Journal of Applied Physics

Thermal conductivity of two-dimensional disordered fibrous materials defined by interfiber thermal contact conductance and intrinsic conductivity of fibers

Cite as: J. Appl. Phys. **127**, 065102 (2020); https://doi.org/10.1063/1.5136238
Submitted: 11 November 2019 . Accepted: 11 January 2020 . Published Online: 10 February 2020

Alexey N. Volkov, and Leonid V. Zhigilei

AIP Publishing

Journal of Applied Physics ARTICLE scitation.org/journal/jap

Thermal conductivity of two-dimensional disordered fibrous materials defined by interfiber thermal contact conductance and intrinsic conductivity of fibers

Cite as: J. Appl. Phys. **127**, 065102 (2020); doi: 10.1063/1.5136238
Submitted: 11 November 2019 · Accepted: 11 January 2020 ·
Published Online: 10 February 2020

Alexey N. Volkov[1,a)] and Leonid V. Zhigilei[2]

AFFILIATIONS

[1]Department of Mechanical Engineering, University of Alabama, 7th Avenue, Tuscaloosa, Alabama 35487, USA
[2]Department of Materials Science and Engineering, University of Virginia, 395 McCormick Road, Charlottesville, Virginia 22904-4745, USA

[a)]**Author to whom correspondence should be addressed:** avolkov1@ua.edu

ABSTRACT

A general framework for the theoretical analysis and numerical calculations of the effective thermal conductivity of two-dimensional homogeneous and isotropic disordered fibrous materials is developed in this work based on the model of random contacts between soft-core spherocylinders. The analysis accounts for the interfiber contact conductance and intrinsic conductivity of fibers and is performed in a wide space of governing parameters that includes the fiber aspect ratio, Biot number calculated for a single thermal contact between fibers, and material density ranging from values corresponding to the percolation threshold up to those characteristic of dense fiber networks. For dense networks, exact theoretical equations for the thermal conductivity of materials composed of spherocylinders with an arbitrary aspect ratio and Biot number are derived. The effect of the intrinsic conductivity of fibers on the thermal transport in fibrous materials is found to depend on the density of contacts and can be significant in sufficiently dense fiber networks even if the Biot number for a single thermal contact is small. Semiempirical corrections to the theoretical equations are derived for small and moderate fiber densities. The power law exponent describing the approximate dependence of the conductivity on the density parameter is found to vary from values close to 1 up to values exceeding 2 when evaluated within different finite ranges of the density parameter. This finding explains the variability of scaling laws for thermal conductivity of fibrous materials suggested in the literature based on numerical simulations performed in different regions of the space of material parameters.

I. INTRODUCTION

A variety of materials can be thought of as disordered networks of fibers, wires, or rod-like particles. Examples of such materials include carbon fibers and nanotubes, metallic nanowires, inorganic powders composed of needle-like particles, fabric, paper, and other organic fiber network materials. Fibrous materials are widely used in thermal management applications, both for thermal insulation and thermal transport, since their thermal transport properties can be tailored by engineering the material structure and tuned in a broad range without changing the physical properties of individual fibers. The bulk conductivity of many common fibrous materials is controlled by the intrinsic conductivity of fibers, while the resistance of interfiber thermal contacts is small and can be neglected. The thermal transport properties of such fibrous materials have been extensively studied during the past few decades based on the random resistor network models[1,2] applied for both electrical and thermal transports. Near the percolation threshold, the conductivity of such materials obeys a power law with a universal exponent that depends only on the dimensionality of the system,[2] while far above the percolation threshold, the conductivity exhibits a linear dependence on the fiber density.[3]

During the last two decades, interest in thermal properties of disordered fibrous materials was reignited by the emergence and proliferation of nanofibrous materials composed of carbon nanotubes (CNTs). The CNT materials, such as films,[4–7] mats,[8–10] aerogels,[11,12] forests,[13] fabric,[14] and "buckypaper,"[15] form a new class of disordered materials with intriguing thermal properties that do not obey theoretical predictions derived for conventional fibrous materials. Although individual CNTs are perfect thermal conductors with measured[16–19] and calculated[20–29] thermal conductivity ranging from a few hundred $W\,m^{-1}\,K^{-1}$ to $\sim$3500 $W\,m^{-1}\,K^{-1}$ and even 6600 $W\,m^{-1}\,K^{-1}$, the measured bulk thermal conductivity of CNT materials is a few orders of magnitude smaller and varies from $\sim$0.1 $W\,m^{-1}\,K^{-1}$ to $\sim$200 $W\,m^{-1}\,K^{-1}$.[30–37] The analysis of the experimental data and theoretical considerations indicate that the thermal conductivity of CNT materials is limited by extremely small contact conductance, leading to a weak thermal coupling between adjacent nanotubes.[38–43] This observation allows one to consider CNT materials as "nonclassical" materials, where bulk conductivity is defined by the resistance of the intertube contacts.[44] Based on this conclusion, a model of thermal transport in such nonclassical materials was suggested,[44] where the intrinsic conductivity of fibers is assumed to be infinitely large and, correspondingly, every fiber is considered as an isothermal object. Such a model was used in multiple theoretical studies and numerical simulations of the thermal conductivity of dilute fiber systems and fiber reinforced composites with fiber densities close to the percolation threshold,[45–50] as well as dense fibrous materials.[3,42,51–57] The theoretical consideration of the thermal transport based on the model of isothermal fibers reveals the quadratic scaling of conductivity with the fiber length and material density,[3,54,56] while other scaling exponents, both smaller and larger than 2, were also deduced from numerical simulations and experiments.[51,52] The unusual quadratic scaling law is explained by the fact that both the density of thermal contacts and average energy flux through a single contact scale linearly with the fiber length and material density. The mesoscopic simulations in Ref. 56 also showed that the quadratic scaling with nanotube length approximately holds even in continuous networks of flexible nanotubes, where CNTs are self-assembled into entangled and interconnected bundles by van der Waals attraction. A nearly quadratic scaling of the conductivity of the CNT films with the material density was then confirmed experimentally.[58]

The numerical calculations of the conductivity of two-dimensional[57] (2D) and three-dimensional[55] (3D) systems of slender rods with finite intrinsic conductivity revealed a gradual transition from the case when the thermal transport is controlled by the thermal contact conductance to the behavior characteristic of ordinary fibrous materials, where the conductance is defined by the intrinsic conductivity of the fibers. The mesoscopic simulations of CNT films with a realistic structure of continuous nanotube networks[59] have shown that this transition occurs in the practically important range of CNT length from a few hundred nm to a few μm, thus suggesting that the model of isothermal fibers is not suitable for quantitative description of the bulk thermal conductivity of CNT materials composed of CNTs longer than several hundred nm. These results were explained using a theoretical method for calculation of thermal conductivity in networks of nonisothermal fibers developed in Ref. 59 based on the assumption of linear temperature distribution along a fiber. This analysis clearly shows that the effect of the intrinsic conductivity depends not on the contact conductance of a single contact but on the total conductance of all contacts of a fiber, which increases with increasing material density. The theoretical consideration in Ref. 59 yielded a simple equation that predicts a gradual variation of thermal conductivity between the limits corresponding to the contact-dominated and intrinsic fiber conductivity-dominated regimes. It has been shown that, with a proper definition of density of thermal contacts, this equation provides an adequate description of the conductivity not only for systems of straight dispersed fibers but also for realistic continuous networks of bundles of carbon nanotubes. A similar equation was also suggested in Refs. 55 and 57 as a fit to the results of numerical simulations. Recently, the approach developed in Ref. 59 was generalized for anisotropic fiber systems.[60] Despite the recent progress in the development of the theoretical understanding of the thermal conductance of fibrous network materials, however, the reported studies have been largely limited to either the consideration of special limiting cases amenable to approximate analytical treatment or numerical simulations performed for limited ranges of material parameters.

The goal of the present paper is to develop a comprehensive theoretical model for predicting the thermal conductivity of fibrous materials at virtually any material density, aspect ratio of fibers, and ratio of intrinsic and contact conductances. For this purpose, we adopt a soft-core model of fibers in the form of spherocylinders (SCs)[47,61–64] and assume a one-dimensional distribution of temperature along an individual fiber. Our approach, in the case of sufficiently dense systems, is based on the *exact* solutions of thermal transport problem and, in contrast to Ref. 59, does not require any *ad hoc* assumptions about the temperature distribution along fibers. We demonstrate that the scaling laws suggested in Refs. 55, 57, 59, and 60 to describe the effect of the intrinsic conductivity of fibers are, in fact, approximations of the analytically derived dependences obtained in the present paper. Furthermore, we show that the scaling laws obtained for dense fibrous systems quickly deviate from the theoretical solutions obtained in Refs. 53–57, 59, and 60 with decreasing material density and cannot be used not only under conditions when the material density is close to the percolation threshold but also for semidilute fiber networks. The deviations from the theoretical solution obtained in the high-density limit can only be revealed through numerical simulations of fiber systems performed in the broad density range, from the percolation threshold to conditions corresponding to dense materials. Using semianalytical treatment guided by numerical simulations, we obtain conductivity equations that are valid even fairly close to the percolation threshold. These equations predict a rather complex dependence of the conductivity on the physical and geometrical parameters of fibers and their density, in accurate agreement with the results of direct numerical simulations. We show, in particular, that the conductivity exponent, if obtained for a limited density range, can vary from 1 up to values larger than 2. This observation can explain the variability of scaling exponents reported in the literature based on experiments and simulations.

In the present paper, we limit our consideration to 2D fibers systems, so that the obtained results can be applied to disordered 2D fibrous materials, such as quasi-2D layered CNT systems,[65] thin

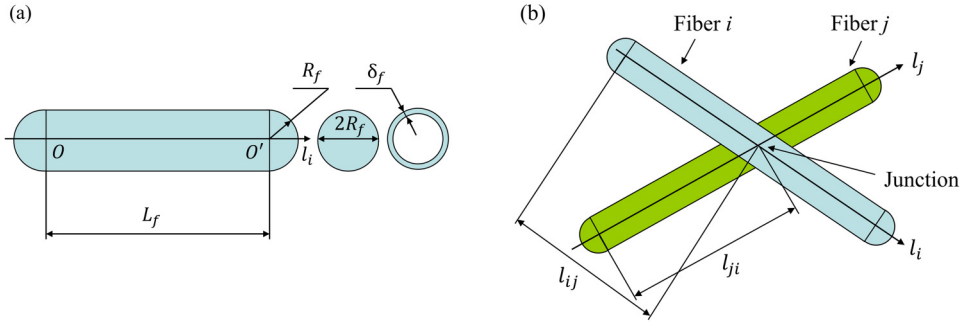

FIG. 1. Schematic representation of a fiber in the form of a rod or a tube modeled by a SC with corresponding cross sections (a) and a junction between two nonparallel 2D SCs (b).

CNT films,[5,6,7,53] flexible electronic devices,[66–68] and 2D nanocomposite materials,[50] where the fibers or nanotubes are preferentially oriented parallel to the plane of the film, are randomly distributed and oriented within the film, and exhibit distinct 2D percolation behavior.[45] The case of 3D fibrous materials with a random orientation of fibers will be considered in another paper.[69]

II. SOFT-CORE RANDOM CONTACT MODEL FOR THERMAL CONDUCTIVITY OF DISORDERED FIBROUS MATERIALS

We consider a material composed of straight fibers, where every fiber has a shape of a spherocylinder (SC), i.e., a circular cylinder of length L_f and external radius R_f capped on both of its ends by two hemispheres, as depicted in Fig. 1(a). A SC can represent either a rod with the cross-sectional area $A_f = \pi R_f^2$ or a tube with the cross-sectional area $A_f = \pi\delta_f(2R_f - \delta_f)$, where δ_f is the thickness of the tube wall. Though other geometrical models of fibers can also be used, e.g., a model of a simple cylinder, the SC model allows us to describe a gradual transition from slender rods to spherical particles by variation of L_f and R_f and to compare our computational results, e.g., on the percolation threshold, with the results of earlier studies.[47,61–64] In this paper, since we limit our consideration to 2D fibrous materials, the axes of all SCs are placed in the same plane. The centers of SCs and their orientations are chosen randomly within this plane. The density of the 2D material is characterized by the surface number density n_S defined as the number of SC centers per unit area. In this case, every SC is a rectangle with dimensions of $(2R_f) \times L_f$ capped by two semicircles of radius R_f. Despite its 2D nature, this plane object is referred to in this paper as a "spherocylinder."

The model of thermal transport in the fibrous material is based on the model of soft-core (interpenetrating) SCs.[64] In the soft-core model, individual SCs can intersect each other as it is schematically shown in Fig. 1(b). Every intersection is considered a thermal contact between SCs and further referred to as a "junction."[70] A junction between SCs i and j occurs if these SCs partially overlap each other and the distance r between nearest points J_{ij} and J_{ji} on the SC axes within their rectangular parts is smaller than $2R_f$ (Fig. 2). The existence of a junction between SCs i and j is characterized by the variable δ_{ij}, which is assumed to be equal to 1 if the contact between SCs i and j exists, otherwise $\delta_{ij} = 0$. The distribution of temperature in a fiber is assumed to be steady-state and one-dimensional, i.e., $T_i = T_i(l_i)$, where l_i is a coordinate counted along the fiber axis [Fig. 1(a)]. Two modes of thermal transport are taken into account, namely, the intrinsic conduction of individual SCs and the contact conduction between them. The intrinsic thermal conduction is assumed to be described by the Fourier law

$$Q_i = -k_f \frac{dT_i}{dl_i} A_f, \tag{1}$$

where $Q_i = Q_i(l_i)$ is the heat flux through the cross section of fiber i at a position defined by coordinate l_i and k_f is the constant value of fiber thermal conductivity. Note that thermal conductivity of a fiber represented by a SC does, in general, depend on its temperature and length. The length dependence, in particular, is usually explained by a contribution of the ballistic thermal transport in fibers shorter than (or comparable to) the phonon mean free path,

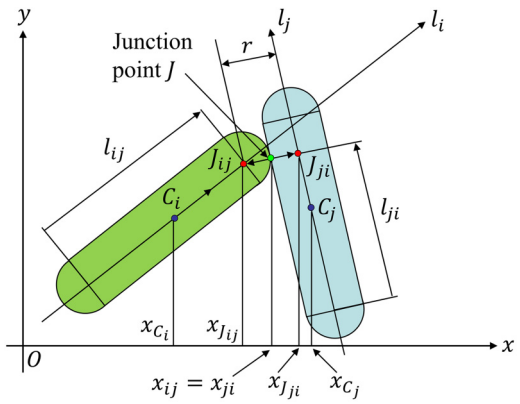

FIG. 2. Junction between two soft-core SCs. The closest distance r is realized between points J_{ij} and J_{ji} on the SC axes within their cylindrical (rectangular in 2D) parts and varies in the range $0 \le r \le 2R_f$. The junction point J is defined as the middle point between points J_{ij} and J_{ji}. The points C_i and C_j are geometrical centers of SCs. For brevity, only a special case of $r = 2R_f$ is shown in the sketch. The definitions of all geometrical parameters of a junction, however, do not depend on this restriction, since the soft-core SCs can freely interpenetrate each other. The general case of arbitrary $r < 2R_f$ can be obtained by replacing the colored objects with SCs of larger radius R_f without changing any other part of the sketch.

as discussed, e.g., for CNTs in Refs. 20 and 25–29. Nevertheless, for a system composed of fibers with the same length and with no large temperature variations, the assumption of a constant intrinsic thermal conductivity is justified.

The contact heat transfer between SCs i and j may, in general, depend on the orientation of the SCs with respect to each other,[71,72] with a particularly strong dependence expected at small misorientation angles between the SCs. In the case considered in this paper, when individual SCs are homogeneously distributed and randomly oriented, the number of pairs of adjacent SCs that are close to being parallel to each other is expected to be small, and the presence of such pairs can be neglected. Thus, in the analysis reported in this paper, the contact heat flux Q_{ij} is assumed to be independent of the relative orientation of SCs and is equal to

$$Q_{ij} = \sigma_c(T_j(l_{ji}) - T_i(l_{ij})), \tag{2}$$

where l_{ij} is the coordinate of a junction between fibers i and j on the axis of fiber i [Fig. 1(b)] and σ_c is the constant contact conductance. The coordinate $x_{ij} = x_{ji}$ of the contact point between fibers i and j on the axis Ox is the coordinate of the point of intersection of the axes of fibers i and j or, when the axes do not cross each other, the center point on the interval connecting the points J_{ij} and J_{ji}, as illustrated in Fig. 2. The bulk thermal conductivity of the fibrous material, k, is calculated by creating a temperature gradient in the material along the axis Ox and applying the Fourier law adopted for the 2D case,

$$\langle Q_x \rangle = -k \nabla T_x L_y, \tag{3}$$

where $\langle Q_x \rangle$ is the ensemble-average value of the heat flux through the cross section of length L_y, which is perpendicular to the axis Ox, k is the thermal conductivity of 2D systems expressed in units of W K^{-1}, and $\nabla T_x = dT/dx$ is the spatial derivative of the average material temperature $T(x)$.

In the present paper, we systematically use dimensionless (reduced) variables that are denoted by a bar over the variable name to distinguish them from corresponding dimensional variables. All length, temperature, and conductivity variables in reduced units are introduced by scaling them by L_f, $\nabla T_x L_f$, and σ_c, respectively, e.g., $\bar{x} = x/L_f$, $\bar{T}_i = T_i/(\nabla T_x L_f)$, and $\bar{k} = k/\sigma_c$. Then, according to Buckingham's Π-theorem,[73] any dimensionless parameter in the considered problem depends on three independent dimensionless governing parameters. These parameters can be introduced in the form of the density parameter $\bar{n}_S = n_S L_f^2$, i.e., average number of SCs in a square $L_f \times L_f$, aspect ratio $\bar{R}_f = R_f/L_f$, and the ratio of the intrinsic, $\sigma_f = k_f A_f/L_f$, and contact, σ_c, conductances,

$$\mathrm{Bi}_c = \frac{\sigma_c}{\sigma_f} = \frac{\sigma_c L_f}{k_f A_f}, \tag{4}$$

which is referred to as the "Biot number for a single contact."[59] The reduced bulk conductivity can then be represented as $\bar{k} = \bar{k}(\bar{n}_S, \bar{R}_f, \mathrm{Bi}_c)$. The case of small Bi_c is characteristic for CNTs due to their extremely large thermal conductivity.[16,17,20,22–26]

III. THE MONTE CARLO METHOD FOR NUMERICAL CALCULATION OF CONDUCTIVITY

The Monte Carlo calculations of thermal conductivity were performed for square samples of dimension L_S ($L_x = L_y = L_S$) in Cartesian coordinates Oxy, where the center O coincides with the sample center, while the axes Ox and Oy are parallel to the sample boundaries. The sample size L_S is chosen to be larger than $2L_{ff}$, where $L_{ff} = L_f + 2R_f$ is the total SC length. In order to calculate k numerically, based on Eq. (3), we generate a series of samples with random distributions of fibers at fixed n_S, L_f, R_f, and L_S as described in Sec. III A. For every random sample, we solve the thermal transport problem as described in Secs. III B and III C and calculate the heat flux Q_x through the sample and temperature distribution in every fiber. These quantities are then averaged over an ensemble of generated samples in order to obtain Q_x and ∇T_x in Eq. (3). Whenever necessary, we determine many other ensemble-average parameters along with Q_x and $T(x)$, which are denoted by $\langle \dots \rangle$, e.g., the percolation probability $P_P = \langle S_P \rangle$, where S_P is equal to either 1 or 0 depending on whether the percolating cluster exists in a particular sample or not (see Sec. III A). All these parameters are calculated numerically as arithmetic means of corresponding parameters for individual random samples. Each sample is divided into a one-dimensional mesh of cells with the size $\Delta x = 0.02 L_{ff}$ in the direction of the axis Ox in order to obtain the distribution of the average material temperature $T(x)$. The value of $T(x)$ in a given cell is then calculated as a weighted average temperature of SCs present in this cell, with contributions from different SCs weighted by parts of their length that belong to the cell.

A. Generation of samples with a random structure

At the first stage of sample preparation for desired values of n_S, L_f, R_f, and L_S, the number of SCs in the sample is calculated as $N = n_S L_S^2$, and N SCs are randomly generated and distributed within the area of the sample. The criterion of the junction existence is then applied to all pairs of SCs, and the variable δ_{ij} is determined for all i and j. As a precaution, the junctions between almost parallel SCs with $\sin^2 \vartheta_{ij} < 10^{-10}$, where ϑ_{ij} is the angle between axes of fibers i and j, are neglected, although most of the randomly generated samples do not contain such pairs of fibers at all. Next, the SCs intersecting the right and left sample boundaries at $|x| = L_S/2$ are identified. It is assumed that all SCs intersecting these boundaries are linked to the heat baths and have fixed temperatures of T_{B1} and T_{B2}. In order to characterize the position of every SC in the sample with respect to the heat baths, a variable χ_i is introduced, which is equal to 1 if SC i crosses the line $x = -L_S/2$, 2 if SC i crosses the line $x = L_S/2$, and 0 for other SCs. The condition $L_x > L_{ff}$ guarantees the absence of SCs that are connected simultaneously to both heat baths. Other boundaries of the sample are assumed to be periodic, and the minimum image convention[74] is used to determine relative positions of SCs in the y-direction. Hence, a gradient of average temperature in the samples exists only in the x-direction. The condition $L_y > 2L_{ff}$ ensures the absence of "self-interaction" among SCs and the applicability of the minimal image conversion approach. For sufficiently large samples (see Sec. IV), the calculated thermal conductivity does not depend on the imposed temperatures of the heat baths,

T_{B1} and T_{B2}, since the thermal properties of individual fibers are assumed to be independent of the temperature.

If $\bar{n}_S$ is small, SCs can form isolated clusters, i.e., groups of SCs that have junctions only with SCs of the same group. The disintegration of a continuous network into clusters plays a very important role in the conductivity of disordered materials near the percolation threshold,[2] i.e., the minimum density when an infinitely large sample contains a percolating cluster that connects opposing boundaries of the sample. We perform a cluster identification procedure[74] that allows us to decompose the sample into individual clusters and identify the SCs belonging to non-percolating clusters. All non-percolating clusters are excluded from further thermal transport calculations. For each sample, we introduce its percolation state S_P that is equal to 1 if the sample contains at least one percolating cluster and 0 otherwise.

B. Thermal model for fibers with infinitely large intrinsic conductivity

If the intrinsic conductivity of fibers is infinitely large and, correspondingly, $\mathrm{Bi}_c = 0$, then the temperature T_i of SC i is constant and does not vary along the SC length. In a steady state, the temperature of SC i with $\chi_i = 0$ can be found from the balance of all incoming contact heat fluxes, $\sum_{j=1}^{N} \delta_{ij} Q_{ij} = 0$, where Q_{ij} is defined by Eq. (2), while the temperatures of all SCs with $\chi_i = 1, 2$ are kept equal to the heat bath temperatures. That is, the temperatures of SCs belonging to percolating clusters can be found by solving the following system of equations:

$$\sum_{j=1}^{N} \delta_{ij}(T_j - T_i) = 0, \quad \text{if } \chi_i = 0, \tag{5a}$$

$$T_i = T_{B\chi_i}, \quad \text{if } \chi_i = 1, 2. \tag{5b}$$

It is convenient to introduce additional functions $\chi_i(x)$, $\delta_{ij(+)}(x)$, and $\delta_{ij(-)}(x)$ in order to formulate compact equations for the heat flux $Q_x(x)$ through an arbitrary sample cross section with coordinate x. The function $\chi_i(x)$ is equal to 1 if SC i intersects the cross section $x = \text{const}$, otherwise $\chi_i(x) = 0$. The function $\delta_{ij(+)}(x)$ indicates the position of the junction between SCs i and j with respect to the plane $x = \text{const}$, such that $\delta_{ij(+)}(x) = 1$ if $\delta_{ij} = 1$ and $x_{ij} \geq x$, otherwise $\delta_{ij(+)}(x) = 0$. Similarly, $\delta_{ij(-)}(x) = 1$ if $\delta_{ij} = 1$ and $x_{ij} < x$, otherwise $\delta_{ij(-)}(x) = 0$. The fluxes of heat $Q_{(+)}(x)$ and $Q_{(-)}(x)$ transferred in positive and negative directions of the axis Ox through a sample cross section can then be found by summing the contact heat fluxes for all SCs crossing this cross section and all junctions located to the right and left from it, respectively, i.e.,

$$Q_{(+)}(x) = -\sum_{i=1}^{N} \chi_i(x) \sum_{j=1}^{N} \delta_{ij(+)}(x) Q_{ij}, \tag{6}$$

$$Q_{(-)}(x) = \sum_{i=1}^{N} \chi_i(x) \sum_{j=1}^{N} \delta_{ij(-)}(x) Q_{ij}. \tag{7}$$

In the steady state, owing to Eq. (5a), $Q_{(+)}(x)$ is independent of x if $x \leq L_S/2 - L_{ff}$, and $Q_{(-)}(x)$ is independent of x if $x \geq -L_S/2 + L_{ff}$. For such x, both $Q_{(+)}(x)$ and $Q_{(-)}(x)$ must be equal to the invariant heat flux Q_x through the sample in the direction of the axis Ox: $Q_x = Q_{(+)}(x) = Q_{(-)}(x)$. In particular, Q_x is equal to both $Q_{B1} = Q_{(+)}(-L_S/2)$ and $Q_{B2} = Q_{(-)}(L_S/2)$ defined at the left and right boundaries. The independence of $Q_{(+)}(x)$ and $Q_{(-)}(x)$ on x, if x is in the ranges mentioned above, can be used for verification of the numerical solutions of the linear system given by Eq. (5). In the present paper, this system is solved iteratively by the Gauss–Seidel method[75] until $|Q_{B1} - Q_{B2}| < (1/2)(Q_{B1} + Q_{B2})\Delta_Q$, where the tolerance Δ_Q is taken to be equal to 10^{-9}. At $\bar{n}_S \leq 300$, the number M of the generated samples used for calculation of ensemble-average parameters at constant $\bar{n}_S$ and $\bar{R}_f$ was equal to 10^4, while $M = 10^3$ was adopted at $\bar{n}_S > 300$.

C. Thermal model for fibers with finite intrinsic conductivity

In this section, we consider a case of finite, i.e., noninfinite and nonzero, Biot number, when the intrinsic thermal conductivity of fibers and interfiber contact conductance are finite. Note that the conductivity of semicircular "caps" of SCs is still assumed to be infinitely large. Then the steady-state distribution of temperature $T_i(l_i)$ along the axis of SC i that belongs to a percolating cluster and is not attached to the heat baths can be found from the heat conduction equation,[59]

$$\frac{d}{dl_i}\left(A_f k_f \frac{dT_i}{dl_i}\right) = -\sum_{j=1,\delta_{ij}=1}^{N} \delta(l_i - l_{ij}) Q_{ij}, \quad \text{if } \chi_i = 0, \tag{8}$$

where $\delta(l)$ is the Dirac δ-function and $Q_{ij} = \sigma_c(T_{ji} - T_{ij})$, with $T_{ij} = T_i(l_{ij})$ and $T_{ji} = T_j(l_{ji})$ being the temperatures of SCs i and j at the corresponding junction. Equation (8) should be solved with the boundary conditions at the SC ends,

$$A_f k_f \left.\frac{dT_i}{dl_i}\right|_{l_i=0} = -\sum_{j=1,\delta_{ij}=1,l_{ij}=0}^{N} Q_{ij}, \tag{9a}$$

$$A_f k_f \left.\frac{dT_i}{dl_i}\right|_{l_i=L_f} = \sum_{j=1,\delta_{ij}=1,l_{ij}=L_f}^{N} Q_{ij}, \tag{9b}$$

while temperatures of SCs with $\chi_i = 1, 2$ are assumed to be constant, as required by Eq. (5b).

The gradient of temperature dT_i/dl_i is constant between neighbor junctions according to Eq. (8) and, hence, the SC temperature is a piecewise-linear function of l_i. The temperature distribution along a SC is then completely determined by values of temperature at the junctions. The formulation of equations with respect to the discrete values of temperature at the junctions requires the introduction of additional notation, since these values in every SC must be numbered in the order of increasing l_{ij}. If one assumes that SC i has N_i junctions with other SCs in points l'_{im} $(0 < l'_{im} < L_f)$ where the temperatures are equal to T'_{im} $(m = 1, \ldots, N_i)$ and l'_{im} increases with m, then the distribution of temperature in SC i is completely defined by the array $(T'_{i1}, \ldots, T'_{iN_i})$. The prime in l'_{im} and T'_{im} is used to highlight the

fact that the second subscript in these quantities is the index of a junction and, thus, T'_{im} is different from T_{ij} that appears in Eq. (8), where a subscript is the index of a second SC forming the junction. Note that mapping of T_{ij} to T'_{im} or vice versa can be easily performed in computational codes, but it is not necessary for the analysis reported in other parts of this paper. Therefore, the notation with prime marks, introduced above, is only used in this section.

The values in array $(T'_{i1}, \ldots, T'_{iN_i})$ must satisfy equations that can be obtained by integrating Eq. (8) over the intervals $[(l'_{im-1} + l'_{im})/2, (l'_{im} + l'_{im+1})/2]$:

$$\frac{\bar{T}'_{im+1} - \bar{T}'_{im}}{\bar{l}'_{im+1} - \bar{l}'_{im}} - \frac{\bar{T}'_{im} - \bar{T}'_{im-1}}{\bar{l}'_{im} - \bar{l}'_{im-1}} = \mathrm{Bi}_c(\bar{T}'_{im} - \bar{T}'_{i'(i,m)m'(i,m)}), \tag{10}$$

where functions $i'(i, m)$ and $m'(i, m)$ define the index of a SC and index of a junction in that SC, which is paired to form junction m with SC i. In Eq. (10), the bar over variable names is used to denote dimensionless values of length $\bar{l}'_{im}$ and temperature $\bar{T}'_{im}$ according to the convention introduced at the end of Sec. II.

The system of Eq. (10) with boundary conditions given by Eq. (9) for internal SCs and Eq. (5b) for fibers directly connected to the heat baths is solved iteratively by the Gauss–Seidel method. The heat flux Q_x is then calculated based on Eqs. (6) or (7), where Q_{ij} is defined by Eq. (2).[76] The matrix of coefficients of this linear system is ill-conditioned if distances between neighbor junctions $\Delta l'_{im} = l'_{im+1} - l'_{im}$ are very small, and it becomes singular if any $\Delta l'_{im} = 0$. In order to regularize the system, we combine the neighbor junctions into a group if the distance between them $\Delta l'_{im}$ is smaller than a small positive constant $\Delta l_{\min}$, which serves as a regularization parameter, and assume that all junctions in a group have the same temperature. In preliminary simulations at $\bar{R}_f = 0$ and $\mathrm{Bi}_c = 10$, we found that the error in $\bar{k}$ due to finite value of the regularization parameter is less than 0.6% at $\Delta l_{\min}/L_f \le 0.01$ and becomes as large as 8% at $\Delta l_{\min}/L_f = 0.1$. Further simulations show that the numerical error in $\bar{k}$ strongly increases when Bi_c and $\bar{n}_S$ exceed the levels of $\mathrm{Bi}_c \approx 10$ and $\bar{n}_S \approx 100$. Based on these results, a value of $\Delta l_{\min}/L_f = 0.01$ is adopted in all simulations where $\mathrm{Bi}_c < 10$ and $\bar{n}_S < 100$. In simulations performed for $\mathrm{Bi}_c \ge 10$ and $\bar{n}_S \ge 100$, a reduced value of $\Delta l_{\min}/L_f = 0.003$ is used. It is worth noting that the correct scaling behavior of $\bar{k}$ at $\bar{n}_S \to \infty$ (Sec. VII) can be established numerically only if $\Delta l_{\min}/L_f$ is sufficiently small to avoid excessive errors due to regularization. All other numerical parameters in simulations performed with finite intrinsic conductivity are identical to those used in simulations with $\mathrm{Bi}_c = 0$.

IV. PERCOLATION THRESHOLD AND FINITE-SIZE EFFECTS

The continuum percolation problem in systems of rod-like particles was a subject of numerous studies, e.g., Refs. 47, 61–64, and 80. In the present work, we calculate the percolation threshold in order to verify our numerical model, reveal the effect related to the finite size of our samples, and describe the conductivity near the percolation threshold in terms of the reduced density parameter.

In 2D networks of SCs with fixed $\bar{R}_f$, the percolation threshold can be formulated in terms of the critical density parameter $\bar{n}_{SP}$ that is the minimum value of $\bar{n}_S$ at which a percolating cluster still exists in an infinitely large sample, i.e., percolation probability $P_p(\bar{n}_S) = 1$ at $\bar{n}_S > \bar{n}_{SP}$ and $P_p(\bar{n}_S) = 0$ at $\bar{n}_S < \bar{n}_{SP}$. The existence of a unique critical density parameter $\bar{n}_{SP}$ is justified theoretically based on the cluster expansion method[77] and also supported by numerous numerical simulations, e.g., in Refs. 61 and 62, where the same critical value corresponding to the onset of percolation, $\sqrt{\pi \bar{n}_{SP}}/2$, is found by variation of L_f at constant n_S and n_S at constant L_f.

In finite-size samples, the percolation probability $P_p(\bar{n}_S)$ is a continuous function of $\bar{n}_S$ (Fig. 3) and does not exhibit a distinct threshold behavior.[2] Then the percolation threshold can be approximately determined as an expectation value $\bar{n}_{SP(\hat{L}_S)}$ of $\bar{n}_S$, which are distributed with the cumulative distribution function $P_p(\bar{n}_S)$, obtained for samples of a sufficiently large relative size $\hat{L}_S = L_S/L_{ff}$ (Fig. 3). The cumulative distribution function $P_p(\bar{n}_S)$ corresponds to the probability density function (PDF) $f_p(\bar{n}_S) = dP_p(\bar{n}_S)/d\bar{n}_S$, so that $\bar{n}_{SP(\hat{L}_S)}$ can be numerically calculated as

$$\bar{n}_{SP(\hat{L}_S)} = \int_0^\infty \bar{n}_S f_p(\bar{n}_S) d\bar{n}_S = \int_0^\infty \bar{n}_S \frac{dP_p}{d\bar{n}_S}(\bar{n}_S) d\bar{n}_S \simeq \sum (\bar{n}_{S(k)} + \bar{n}_{S(k+1)}) \frac{P_{p(k+1)} - P_{p(k)}}{2}, \tag{11}$$

where $P_{p(k)} = P_p(\bar{n}_{S(k)})$. We found that actual $f_p(\bar{n}_S)$ can be approximated by the Gaussian distribution and, thus, the approximate value of $\bar{n}_{S(\hat{L}_S)}$ can be also found from the condition $P_p(\bar{n}_{SP(\hat{L}_S)}) = 1/2$. For example, at $\bar{R}_f = 0$, this condition gives $\bar{n}_{S(16)} = 5.494$, while Eq. (11) results in $\bar{n}_{S(16)} = 5.502$. Convergence of $\bar{n}_{SP(\hat{L}_S)}$ to $\bar{n}_{SP}$ at $\hat{L}_S \to \infty$ is slow, so that it is not possible to obtain three decimal digits in $\bar{n}_{SP}$ even at $\hat{L}_S = 64$. Our calculations prove that a more accurate estimation of $\bar{n}_{SP}$ at a fixed $\hat{L}_S$ can be obtained with the intersection method.[78,79] Indeed, one can see

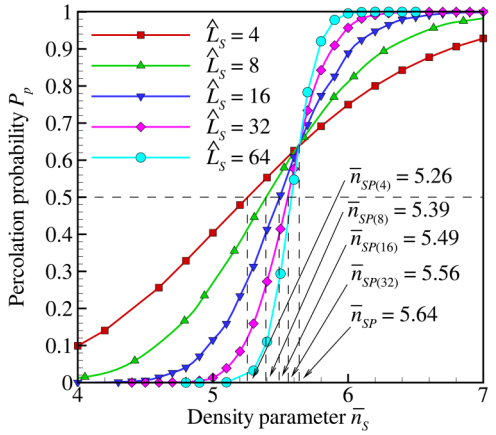

FIG. 3. Percolation probability P_p vs density parameter $\bar{n}_S$ found at $\bar{R}_f = 0$ and various sample sizes $\hat{L}_S = L_S/L_f$. The values of $\bar{n}_{S(\hat{L}_S)}$ correspond to $P_p = 0.5$ at a given $\hat{L}_S$.

that the curves computed for different $\hat{L}_S$ intersect each other at $\bar{n}_S = 5.64$ with the error within 0.03% at $\hat{L}_S \geq 4$. That "intersection" point at a finite $\hat{L}_S$ lies closer to the true percolation threshold than $\bar{n}_{SP(\hat{L}_S)}$ for values of $\hat{L}_S$ normally accessible in numerical simulations, suggesting that the intersection method provides a computationally efficient and accurate approach for the determination of the percolation threshold. In particular, the intersection method is capable of predicting $\bar{n}_{SP}$ with the error less than 0.1% in the simulations conducted for small samples with $\hat{L}_S \leq 8$, while, e.g., at $\bar{R}_f = 0$, the difference between $\bar{n}_{SP}$ and $\bar{n}_{SP(8)} = 5.39$ is about 4.5%. Our simulations show that, at $\bar{R}_f = 0$, the percolation threshold corresponds to $\bar{n}_{SP} = 5.64$ with the error 0.03%. This result is in a good agreement with previously reported values of 5.71,[61,62] 5.59 ± 0.05,[80] and 5.64 ± 0.02.[81] By applying the intersection method at $\bar{R}_f > 0$, we found that $\bar{n}_{SP} = 5.57$ at $\bar{R}_f = 0.001$, $\bar{n}_{SP} = 5.02$ at $\bar{R}_f = 0.01$, $\bar{n}_{SP} = 4.13$ at $\bar{R}_f = 0.03$, and $\bar{n}_{SP} = 2.50$ at $\bar{R}_f = 0.1$.

The value of conductivity naturally depends on the sample size close the percolation threshold,[2] while at $\bar{n}_S \gg \bar{n}_{SP}$, the effect of $\hat{L}_S$ on k is defined by an approach used for numerical calculation of ∇T_x. If $L_S > 2L_{ff}$ at $\mathrm{Bi}_c = 0$, then the distribution $T(x)$ consists of the central linear part and boundary regions, where the temperature gradient is not constant (Fig. 4). The nonlinear distributions $T(x)$ appear in the boundary regions at $x \leq -L_S/2 + L_{ff}$ or $x \geq L_S/2 - L_{ff}$, where some SCs are directly linked to the heat baths. As a result, the thermal conductivity calculated based on Eq. (3), where ∇T_x is replaced by the imposed gradient $\nabla T_{Bx} = (T_{B2} - T_{B1})/L_S$, strongly depends on the sample size $\hat{L}_S$ even far above the percolation threshold, e.g., at $\bar{n}_S = 73.7$ (the solid curve in the inset of Fig. 4). On the contrary, utilizing the temperature gradient in the linear part of the sample,

$$\nabla T_x = \frac{T(L_S/2 - L_{ff}) - T(-L_S/2 + L_{ff})}{L_S - 2L_{ff}}, \tag{12}$$

one can obtain values of k that are practically independent of $\hat{L}_S$ already at $\hat{L}_S \geq 4$ (dashed curve in the inset of Fig. 4). We found that, with the latter approach, the conductivity can be accurately calculated based on finite-size samples with $\hat{L}_S = 4$ at $\bar{n}_S > 20$ for any $\bar{R}_f$. For smaller $\bar{n}_S$, however, the allowable sample size is limited from below by the need to account for the effect of large clusters. Thus, in simulations performed at $8 \leq \bar{n}_S \leq 20$ we use $\hat{L}_S = 16$. At even smaller $\bar{n}_S$, near the percolation threshold, the dependence of the conductivity on the sample size is inevitable and is discussed in Sec. V.

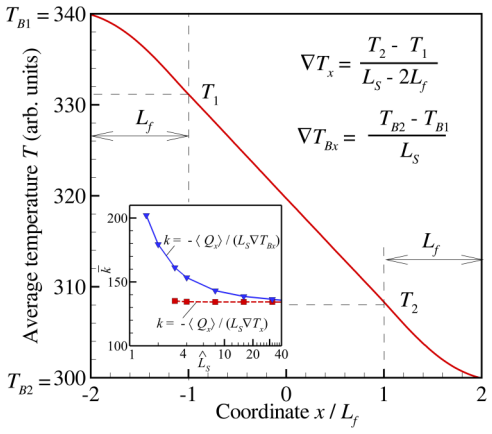

FIG. 4. Distribution of the average material temperature T along the coordinate x, obtained at $\bar{n}_S = 73.7$, $\bar{R}_f = 0$, $\nabla T_{Bx} L_f = 10$, and $\mathrm{Bi}_c = 0$. This distribution is used for calculation of the temperature gradient ∇T_x in the central part of the sample, $-L_S/2 + L_f < x < L_S/2 - L_f$, based on Eq. (12). The inset shows the numerical values of conductivity $\bar{k}$ vs the sample size $\hat{L}_S = L_S/L_f$. The values of $\bar{k}$ calculated based on the imposed gradient ∇T_{Bx} (solid curve) depend on $\hat{L}_S$ even at $\hat{L}_S \sim 40$, while $\bar{k}$ calculated based on ∇T_x (dashed curve) is practically independent of $\hat{L}_S$ at $\hat{L}_S \geq 4$.

V. COMPUTATIONAL RESULTS FOR INFINITELY LARGE INTRINSIC CONDUCTIVITY OF FIBERS

The typical patterns of fiber temperatures in random samples are shown in Fig. 5 for various values of $\bar{n}_S$ at $\bar{R}_f = 0$ and $\mathrm{Bi}_c = 0$. At $\bar{n}_S = 4.42$ [Figs. 5(a) and 5(b)], which is below of the percolation threshold ($P_p = 0.06$ at $\hat{L}_S = 8$), many groups (quasi-clusters) of fibers that are poorly connected to each other are formed, and the effect of fluctuations caused by the random structure of a sample is very pronounced. The shaded area in Fig. 5(a) covers one of such quasi-clusters, which has only one connection with the rest of the sample. A significant part of the sample consists of non-percolating clusters that do not contribute to thermal transport. At $\bar{n}_S = 7.37$ [Figs. 5(c) and 5(d)], which is slightly above the percolation threshold ($P_p = 0.99$ at $\hat{L}_S = 8$), the effect of clustering of fibers into quasi-clusters with almost constant temperatures is still rather pronounced, although the number of fibers involved into non-percolating clusters is small.

Close to the percolation threshold, the conductivity $\bar{k}$ depends on the sample size [Fig. 6(a)]. If the sample is sufficiently large, the value of $\bar{k}$ is affected by the sample size only in a small vicinity of $\bar{n}_{SP}$. At $\bar{R}_f = 0$, the sample-size-independent value of $\bar{k}$ can be found with the error within 2% in simulations with $\hat{L}_S = 16$ for $\bar{n}_S \geq 8$ and in simulations with $\hat{L}_S = 64$ for $\bar{n}_S \geq 6.5$. If conductivity $\bar{k}$ is plotted vs the reduced density parameter $\bar{n}_S - \bar{n}_{SP}$, it exhibits a universal scaling behavior.[2] With increasing $\hat{L}_S$, the conductivity $\bar{k}$ approaches the dashed-dotted line in Fig. 6(b), which corresponds to the power law $C_p(\bar{n}_S - \bar{n}_{SP})^t$, where the conductivity exponent t presumably depends only on the dimensionality of the problem. For the 2D percolation problem, it was numerically found to be equal to 1.3.[2] We plot the dashed-dotted line in Fig. 6(b) as the best fit for the tangent (in double logarithmic scale) to the curves for $\bar{k}$ found at $\hat{L}_S = 64$ in the range $2 < \bar{n}_S - \bar{n}_{SP} < 10$, where the difference between these values of $\bar{k}$ and corresponding values calculated at $\hat{L}_S = 32$ is about 1%. This best fit gives $C_p = 0.18$ and $t = 1.33$. One can see that this fit is in a good agreement with numerical results obtained at $\hat{L}_S = 128$ in the range $0.2 < \bar{n}_S - \bar{n}_{SP} < 0.6$. Further simulation showed that t is independent of $\bar{R}_f$ at $\bar{R}_f \leq 0.03$ with an error of less than 5%. Thus, our simulations do not support the conclusion made in Ref. 47 on the dependence of the conductivity exponent on the nanotube aspect ratio.

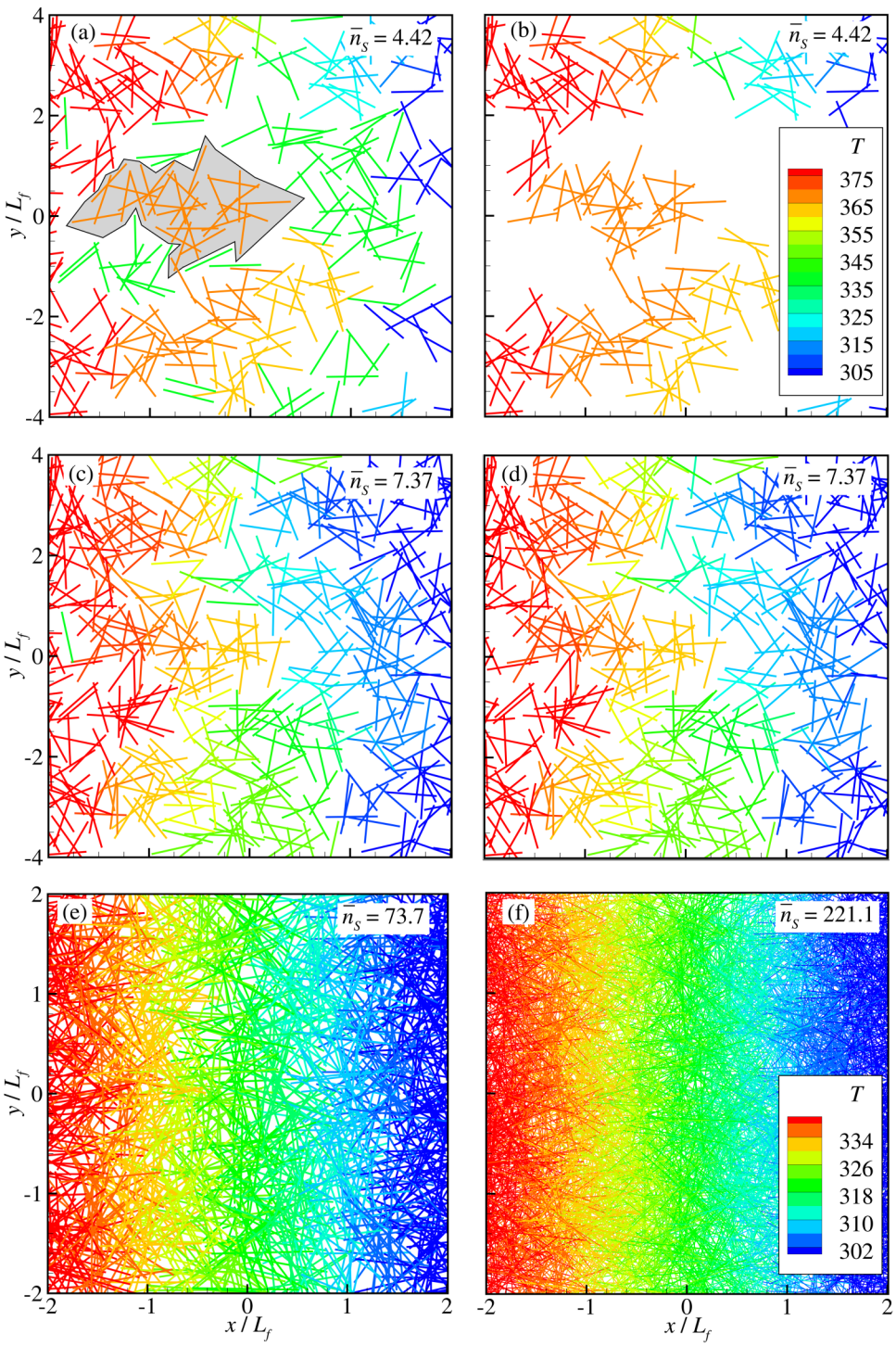

FIG. 5. Patterns of SC temperatures obtained in randomly generated samples at $\bar{R}_f = 0$ and $\mathrm{Bi}_c = 0$ for $\bar{n}_S = 4.42$ [(a) and (b)], $\bar{n}_S = 7.37$ [(c) and (d)], $\bar{n}_S = 73.7$ (e), and $\bar{n}_S = 221.1$ (f). The individual SCs are colored according to their temperatures. In panels (a), (c), (e), and (f), all fibers in the samples are shown, while in panels (b) and (d), only SCs that belong to percolating clusters are depicted. The shaded area in panel (a) surrounds a part of a percolating cluster, where all SCs have the same temperature, and, therefore, do not contribute to the thermal transport. Panels (e) and (f) share the color scale shown in panel (f). Other panels share the color scale shown in panel (b).

At $\bar{n}_S \gg \bar{n}_{SP}$, e.g., $\bar{n}_S = 73.7$ and $\bar{n}_S = 221.1$, the fields of fiber temperatures shown in Figs. 5(e) and 5(f) qualitatively look like monotonous distributions of temperature in a bulk material, although each SC has a constant temperature. In these cases, all fibers in the sample constitute a single percolating cluster, and every SC interacts with multiple neighboring SCs. The temperature of an individual fiber in this case is defined by the position of the fiber center and is almost independent of the realization of the

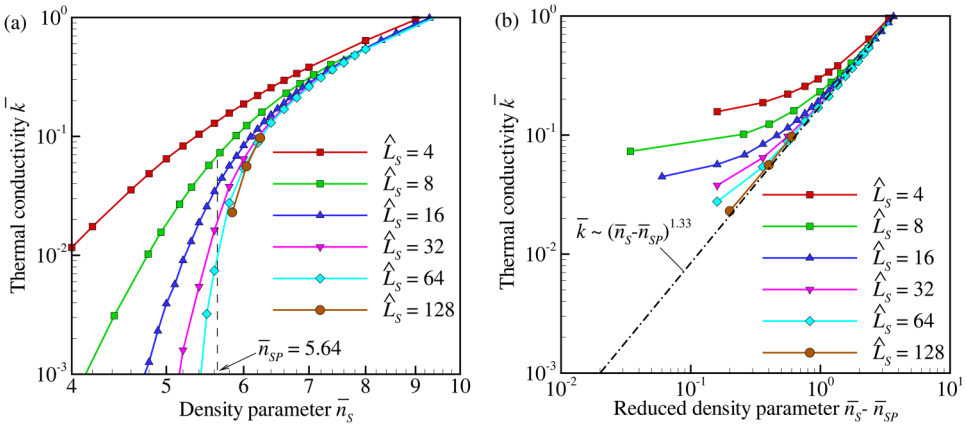

FIG. 6. Thermal conductivity $\bar{k}$ vs density parameter $\bar{n}_S$ (a) and reduced density parameter $\bar{n}_S - \bar{n}_{SP}$ (b) at $\bar{R}_f = 0$ and $\mathrm{Bi}_c = 0$ calculated for various sample sizes $\hat{L}_S = L_S/L_f$. In panel (b), the dashed-dotted curve represents a power fit of calculated values of $\bar{k}$ at $\hat{L}_S = 64$ in the range $2 \le \bar{n}_S - \bar{n}_{SP} \le 10$. The values of $\bar{k}$ obtained at $\hat{L}_S = 128$ are well described by this power fit.

random structure of the sample. This fact enables the development of a theoretical approach that predicts the conductivity of fibrous materials at high values of the density parameter (Secs. VI A and VIII A).

The results of numerical calculations of $\bar{k}$ are shown by symbols and solid curves in Fig. 7 in a broad range of $\bar{n}_S$. These values of $\bar{k}$ are proved to be independent of $\hat{L}_S$ at $\bar{n}_S \ge 8$ with an error within 2%. One can see that, for large $\bar{n}_S$, dependences $\bar{k}(\bar{n}_S)$ at $\bar{R}_f = \text{const}$ approach asymptotes that are shown by the dashed, dashed-dotted, and dashed-double-dotted lines. These asymptotes correspond to the power law $\bar{k} \sim \bar{n}_S^2$. With decreasing $\bar{n}_S$, $\bar{k}(\bar{n}_S)$ deviates from the asymptotes and drops down to zero near the percolation threshold much faster than $\bar{k} \sim \bar{n}_S^2$. This behavior can potentially explain the variability of the values of the conductivity exponent obtained in earlier studies performed in narrow ranges of $\bar{n}_S$. In particular, one can hypothesize that the power law $k \propto L_f^{2.16}$ found numerically in Ref. 52 is likely to reflect the fact that the authors performed simulations in a range of $\bar{n}_S$ intermediate between the percolation threshold and dense material, where the scaling law $\bar{k} \propto \bar{n}_S^2$ corresponding to the asymptotes in Fig. 7 is not reached yet. An approximation for the thermal conductivity of fibrous materials adopted for the case when $\bar{n}_S \gg \bar{n}_{SP}$ and $\bar{k} \sim \bar{n}_S^2$ is further referred to in the present paper as "high-density approximation." The data in Fig. 7 show that the high-density approximation is valid at $\bar{R}_f \le 0.1$ with errors of 20% at $\bar{n}_S > 30$, 6% at $\bar{n}_S > 60$, and 3% at $\bar{n}_S > 10^2$.

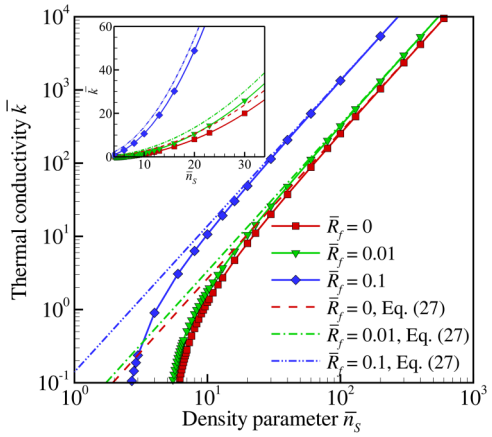

FIG. 7. Thermal conductivity $\bar{k}$ vs density parameter $\bar{n}_S$ calculated at $\mathrm{Bi}_c = 0$ for $\bar{R}_f = 0$ (red squares), $\bar{R}_f = 0.01$ (green gradients), and $\bar{R}_f = 0.1$ (blue diamonds). Symbols and solid curves show the results of numerical calculations; other curves are the predictions of Eq. (27). The inset shows values of $\bar{k}$ in an intermediate range of $\bar{n}_S$. The data are partially taken from Ref. 56.

VI. CONDUCTIVITY EQUATION FOR INFINITELY LARGE INTRINSIC CONDUCTIVITY OF FIBERS

A. Theoretical solution in the high-density approximation

Though in theoretical analysis one can assume that the material sample is infinite, we prefer to start the derivation of an equation for the conductivity by considering a sample that has a finite size L_y in the y-direction. This approach allows us to establish a transparent relationship between the theoretical predictions and numerical results obtained for finite-size samples.

The ensemble averaging of Eq. (6) gives the average heat flux in the form

$$\langle Q_x \rangle = -\left\langle \sigma_c \sum_{i=1}^{N} \chi_i(x) \sum_{j=1}^{N} \delta_{ij(+)}(x)(T_j - T_i) \right\rangle = -\sigma_c \langle N_{J(+)} \rangle \langle \Delta T_{(+)} \rangle, \tag{13}$$

where $\langle N_{J(+)} \rangle$ is the average total number of junctions with $\chi_i(x) = 1$ and $\delta_{ij(+)}(x) = 1$, i.e., junctions that are located on the right of the plane $x = \text{const}$ on fibers that cross this plane, and $\langle \Delta T_{(+)} \rangle$ is the average temperature difference in such junctions,

$$\langle N_{J(+)} \rangle = \left\langle \sum_{i=1}^{N} \chi_i(x) \sum_{j=1}^{N} \delta_{ij(+)}(x) \right\rangle, \tag{14}$$

$$\langle \Delta T_{(+)} \rangle = \frac{1}{\langle N_{J(+)} \rangle} \left\langle \sum_{i=1}^{N} \chi_i(x) \sum_{j=1}^{N} \delta_{ij(+)}(x)(T_j - T_i) \right\rangle. \quad (15)$$

The value of $\langle N_{J(+)} \rangle$ can be represented in the form $\langle N_{J(+)} \rangle = \langle N_x \rangle \langle N_J \rangle / 2$, where $\langle N_x \rangle$ is the average number of SCs crossing any plane $x = \text{const}$ within the sample and $\langle N_J \rangle$ is the average number of junctions for an individual fiber. Equation (13) then reduces to

$$\langle Q_x \rangle = -\sigma_c \langle N_x \rangle \frac{\langle N_J \rangle}{2} \langle \Delta T_{(+)} \rangle. \quad (16)$$

By combining Eq. (16) with the Fourier law given by Eq. (3), we express the conductivity in the following form:

$$k = \sigma_c \frac{L_f}{L_y} \langle N_x \rangle \frac{\langle N_J \rangle}{2} \frac{\langle \Delta T_{(+)} \rangle}{\nabla T_x L_f} = \sigma_c \frac{L_f}{L_y} \langle N_x \rangle \frac{\langle N_J \rangle}{2} \langle \Delta \bar{T}_{(+)} \rangle, \quad (17)$$

where $\langle \Delta \bar{T}_{(+)} \rangle = \langle \Delta T_{(+)} \rangle / (\nabla T_x L_f)$.

The values of $\langle N_x \rangle$ and $\langle N_J \rangle$ can be found as ensemble-average values of corresponding variables assuming homogeneous distribution of SC centers and homogeneous distribution of fiber orientations within the plane Oxy. In particular, $\langle N_x \rangle$ can be represented as $\langle N_x \rangle = \langle N \rangle P_x$, where $\langle N \rangle = n_S L_x L_y$ is the average total number of SCs in the sample and P_x is the probability of intersection of any given SC with an axis $x = \text{const}$ within the sample, e.g., with $x = 0$. By assuming random distributions of the centers of SCs along the axis Ox and the angles θ_1 between the axes of SCs and the axis Ox, P_x can be expressed as

$$P_x = \frac{1}{L_x} \int_0^{2\pi} (L_f |\cos\theta_1| + 2R_f) \frac{d\theta_1}{2\pi} = \frac{2}{\pi} \frac{L_f}{L_x} (1 + \pi \bar{R}_f), \quad (18)$$

and, hence,

$$\frac{L_f}{L_y} \langle N_x \rangle = \frac{2}{\pi} \bar{n}_S (1 + \pi \bar{R}_f). \quad (19)$$

The average number of junctions per fiber, $\langle N_J \rangle$, can be represented in the form

$$\langle N_J \rangle = \frac{\langle N \rangle^2 P_J}{\langle N \rangle} = \langle N \rangle P_J, \quad (20)$$

where P_J is the probability of existence of a junction between any pair of SCs.

The derivation of P_J can be based on the concept of the excluded volume, or, in the case of 2D samples, excluded area, A_{ex}, which was originally introduced by Onsager[82] to describe the isotropic–nematic phase transition in systems of thin rod-like particles. This approach was later extended to study the continuous percolation in fiber systems.[63,64,77] For a given angle ϑ between axes of a pair of SCs, $A_{ex}(\vartheta)$ is the area around a SC where the center of another SC must be located if these SCs intersect each other. The derivation of the excluded area for SCs can be found in the literature.[63] Therefore, all necessary terms are only briefly introduced below.

There are four types of junctions between two SCs on the plane Oxy (Fig. 8). The criterion for the type identification is based

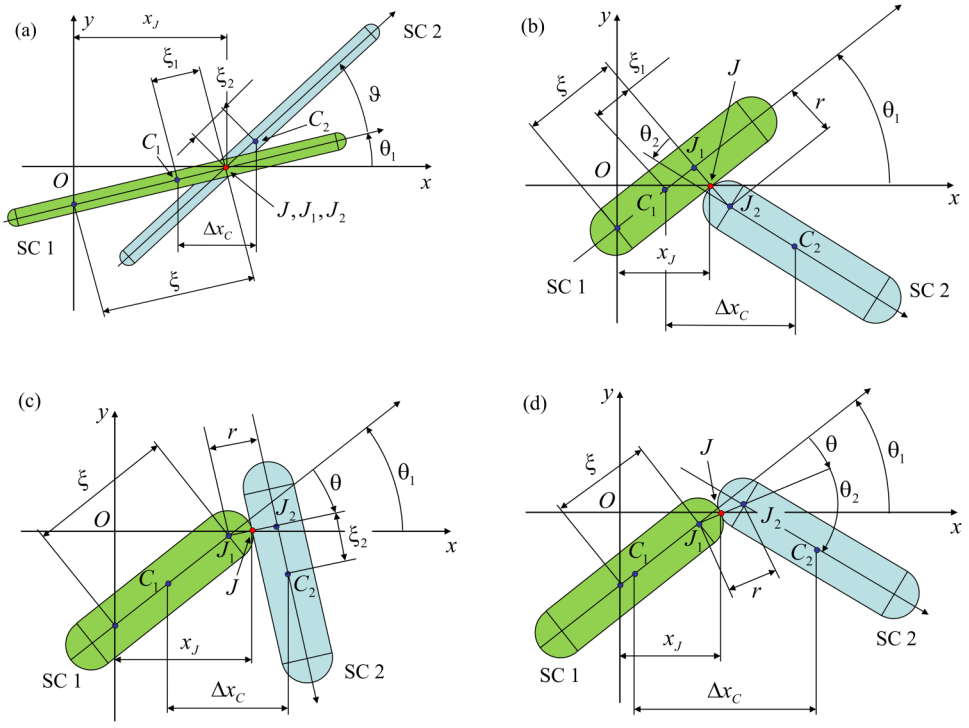

FIG. 8. Different types of junctions of soft-core SCs on the plane Oxy. The junction type is determined by the position of the closest points that are located on SCs' axes within their cylindrical (rectangular in 2D) parts. For junctions of type 1 shown in panel (a), the closest points coincide with each other. For junctions of types 2 and 3 shown in panels (b) and (c), one of the closest points lies at the end of the cylindrical part of a SC. For junctions of type 4 shown in panel (d), both of the closest points are located at the ends of the cylindrical parts of SCs. The notation of geometrical parameters corresponds to the notation used in Appendixes A–C. In panels (b)–(d), only a special case of $r = 2R_f$ is shown for the sake of clarity. The definitions of all geometrical parameters in these panels, however, are valid in the general case of arbitrary r, as explained in the caption of Fig. 2.

on the positions of the closest points J_1 and J_2 of SCs 1 and 2, which are located on the SC axis within the rectangular parts of the SCs. For junctions of type 1, Fig. 8(a), both the closest points lie within the rectangular parts and coincide with each other. For these junctions, the excluded area is the area of the parallelogram *ABCD* in Fig. 9 and is equal to $A_{ex(1)}(\vartheta) = L_f^2|\sin\vartheta|$, where ϑ is the angle between the SC axes. Assuming a homogeneous distribution of ϑ, the excluded area averaged over all possible orientations of SCs in this case is equal to $A_{ex(1)} = \langle A_{ex(1)}(\vartheta)\rangle = (2/\pi)L_f^2$. For junctions of type 2 [Fig. 8(b)], the closest point J_1 is located inside the rectangular part of one SC, while the point J_2 coincides with the center of the semicircular capping of another SC. The excluded area for these junctions, $A_{ex(2)} = 4L_f R_f$, is equal to the sum of areas of rectangles *ADLE* and *BHIC* in Fig. 9. In a junction of type 3 [Fig. 8(c)], SCs 1 and 2 are swapped as compared with a junction of type 2, and the excluded area is equal to the sum of areas of rectangles *CJKD* and *AFGB* in Fig. 9, i.e., $A_{ex(3)} = 4L_f R_f$. For junctions of type 4 [Fig. 8(d)], the closest distance is realized between the centers of capping semicircles of both SCs, so that the excluded area in this case is the area of four circular segments in Fig. 9, $A_{ex(4)} = 4\pi R_f^2$. The total excluded area is then equal to

$$\begin{aligned} A_{ex} &= A_{ex(1)} + A_{ex(2)} + A_{ex(3)} + A_{ex(4)} \\ &= \frac{2}{\pi}L_f^2(1 + 4\pi\bar{R}_f + 2\pi^2\bar{R}_f^2). \end{aligned} \tag{21}$$

By assuming that the positions of the SC centers are homogeneously distributed within the sample, one can find that

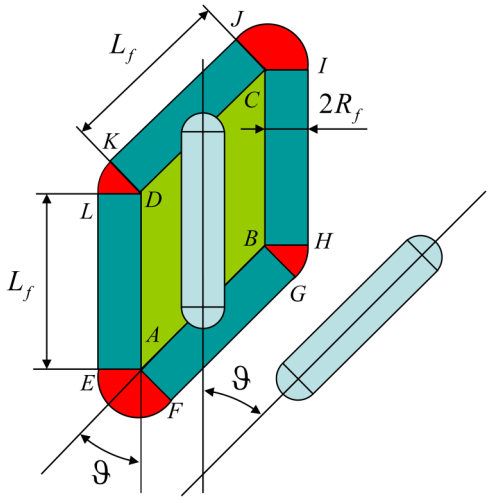

FIG. 9. Schematic representation of the excluded area *EFGHIJKL* for two SCs with the angle ϑ between their axes. The parts of the excluded area shaded by different colors correspond to the different types of junctions shown in individual panels of Fig. 8. The case of Fig. 8(a) is realized if the center of the second SC is in the area *ABCD*, the case of Fig. 8(b) corresponds to the areas *BHIC* and *ADLE*, the case of Fig. 8(c) corresponds to the areas *AFGB* and *CJKD*, and the case of Fig. 8(d) corresponds to the areas *AEF*, *BGH*, *CIJ*, and *DKL*. The idea of this figure is taken from Ref. 63.

$P_J = A_{ex}/L_S^2$ and

$$\langle N_J\rangle = \frac{2}{\pi}\bar{n}_S(1 + 4\pi\bar{R}_f + 2\pi^2\bar{R}_f^2). \tag{22}$$

The parameters $\langle N_x\rangle$ and $\langle N_J\rangle$ are purely geometrical parameters, and Eqs. (19) and (22) do not rely on any assumptions except the assumption of homogeneous distributions of positions and orientations of SCs.

The temperature difference $\langle\Delta T_{(+)}\rangle$ depends, in general, on fluctuations caused by the random structure of a sample. The role of these fluctuations increases in the vicinity of the percolation threshold. In the opposite limit of the high-density approximation, one can assume that all SCs are well-interconnected with each other, and the temperature of a SC depends only on the position of the SC center within the sample. Based on this assumption, in the limit of $\bar{n}_S \to \infty$, the temperature of any SC can be calculated as the average material temperature at the point corresponding to the SC center,

$$T_i = T_0 + \nabla T_x x_{C_i}. \tag{23}$$

By inserting Eq. (23) into the right-hand side of Eq. (15), one can find that

$$\begin{aligned} \langle\Delta T_{(+)}\rangle_\infty^0 &= \frac{\nabla T_x L_f}{\langle N_{J(+)}\rangle}\left\langle\sum_{i=1}^{N}\chi_i(x)\sum_{j=1}^{N}\delta_{ij(+)}(x)\frac{x_{C_j} - x_{C_i}}{L_f}\right\rangle \\ &= \nabla T_x L_f\langle\Delta\bar{x}_{(+)}\rangle, \end{aligned} \tag{24}$$

where $\langle\Delta\bar{x}_{(+)}\rangle$ is the average dimensionless inter-center distance along the axis *Ox*, and the superscript "0" and subscript "∞" indicate that Eq. (24) is obtained for $\mathrm{Bi}_c = 0$ and $\bar{n}_S \to \infty$. The value of $\langle\Delta\bar{x}_{(+)}\rangle$ is a pure geometrical parameter, like $\langle N_x\rangle$ and $\langle N_J\rangle$. The approach used for calculation of $\langle\Delta\bar{x}_{(+)}\rangle$ is briefly described in Appendix A, while the detailed derivation of an equation for this quantity is provided in Sec. SI in the supplementary material, where $\langle\Delta\bar{x}_{(+)}\rangle$ is expressed in the form of Eq. (S24). By inserting Eq. (S24) in the supplementary material into Eq. (24), one can write

$$\begin{aligned} \langle\Delta\bar{T}_{(+)}\rangle_\infty^0 &= \langle\Delta\bar{x}_{(+)}\rangle \\ &= \frac{\pi}{24}\frac{1 + 8\pi\bar{R}_f + (72 + 6\pi^2)\bar{R}_f^2 + 96\pi\bar{R}_f^3 + 24\pi^2\bar{R}_f^4}{(1 + \pi\bar{R}_f)(1 + 4\pi\bar{R}_f + 2\pi^2\bar{R}_f^2)}. \end{aligned} \tag{25}$$

Within the adopted model of thermal transport, where the heat is transferred among the fiber-like particles through point-like junctions, Eq. (25) is accurate for arbitrary $\bar{R}_f$, e.g., for disks with $L_f = 0$, it gives $\langle\Delta T_{(+)}\rangle_\infty^0 = \nabla T_x R_f/2$. For high-aspect-ratio SCs at $\bar{R}_f \le 0.03$, the contribution of terms with the third and fourth powers of $\bar{R}_f$ in the numerator and denominator in Eq. (25) is less than 0.1% and, for practical purposes, Eq. (25) can be

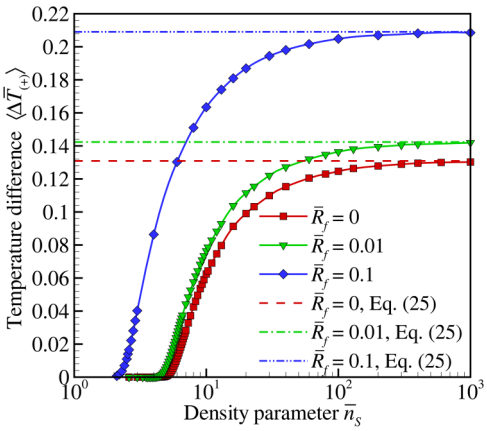

FIG. 10. Averaged temperature difference $\langle \Delta \bar{T}_{(+)} \rangle$ vs density parameter $\bar{n}_S$ calculated at $\mathrm{Bi}_c = 0$ for $\bar{R}_f = 0$ (red squares), $\bar{R}_f = 0.01$ (green gradients), and $\bar{R}_f = 0.1$ (blue diamonds). The symbols and solid curves correspond to the numerical values. The horizontal lines show the values calculated based on Eq. (25).

approximated in this range of $\bar{R}_f$ as

$$\langle \Delta \bar{T}_{(+)} \rangle_\infty^0 \approx \frac{\pi}{24} \frac{1 + 8\pi \bar{R}_f + (72 + 6\pi^2)\bar{R}_f^2}{1 + 5\pi \bar{R}_f + 6\pi^2 \bar{R}_f^2} = \frac{\pi}{24} \left(1 + \bar{R}_f \frac{3\pi + 72\, \bar{R}_f}{1 + 5\pi \bar{R}_f + 6\pi^2 \bar{R}_f^2} \right). \quad (26)$$

In order to establish the range of applicability of the assumption given by Eq. (23) and to find the range of $\bar{n}_S$ where $\langle \Delta \bar{T}_{(+)} \rangle$ can be described by Eq. (25), the values of the temperature difference were calculated numerically based on Eq. (15). The results of these calculations, shown by symbols in Fig. 10, demonstrate that $\langle \Delta \bar{T}_{(+)} \rangle$ quickly approaches the limiting values predicted by Eq. (25) for $\bar{n}_S \to \infty$ (horizontal lines in Fig. 10).[83] For example, the difference between the prediction of Eq. (25) and numerical values of $\langle \Delta \bar{T}_{(+)} \rangle$ is smaller than 0.5% at $\bar{n}_S \geq 10^3$, smaller than 3% at $\bar{n}_S \geq 10^2$, and smaller than 20% at $\bar{n}_S \geq 30$. Thus, the assumption given by Eq. (23) provides a reasonably accurate description of the temperature difference at junctions when $\bar{n}_S \geq 30 - 100$. Along with the data shown in Fig. 10, additional simulations were performed for $\bar{R}_f = 1$, and numerical data were found to be in an excellent agreement with Eq. (25) in the limit of large $\bar{n}_S$.

With decreasing $\bar{n}_S$, $\langle \Delta \bar{T}_{(+)} \rangle$ first gradually decreases at moderate $\bar{n}_S$ and then drops sharply close to the percolation threshold. The average temperature difference is varied continuously around the percolation threshold, with nonzero values predicted even below $\bar{n}_{SP}$. This artifact is caused by the finite sample sizes $\hat{L}_S$ used in the calculations. With an increase in the sample size, the plots of $\langle \Delta \bar{T}_{(+)} \rangle$ become steeper in a vicinity of the percolation threshold, while the effect of the sample size appears to become negligible at $\bar{n}_S \gg \bar{n}_{SP}$. For example, the difference between $\langle \Delta \bar{T}_{(+)} \rangle$ obtained at $\hat{L}_S = 32$ and $\hat{L}_S = 4$ becomes less than 1% for $\bar{n}_S \geq 20$.

By inserting Eqs. (19), (23), and (25) into Eq. (17), one can find

$$k_\infty^0 = \sigma_c C_0^0(\bar{R}_f) \bar{n}_S^2 = \sigma_c \frac{C_0^0(\bar{R}_f)}{(2 + \pi \bar{R}_f)^2} \varphi_S^2 \left(\frac{L_f}{R_f} \right)^2, \quad (27)$$

where $\varphi_S = n_S(2L_f R_f + \pi R_f^2) = \bar{n}_S \bar{R}_f (2 + \pi \bar{R}_f)$ is the fiber surface coverage and

$$C_0^0(\bar{R}_f) = \frac{1}{12\pi}(1 + 8\pi \bar{R}_f + (72 + 6\pi^2)\bar{R}_f^2 + 96\pi \bar{R}_f^3 + 24\pi^2 \bar{R}_f^4). \quad (28)$$

The values of the conductivity predicted by Eq. (27) are shown by the lines in Fig. 7. One can see that Eq. (27) accurately describes asymptotic behavior of the thermal conductivity in high-density materials. The quadratic dependence of k_∞^0 on $\bar{n}_S$, or on both φ_S and L_f at $R_f = \text{const} \ll L_f$, in the high-density approximation is a result of a combination of the following scaling relationships: $\langle N_x \rangle L_y \propto \bar{n}_S / L_f$, $\langle N_J \rangle \propto \bar{n}_S$, and $\langle \Delta T_{(+)} \rangle \propto L_f$. This quadratic scaling law, first established in Ref. 53 and then confirmed in Ref. 56, is quite different from the scaling law for fibrous materials with negligibly small interfiber contact resistance, where the conductivity is proportional to φ_S and is independent of L_f, e.g., Ref. 3 and Eq. (68) in Sec. VIII A. Equation (27) can be reformulated to express k as a function of the material surface density ρ_S. For high-aspect-ratio fibers, when the mass of caps can be neglected, $\rho_S = \rho_f L_f n_S$, where the ρ_f is the linear density of the fiber material (mass per unit length of the fiber). Then, $k_\infty^0 = \sigma_c C_0^0(\bar{R}_f)(\rho_S L_f)^2 / \rho_f^2$, i.e., k_∞^0 scales quadratically with the material density ρ_S. At $\bar{R}_f \to 0$, $C_0^0(\bar{R}_f) \to 1/(12\pi)$ and the conductivity of slender rods is equal to

$$k_\infty^0 = \sigma_c \frac{(n_S L_f^2)^2}{12\pi}. \quad (29)$$

With increasing $\bar{R}_f$, the contribution of terms proportional to $\bar{R}_f$ and $\bar{R}_f^2$ in Eq. (28) rapidly increases. For example, at $\bar{R}_f = 0.01$, the term proportional to $\bar{R}_f$ increases the conductivity by ~24% with respect to the first radius-independent term, while the term proportional to $\bar{R}_f^2$ gives an additional rise by ~4%. The terms proportional to $\bar{R}_f^3$ and $\bar{R}_f^4$ are much smaller and can be neglected at $\bar{R}_f < 0.03$. For disk particles with $L_f = 0$, Eq. (27) reduces to

$$k_\infty^0 = \sigma_c 2\pi (n_S R_f^2)^2. \quad (30)$$

B. Role of fluctuations of fiber temperature. Correction of the conductivity equation for semidilute networks

In this section, we derive a semiempirical correction to Eq. (27), which is capable of predicting the thermal conductivity of semidilute fiber networks with moderate, $\bar{n}_S \sim 10$, density parameters. Since Eqs. (19) and (22) are valid for any $\bar{n}_S$, the deviation of k from k_∞^0 at $\bar{n}_S$ approaching the percolation threshold (Fig. 7) can

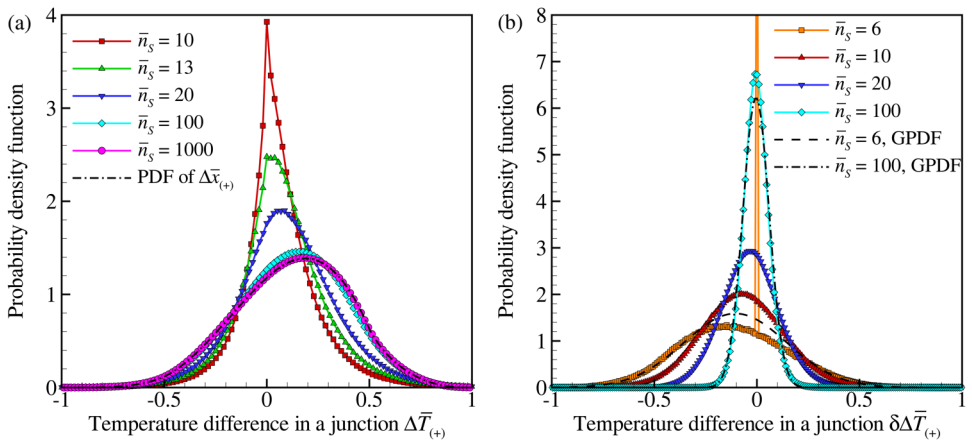

FIG. 11. PDFs of $\Delta\bar{T}_{(+)}$ (a) and $\delta\Delta\bar{T}_{(+)} = \Delta\bar{T}_{(+)} - \Delta\bar{T}^0_{(+)\infty}$ (b) for various density parameters $\bar{n}_S$ at $\bar{R}_f = 0$ and $\mathrm{Bi}_c = 0$. In panel (a), the dashed-dotted curve corresponds to the PDF of $\Delta\bar{T}^0_{(+)\infty} = \Delta\bar{x}_{(+)}$, which is independent of $\bar{n}_S$. This dashed-dotted curve visually coincides with the PDF of $\Delta\bar{T}_{(+)}$ at $\bar{n}_S = 1000$. In panel (b), the dashed and dashed-dotted curves represent the Gaussian PDF (GPDF) plotted for the same values of the expectation and root mean square deviation as the corresponding PDFs found numerically. In panel (b), the sharp peak at $\delta\Delta\bar{T}_{(+)} = 0$ of the PDF for $\bar{n}_S = 6$ corresponds to junctions between fibers belonging to non-percolating clusters, where the temperature difference is zero. For such junctions, $\delta\Delta\bar{T}_{(+)}$ is not calculated based on the definition given by Eq. (31) but is assumed to be equal to zero.

only be attributed to the deviation of $\langle\Delta\bar{T}_{(+)}\rangle$ from the values given by Eq. (25). This deviation is illustrated in Fig. 10 and is a result of an increasing effect of fluctuations and correlations of SC temperatures with decreasing $\bar{n}_S$, when the network gradually disintegrates into quasi-clusters. Temperatures of SCs in these quasi-clusters are well-correlated. Close to the percolation threshold, the network breaks up into poorly connected quasi-clusters, with individual fibers in each quasi-cluster having almost the same temperature, so that $\langle\Delta\bar{T}_{(+)}\rangle$ approaches zero.

The analysis of distributions of temperature differences at junctions computed for different $\bar{n}_S$ supports this explanation. At $\bar{n}_S = 1000$, the PDF of $\Delta\bar{T}_{(+)}$, where $\Delta T_{(+)} = T_j - T_i$ is the temperature difference at a junction between a pair of SCs with $\chi_i(0) = 1$ and $\delta_{ij(+)}(0) = 1$, practically coincides with the PDF of $\Delta\bar{x}_{(+)}$, where $\Delta x_{(+)} = x_{C_j} - x_{C_i}$ is the inter-center distance in a junction between a pair of SCs with $\chi_i(0) = 1$ and $\delta_{ij(+)}(0) = 1$ (Fig. 11). With decreasing $\bar{n}_S$, the maximum of the PDF of $\Delta\bar{T}_{(+)}$ shifts toward $\Delta\bar{T}_{(+)} = 0$ and, when $\bar{n}_S$ gets smaller than some critical value, the PDF becomes nonsmooth around $\Delta\bar{T}_{(+)} = 0$ [curves for $\bar{n}_S = 10$ and $\bar{n}_S = 13$ in Fig. 11(a)]. The spike in the PDF at $\Delta\bar{T}_{(+)} = 0$ indicates the presence of a finite fraction of junctions with zero temperature difference. To estimate the role of correlation of SC temperatures due to clustering, we additionally introduce a quantity $\delta T_i = T_i - (T_0 + \nabla T_x x_{C_i})$, which characterizes the deviation of the real temperature T_i of SC i from the approximate value given by Eq. (23). Pearson's correlation coefficient $\rho(\delta T_i, \delta T_j)$ found numerically for all pairs of SCs that are linked by a junction is close to 1 near the percolation threshold and decreases with an increase in $\bar{n}_S$ (Fig. 12).

The deviation of the real dimensionless temperature difference at a junction, $\Delta\bar{T}_{(+)}$, from its value in the high-density approximation, $\Delta\bar{T}^0_{(+)\infty} = (x_{C_j} - x_{C_i})/L_f$, can be characterized by the quantity

$$\delta\Delta\bar{T}_{(+)} = \Delta\bar{T}_{(+)} - \Delta\bar{T}^0_{(+)\infty}. \tag{31}$$

The analysis of a typical numerical PDFs of $\delta\Delta\bar{T}_{(+)}$ [Fig. 11(b)] indicates that the root mean square deviation (RMSD) of $\delta\Delta\bar{T}_{(+)}$ decreases with increasing $\bar{n}_S$ and the PDFs approach the Dirac δ-function at $\bar{n}_S \to \infty$. With a decrease in $\bar{n}_S$, distributions of $\delta\Delta\bar{T}_{(+)}$ become broader, while the mean value changes from zero

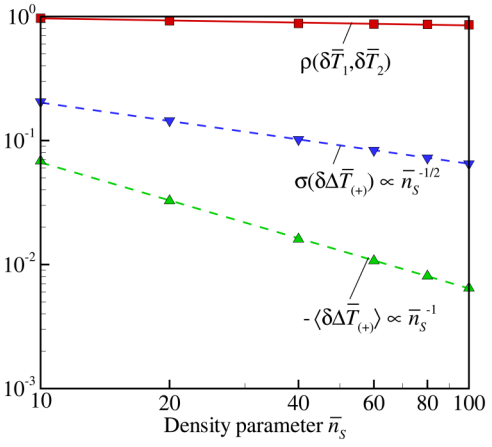

FIG. 12. Pearson's correlation coefficient $\rho(\delta\bar{T}_1, \delta\bar{T}_2)$ (red squares), expectation value $\langle\delta\Delta\bar{T}_{(+)}\rangle$ (green triangles), and root mean square deviation $\sigma(\delta\Delta\bar{T}_{(+)})$ (blue gradients) vs density parameter $\bar{n}_S$ at $\bar{R}_f = 0$ and $\mathrm{Bi}_c = 0$. All values are calculated for SCs that intersect the line $x = 0$ in samples with $\hat{L}_S = 16$. The symbols represent numerical values. The dashed curves are power-law fits to the numerical values.

to $-\langle\Delta\bar{T}_{(+)}\rangle^0_\infty$. The comparison of the numerical PDFs with corresponding Gaussian distributions, plotted for the same mean value and RMSD and shown by the dashed and dashed-dotted curves in Fig. 11(b), shows that the real PDFs exhibit substantial deviations from the Gaussian distributions for both small and large $\bar{n}_S$. The mean value, $\langle\delta\Delta\bar{T}_{(+)}\rangle$, and RMSD, $\sigma(\delta\Delta\bar{T}_{(+)})$, both approach zero at $\bar{n}_S \to \infty$ as $\sim 1/\bar{n}_S$ and $\sim 1/\sqrt{\bar{n}_S}$, respectively (Fig. 12). This observation suggests that $\langle\delta\Delta\bar{T}_{(+)}\rangle$ can be represented as a series expansion in powers of a small parameter $1/\bar{n}_S$ near $\langle\delta\Delta\bar{T}_{(+)}\rangle = 0$,

$$-\langle\delta\Delta\bar{T}_{(+)}\rangle^0 = \frac{\tilde{C}_1^0(\bar{R}_f)}{\bar{n}_S} + \frac{\tilde{C}_2^0(\bar{R}_f)}{\bar{n}_S^2} + \cdots, \tag{32}$$

where the superscript "0" indicates that this equation is applied at $\mathrm{Bi}_c = 0$. If one retains only the first term in this series, i.e.,

$$\langle\delta\Delta\bar{T}_{(+)}\rangle^0 = -\frac{\tilde{C}_1^0(\bar{R}_f)}{\bar{n}_S}, \tag{33}$$

then the prefactor $\tilde{C}_1^0(\bar{R}_f)$ can be found by fitting Eq. (33) to numerical data by the least-squares method. Our calculations show that Eq. (33) can be fitted to numerical data in the range $\bar{n}_S > \bar{n}_{S\max} = 8$ with $\tilde{C}_1^0(0) = 0.69$. As $\bar{n}_S$ increases above $\bar{n}_{S\max}$, however, the value of $\tilde{C}_1^0(0)$ that ensures a good data fit by Eq. (33) approaches $2/\pi$. This behavior is expected, because the contribution of the second and higher order terms in the power series expansion given by Eq. (32) becomes smaller for larger $\bar{n}_S$. After inserting Eq. (33) into Eq. (31) and performing ensemble averaging, one can find that

$$\langle\Delta\bar{T}_{(+)}\rangle^0 = \langle\Delta\bar{T}_{(+)}\rangle^0_\infty + \langle\delta\Delta\bar{T}_{(+)}\rangle^0 = \langle\Delta\bar{x}_{(+)}\rangle - \frac{\tilde{C}_1^0(\bar{R}_f)}{\bar{n}_S}. \tag{34}$$

The predictions of Eq. (34) for $\tilde{C}_1^0(0) = 0.69$ and $\tilde{C}_1^0(0) = 2/\pi$ are shown in Figs. 13(a) and 13(b) by solid and dashed curves, respectively. The former choice of $\tilde{C}_1^0(0)$ provides better approximation at small $\bar{n}_S < 20$ and inferior approximation at $20 < \bar{n}_S < 10^2$ as compared to the latter value of $\tilde{C}_1^0(0)$. On the other hand, the latter choice provides an excellent approximation for $\bar{n}_S > 20$ with the deviation from the numerical results staying below 0.6%. Therefore, the value of $\tilde{C}_1^0(0) = 2/\pi$ is adopted here for further use. Analysis of the numerical data for various $\bar{R}_f$ shows that $\tilde{C}_1^0(\bar{R}_f)$ can be approximated by the following equation:

$$\tilde{C}_1^0(\bar{R}_f) = \frac{2}{\pi}\frac{1}{1+\pi\bar{R}_f}. \tag{35}$$

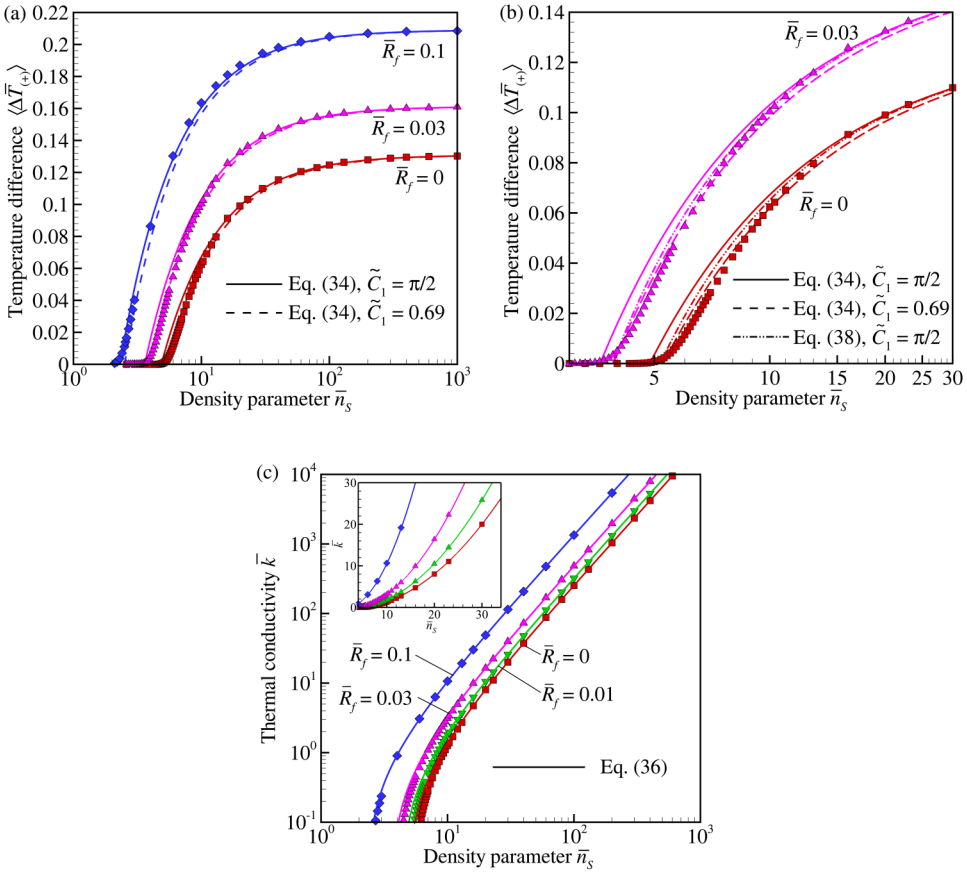

FIG. 13. Average temperature difference at junctions $\langle\Delta\bar{T}_{(+)}\rangle$ [(a) and (b)] and thermal conductivity $\bar{k}$ (c) vs density parameter $\bar{n}_S$ at $\mathrm{Bi}_c = 0$. The symbols represent values calculated numerically at $\bar{R}_f = 0$ (red squares), $\bar{R}_f = 0.01$ (green gradients), $\bar{R}_f = 0.03$ (magenta triangles), and $\bar{R}_f = 0.1$ (blue diamonds). In panels (a) and (b), the solid and dashed curves are obtained with Eq. (34) at $\tilde{C}_1(0) = 2/\pi \approx 0.64$ and $\tilde{C}_1(0) = 0.69$, while the dashed-dotted curves are obtained with Eq. (38) at $\tilde{C}_1(0) = 2/\pi$. In panel (c), the solid curves are obtained with Eq. (36). The inset in panel (c) shows values of $\bar{k}$ in the intermediate range of $\bar{n}_S$. It reveals that Eq. (36) provides an excellent approximation of numerical values at $\bar{n}_S \geq 5$.

After inserting Eqs. (19), (22), and (34) into Eq. (17), the latter reduces to

$$k^0 = \sigma_c C_0^0(\bar{R}_f)\bar{n}_S^2 - \sigma_c C_1^0(\bar{R}_f)\bar{n}_S = k_\infty^0 - \sigma_c C_1^0(\bar{R}_f)\bar{n}_S, \quad (36)$$

where the prefactor $C_1^0(\bar{R}_f)$ is equal to

$$C_1^0(\bar{R}_f) = \frac{L_f}{L_y}\frac{\langle N_x\rangle\langle N_J\rangle}{2\bar{n}_S^2}\tilde{C}_1^0(\bar{R}_f) = \frac{4}{\pi^3}(1 + 4\pi\bar{R}_f + 2\pi^2\bar{R}_f^2). \quad (37)$$

The comparison of values of $\bar{k}$ calculated with Eq. (36) [solid curved in Fig. 13(c)] with numerical values [symbols in Fig. 13(c)], demonstrates that the error of Eq. (36) is less than 0.5% at $\bar{n}_S \geq 16$, 4% at $\bar{n}_S \geq 13$, and 22% at $\bar{n}_S \geq 8$. Thus, the second and following terms in the power series expansion given by Eq. (32) make a substantial contribution to $\bar{k}$ only close to the percolation threshold. Similar first-order corrections for finite $\bar{n}_S$ were proposed in Refs. 53 and 57.

Further analysis of the simulation results showed that $\tilde{C}_2^0(\bar{R}_f) \approx \tilde{C}_1^0(\bar{R}_f)/2$. This observation provides a hint that the series in Eq. (32) can be approximated by the Tailor expansion of the exponential function and, therefore, Eq. (20) can be replaced by $\langle\delta\Delta\bar{T}_{(+)}\rangle^0 = 1 - \exp(\tilde{C}_1^0(\bar{R}_f)/\bar{n}_S)$, yielding

$$\langle\Delta\bar{T}_{(+)}\rangle^0 = \langle\Delta\bar{x}_{(+)}\rangle + 1 - \exp(\tilde{C}_1^0(\bar{R}_f)/\bar{n}_S). \quad (38)$$

The predictions based on this equation are shown in Fig. 13(b) by dashed-dotted curves. One can see that this equation gives the same results as Eq. (34) at $\bar{n}_S > 15$, while for smaller density parameters, Eq. (38) provides about twice smaller error than Eq. (34).

VII. COMPUTATIONAL RESULTS FOR FIBER NETWORKS WITH FINITE INTRINSIC CONDUCTIVITY OF FIBERS

In the case of finite intrinsic conductivity of fibers, the patterns of the SC temperature become more homogeneous in the direction perpendicular to the direction of the heat flux. For example, one can compare the temperature pattern obtained at $\mathrm{Bi}_c = 10$ and shown in Fig. 14 with the corresponding pattern obtained at $\mathrm{Bi}_c = 0$ and shown in Fig. 5(e). The main difference between these patterns is the constancy of temperature of every SC in the latter case, while some nonzero temperature gradient is maintained along SCs in the former one.

The typical distributions of temperature along SCs in a dense network of slender rods as functions of the coordinate x are shown by solid curves in Fig. 15. As one can see, at sufficiently large $\bar{n}_S$ and Bi_c, dT_i/dx is approximately constant along SCs. Based on this fact, an approximate equation for $\bar{k}$ at arbitrary Bi_c and $\bar{R}_f = 0$ was obtained in Ref. 59. In a generalized form, accounting for finite values of $\bar{n}_S$, such an equation is derived in Sec. SIV in the supplementary material [Eq. (S70)]. Visually, the distributions of temperature along SCs are rather smooth contrary to an expectation that they should be piecewise-linear with jumps in the slope in the points of interfiber junctions. This is explained by a relatively high value of $\bar{n}_S$ in the network shown in Fig. 15, where the average number of junctions $\langle N_J\rangle$ is as high as 93.9. At much

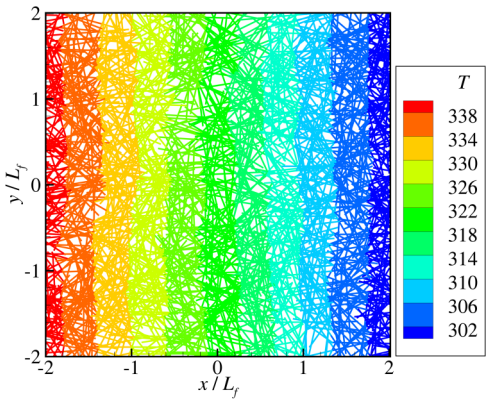

FIG. 14. Pattern of SC temperatures in a sample generated at $\bar{n}_S = 73.7$, $\bar{R}_f = 0$, and $\mathrm{Bi}_c = 10$. The individual SCs are colored according to their local temperature that is measured in arbitrary units. The pattern of SC temperatures obtained for the same $\bar{n}_S$ and $\bar{R}_f$ but with $\mathrm{Bi}_c = 0$ is shown in Fig. 5(e).

smaller values of $\bar{n}_S$, the distributions of temperature along individual SCs retain a pronounced piecewise-linear character.

As can be seen from Fig. 16(a), for any density, $\bar{k}$ decreases from its maximum at $\mathrm{Bi}_c = 0$ with decreasing intrinsic conductivity of fibers. At a finite Bi_c, the dependence $\bar{k}(\bar{n}_S)$ for slender rods at $\bar{n}_S \gg 1$ demonstrates a different asymptotic behavior as compared to the case of $\mathrm{Bi}_c = 0$: $\bar{k} \propto \bar{n}_S$ at $\mathrm{Bi}_c > 0$, while the scaling law $\bar{k} \propto \bar{n}_S^2$ holds at $\mathrm{Bi}_c = 0$. The rate the actual function $\bar{k}(\bar{n}_S)$ approaches its asymptote $\bar{k} \propto \bar{n}_S$ decreases with decreasing Biot number. This result suggests a possible explanation of the scaling law $k \propto L_f^{1.46}$ for the electrical conductivity of CNT networks found experimentally.[51] The value of the exponent, which is intermediate between 1 and 2, may indicate that the electrical

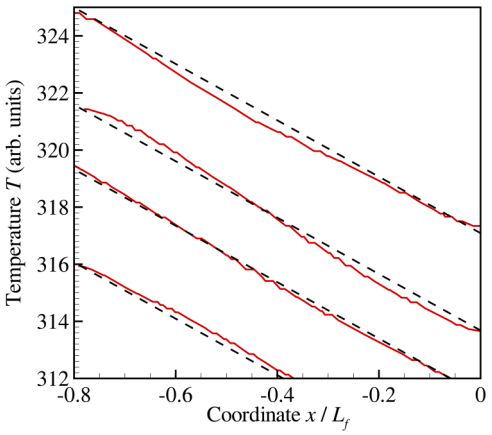

FIG. 15. The distributions of temperature along four representative fibers (solid curves) in a sample with $\bar{n}_S = 147.4$, $\bar{R}_f = 0$, and $\mathrm{Bi}_c = 10$. The distributions are shown as functions of the sample coordinate x (Fig. 14). The slope of the dashed lines is equal to the average gradient ∇T_{fx} calculated with Eq. (54).

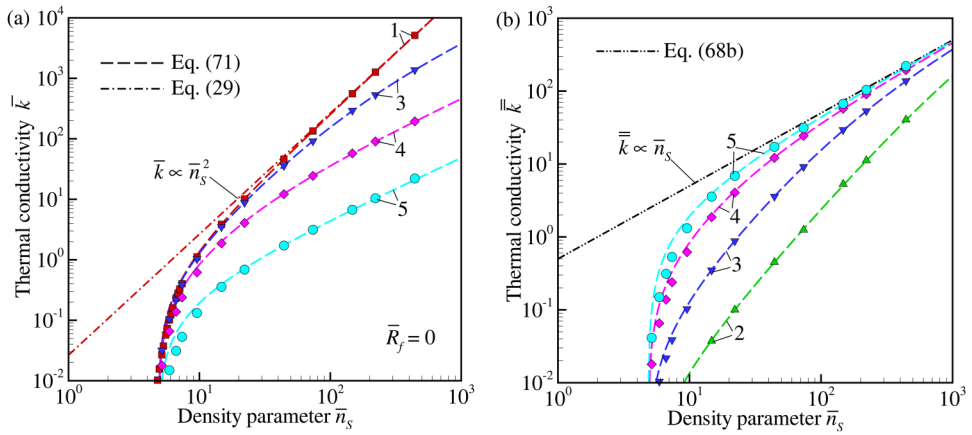

FIG. 16. Dimensionless thermal conductivity in the form of $\bar{k} = k/\sigma_c$ (a) and $\bar{\bar{k}} = k/\sigma_f = \bar{k} \times \mathrm{Bi}_c$ (b) vs density parameter $\bar{n}_S$ for slender rods ($\bar{R}_f = 0$) at $\mathrm{Bi}_c = 0$ (red squares and curve 1), $\mathrm{Bi}_c = 0.01$ (green triangles and curve 2), $\mathrm{Bi}_c = 0.1$ (blue gradients and curves 3), $\mathrm{Bi}_c = 1$ (magenta diamonds and curves 4), and $\mathrm{Bi}_c = 10$ (cyan circles and curves 5). The symbols represent numerical values. The dashed curves are calculated with Eq. (71). In panel (a), the dashed-dotted curve is obtained with Eq. (29) that describes conductivity at $\mathrm{Bi}_c = 0$. In panel (b), the dashed-double-dotted curve is obtained with Eq. (68b) that describes conductivity at $\mathrm{Bi}_c \to \infty$.

analog of the Biot number is about 1, when the dependence $\bar{k}(\bar{n}_S)$ at moderate $\bar{n}_S$ can be approximated neither by the scaling law $\bar{k} \propto \bar{n}_S$ nor $\bar{k} \propto \bar{n}_S^2$.

In order to make the asymptotic behavior of the thermal conductivity at finite Bi_c more apparent, one can introduce the dimensionless conductivity $\bar{\bar{k}} = k/\sigma_f = \bar{k} \times \mathrm{Bi}_c$ by using the intrinsic fiber conductance σ_f as a more suitable scale for conductivity at $\mathrm{Bi}_c \gg 1$ than σ_c. As can be seen from Fig. 16(b), for finite Bi_c, the function $\bar{\bar{k}}(\bar{n}_S)$ approaches a single asymptote at $\bar{n}_S \to \infty$ shown by the dashed-double-dotted line. This line corresponds to the scaling law $\bar{\bar{k}} \propto \bar{n}_S$ in the limiting case of $\mathrm{Bi}_c \to \infty$, when the effect of interfiber contact resistance is negligible.

In spite of such asymptotic behavior, for networks of slender rods at very large but finite $\bar{n}_S$, the scaling of conductivity with $\bar{n}_S$ also depends on Bi_c. At a sufficiently small Bi_c, e.g., $\mathrm{Bi}_c = 0.01$ (curve 2 in Fig. 16), the thermal conductivity is better approximated by the scaling law $\bar{k} \propto \bar{n}_S^2$ established for $\mathrm{Bi}_c = 0$ than by the linear dependence for finite Bi_c even when $\bar{n}_S$ is as large as 10^3. This observation shows that the consideration of the limiting case of infinitely large intrinsic conductivity of SCs can yield results applicable to real systems with finite $\bar{n}_S$ and Bi_c.

The thermal conductivity of slender rods as a function of the Biot number is shown in Fig. 17. This plot illustrates the expected variation of $\bar{k}$ between two limiting cases corresponding to $\mathrm{Bi}_c \to 0$ and $\mathrm{Bi}_c \to \infty$. At $\mathrm{Bi}_c \to 0$, the values of $\bar{k}$ at fixed $\bar{n}_S$ approach horizontal asymptotes corresponding to the values of k in the limit of infinitely large intrinsic conductivity of fibers. At $\mathrm{Bi}_c \to \infty$, $\bar{k}$ decreases linearly with Bi_c, since in this case the reduced conductivity in the form $\bar{\bar{k}} = \bar{k} \times \mathrm{Bi}_c$ must approach the horizontal asymptotes corresponding to the values of k in the limit of infinitely large contact conductance. The obtained results show, however, that the range of Bi_c where this transition occurs is not constant but depends on $\bar{n}_S$. With increasing $\bar{n}_S$, this transitional range of Bi_c moves toward smaller Biot numbers.

At relatively small $\bar{R}_f$, e.g., at $\bar{R}_f = 0.01$, the conductivity curves in the range $\bar{n}_S \le 10^3$ are qualitatively similar to those for slender rods (Fig. 18). With further increase in $\bar{R}_f$, the behavior of $\bar{k}$ as a function of $\bar{n}_S$ becomes qualitatively different from the case $\bar{R}_f = 0$ (Fig. 19). The quadratic scaling law for conductivity, $\bar{k} \propto \bar{n}_S^2$ at large $\bar{n}_S$, holds at arbitrary Bi_c, although for semidilute networks ($\bar{n}_S = 10 - 10^2$), an increase in Bi_c can significantly decrease $\bar{k}$. For example, at $\bar{R}_f = 0.1$ and $\bar{n}_S = 10$, $\bar{k}$ drops by more than two orders of magnitude when Bi_c increases from 1 to 10^3. At a constant $\bar{R}_f$ and $\bar{n}_S \to \infty$,

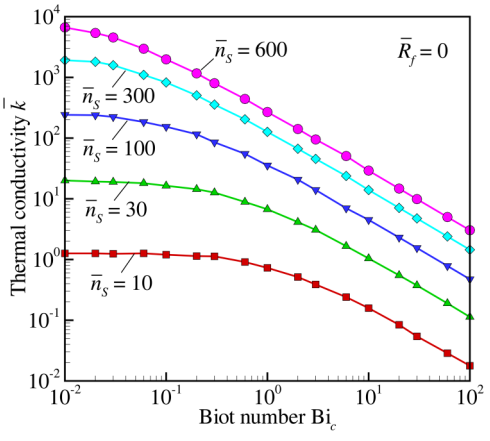

FIG. 17. Dimensionless thermal conductivity $\bar{k} = k/\sigma_c$ vs Biot number Bi_c for slender rods ($\bar{R}_f = 0$) at $\bar{n}_S = 10$ (red squares), $\bar{n}_S = 30$ (green triangles), $\bar{n}_S = 100$ (blue gradients), $\bar{n}_S = 300$ (cyan diamonds), and $\bar{n}_S = 600$ (magenta circles). The symbols represent values calculated numerically, while the curves are drawn only to guide the eye.

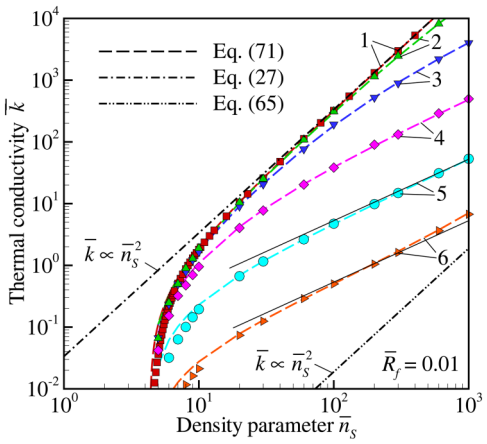

FIG. 18. Dimensionless thermal conductivity $\bar{k}$ vs density parameter $\bar{n}_S$ for $\bar{R}_f = 0.01$ at $\mathrm{Bi}_c = 0$ (red squares and curve 1), $\mathrm{Bi}_c = 0.01$ (green triangles and curve 2), $\mathrm{Bi}_c = 0.1$ (blue gradients and curve 3), $\mathrm{Bi}_c = 1$ (magenta diamonds and curves 4), $\mathrm{Bi}_c = 10$ (cyan circles and curve 5), and $\mathrm{Bi}_c = 100$ (orange right triangles and curve 6). The symbols represent numerical values. The dashed curves are calculated with Eq. (71). The dashed-dotted and dashed-double-dotted curves are calculated with Eqs. (27) and (65), respectively. The thin black lines show the result of fitting the calculated values of conductivity at $\mathrm{Bi}_c = 10$ and $\mathrm{Bi}_c = 100$ to the linear scaling law in limited ranges of $\bar{n}_S$.

the conductivity approaches an asymptote that does not depend on Bi_c.

The results of the numerical calculations discussed above illustrate a rather complex behavior of $\bar{k}$ at finite $\bar{n}_S$ and Bi_c. At $\bar{R}_f = 0$, it is characterized by the transition between two limiting cases of $\mathrm{Bi}_c = 0$ and $\mathrm{Bi}_c \to \infty$ that imply quadratic and linear dependences of $\bar{k}$ on $\bar{n}_S$. At finite $\bar{R}_f$, the asymptotic behavior remains quadratic for dense networks at an arbitrary Bi_c, but the dependence of $\bar{k}$ on $\bar{n}_S$ for semidilute networks become more complicated at finite Bi_c as compared to the case of $\mathrm{Bi}_c = 0$. In dense networks composed of SCs with finite $\bar{R}_f$, the effect of contact resistance does not vanish even in the limit of infinitely large Bi_c.

VIII. THEORETICAL EQUATION FOR CONDUCTIVITY AT FINITE INTRINSIC CONDUCTIVITY OF FIBERS

In this section, we approach the challenging problem of theoretical description of the thermal conductivity for fiber systems composed of finite-aspect-ratio SCs at finite Bi_c. For this purpose, we generalize the approach that was used in Sec. VI for $\mathrm{Bi}_c = 0$. At finite Bi_c, Eq. (17) for conductivity, as well as Eqs. (19) and (22), remain valid, but since the temperature varies along the SC length, the distribution of temperature along a fiber should be determined first in order to find new $\langle \Delta \bar{T}_{(+)} \rangle$. In the high-density approximation, this problem is solved in Sec. VIII A. Next, in Sec. VIII B, we find a correction to the equation derived in Sec. VIII A, which enables calculation of the conductivity for semidilute networks.

A. Theoretical solution for temperature distribution along a fiber and conductivity equation for dense networks

To obtain an equation for the distribution of the average SC temperature, one can use Eq. (8) applied to any SC i, e.g., SC 1. If the angle θ_1 between SC 1 and the axis Ox, as well as the position of the SC center x_{C_1}, are fixed, then, from the symmetry consideration, the distribution of the averaged SC temperature along the coordinate x can be represented as

$$T_{f,\theta_1}(x_1) = T(x_{C_1}) + \tau_{\theta_1}(x_1 - x_{C_1}), \tag{39}$$

where $-(L_f/2)\cos\theta_1 < x_1 - x_{C_1} < (L_f/2)\cos\theta_1$ (for simplicity, only the case of $\cos\theta_1 \geq 0$ is considered here; the obtained solution, however, is valid for an arbitrary θ_1); the temperature at the SC center, $T(x_{C_1})$, is given by Eq. (23); and $\tau_{\theta_1}(x)$ is some odd function, i.e., $\tau_{\theta_1}(-x) = -\tau_{\theta_1}(x)$. Using a dimensionless variable $\bar{\eta} = (x_1 - x_{C_1})/L_f$ and a function $\bar{\tau}_{\theta_1}(\bar{\eta}) = \tau_{\theta_1}(L_f\bar{\eta})/(\nabla T_x L_f)$, one can rewrite Eq. (39) as

$$T_{f,\theta_1}(x_1) = T(x_{C_1}) + \nabla T_x L_f \bar{\tau}_{\theta_1}\left(\frac{x_1 - x_{C_1}}{L_f}\right). \tag{40}$$

A heat transfer equation with respect to $T_{f,\theta_1}(x)$ can be obtained from Eq. (8) after its averaging over all possible positions and orientations of other SCs interacting with SC 1 within $0 < l_1 < L_f$, where only junctions of types 1 and 2 in Fig. 8 contribute to the right-hand side of Eq. (8). The equation with respect to $T_{f,\theta_1}(x_1)$ can then be written in the form

$$\frac{d^2 T_{f,\theta_1}}{dx_1^2} = -\frac{1}{\cos^2\theta_1}\frac{\sigma}{k_f A_f}\frac{\langle N_J\rangle_{(1,2)}}{L_f}\langle \Delta T_{\theta_1}\rangle_{(1,2)}, \tag{41}$$

where $\langle N_J\rangle_{(1,2)}/L_f$ is the total number of junctions of types 1 and 2 per unit length of a SC,

$$\langle N_J\rangle_{(1,2)} = \langle N_J\rangle \frac{A_{\mathrm{ex}(1)} + A_{\mathrm{ex}(2)}}{A_{\mathrm{ex}}} = \bar{n}_S\left(\frac{2}{\pi} + 4\bar{R}_f\right), \tag{42}$$

and $\langle \Delta T_{\theta_1}\rangle_{(1,2)}$ is the average temperature difference in all such junctions. The general approach to evaluation of $\langle \Delta T_{\theta_1}\rangle_{(1,2)}$ is described in Appendix B, while the detailed derivation of this quantity is provided in Sec. SII in the supplementary material. The result, given by Eqs. (B3) and (S40) in the supplementary material, is as follows:

$$\langle \Delta T_{\theta_1}\rangle_{(1,2)} = \nabla T_x(x_1 - x_{C_1}) - \tau_{\theta_1}(x_1 - x_{C_1}). \tag{43}$$

By inserting Eqs. (42) and (43) into the right-hand side of Eq. (41), one can find the equation with respect to $\bar{\tau}_{\theta_1}(\bar{\eta})$,

$$\frac{d^2\bar{\tau}_{\theta_1}}{d\bar{\eta}^2} = \frac{C^2}{\cos^2\theta_1}(\bar{\tau}_{\theta_1} - \bar{\eta}), \tag{44}$$

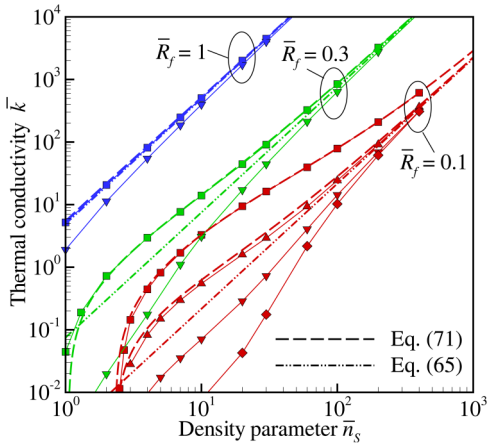

FIG. 19. Thermal conductivity $\bar{k}$ vs density parameter $\bar{n}_S$ for $\bar{R}_f = 0.1$ (red), $\bar{R}_f = 0.3$ (green), and $\bar{R}_f = 1$ (blue) at $\mathrm{Bi}_c = 1$ (squares), $\mathrm{Bi}_c = 10$ (triangles), $\mathrm{Bi}_c = 100$ (gradients), and $\mathrm{Bi}_c = 1000$ (diamonds). The symbols connected by thin solid curves represent numerical values. The dashed curves are calculated with Eq. (71). The dashed-double-dotted curves are calculated with Eq. (65). The dashed curves, shown only for $\mathrm{Bi}_c = 1$ and $\mathrm{Bi}_c = 10$, visually almost coincide with the corresponding solid curves.

where

$$C^2 = 2\mathrm{Bi}_c \bar{n}_S \left(\frac{1}{\pi} + 2\bar{R}_f\right). \tag{45}$$

The general solution of Eq. (44) satisfying condition $\bar{\tau}_{\theta_1}(0) = 0$ has the form of

$$\bar{\tau}_{\theta_1}(\bar{\eta}) = \bar{\eta} + \tilde{D}\ \sinh\left(\frac{C\bar{\eta}}{\cos\theta_1}\right), \tag{46}$$

where $\tilde{D}$, which does not depend on $\bar{\eta}$ but can depend on θ_1, should be obtained based on another boundary condition formulated for any of the SC ends. In order to simplify the form of this boundary condition, we represent $\tilde{D}$ in the form $\tilde{D} = -D\cos\theta_1$, where $D = D(\theta_1)$ is an unknown function. Then,

$$\bar{\tau}_{\theta_1}(\bar{\eta}) = \bar{\eta} - D\cos\theta_1\ \sinh\left(\frac{C\bar{\eta}}{\cos\theta_1}\right). \tag{47}$$

The boundary condition at $\bar{\eta} = \cos\theta_1/2$ can be found by averaging Eq. (9b),

$$\frac{dT_{f,\theta_1}}{dx_1}\Big|_{x_1 = x_{C_1} + L_f(\cos\theta_1)/2} = \frac{1}{\cos\theta_1}\frac{\sigma_c}{A_f k_f}\frac{\langle N_J\rangle_{(3,4)}}{2}\langle \Delta T_{\theta_1}\rangle_{(3,4)}, \tag{48}$$

where $\langle N_J\rangle_{(3,4)}/2$ is the total number of junctions of types 3 and 4 at a SC end [junctions of types 1 and 2 do not contribute to the right-hand side of Eq. (9b)],

$$\langle N_J\rangle_{(3,4)} = \langle N_J\rangle \frac{A_{\mathrm{ex}(3)} + A_{\mathrm{ex}(4)}}{A_{\mathrm{ex}}} = 4\bar{n}_S\bar{R}_f(1 + \pi\bar{R}_f), \tag{49}$$

and $\langle \Delta T_{\theta_1}\rangle_{(3,4)}$ is the average temperature difference at such junctions. $\langle \Delta T_{\theta_1}\rangle_{(3,4)}$ is derived in Sec. SII in the supplementary material in the form of Eq. (S41) [see also Eq. (B4) in Appendix B],

$$\langle \Delta T_{\theta_1}\rangle_{(3,4)} = \nabla T_x L_f \frac{\cos\theta_1}{2}\frac{K + \pi\bar{R}_f F_{\theta_1}(D)}{1 + \pi\bar{R}_f} - \tau_{\theta_1}\left(\frac{L_f\cos\theta_1}{2}\right), \tag{50}$$

where the functional $F_{\theta_1}(D)$ is given by Eqs. (B5) or (S43) in the supplementary material and

$$K = 1 + (8/\pi + \pi)\bar{R}_f + (16/3)\bar{R}_f^2. \tag{51}$$

After combining Eqs. (47)–(50), the boundary condition reduces to

$$-D\left[C\cosh\left(\frac{C}{2}\right) + A\sinh\left(\frac{C}{2}\right)\right] + 1 + \frac{A}{2} = \mathrm{Bi}_c\bar{n}_S\bar{R}_f K + \pi\mathrm{Bi}_c\bar{n}_S\bar{R}_f^2 F_{\theta_1}(D), \tag{52}$$

where

$$A = 2\mathrm{Bi}_c\bar{n}_S\bar{R}_f(1 + \pi\bar{R}_f). \tag{53}$$

Equation (52) is an integral equation with respect to the unknown function $D = D(\theta_1)$. We did not perform a comprehensive analysis of this equation; however, at least one physically meaningful solution of Eq. (52) can be easily found. The results of numerical simulations show that, for a SC embedded into a dense isotropic network, the temperature gradient ∇T_{fx} averaged over the SC length is independent of θ_1 (Fig. 15). For the temperature distribution given by Eq. (47),

$$\nabla T_{fx} = \int_{-(L_f/2)\cos\theta_1}^{(L_f/2)\cos\theta_1} \frac{dT_{f,\theta_1}}{dx_1}\frac{dx_1}{L_f\cos\theta_1} = \nabla T_x\frac{\bar{\tau}_{\theta_1}((\cos\theta_1)/2)}{(\cos\theta_1)/2} = \nabla T_x(1 - 2D\sinh(C/2)), \tag{54}$$

and ∇T_{fx} does not depend on θ_1 only if D does not depend on θ_1. For constant D, Eq. (B6) reduces to $F_{\theta_1}(D) = (8/\pi^2)(D\sinh(C/2) - (1/2))$ and D can be found from Eq. (52) as

$$D = \frac{1 + A/2 - B}{C\cosh(C/2) + A\sinh(C/2)}, \tag{55}$$

where

$$B = \mathrm{Bi}_c\bar{n}_S\bar{R}_f\frac{K(C + A\ \tanh(C/2)) + (8/\pi)\bar{R}_f(\tanh(C/2) - C/2)}{C + (A + (8/\pi)\mathrm{Bi}_c\bar{n}_S\bar{R}_f^2)\tanh(C/2)}. \tag{56}$$

Equation (47) with parameters A, B, C, D, and K given by Eqs. (53), (56), (45), and (51) describes the distribution of the average temperature along a SC in a dense network. At $\bar{R}_f \ll 1$, the temperature distribution is close to the linear one (Fig. 20) with zero temperature gradient at the SC ends at $\bar{R}_f = 0$, because for slender rods only the junctions of type 1 are possible,

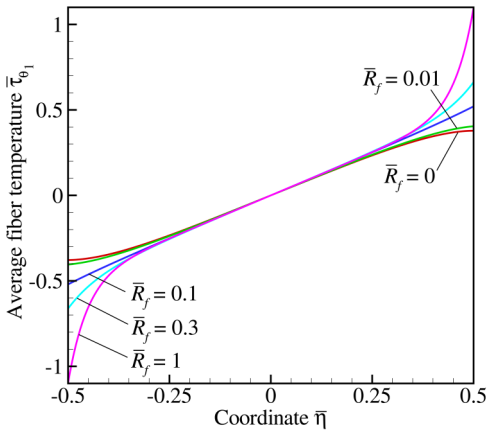

FIG. 20. Distributions of the average fiber temperature $\bar{\tau}_{\theta_1}(\bar{\eta})$ given by Eq. (47) for $\mathrm{Bi}_c\bar{n}_S = 100$, $\cos\theta_1 = 1$, and various $\bar{R}_f$: $\bar{R}_f = 0$ (red), $\bar{R}_f = 0.01$ (green), $\bar{R}_f = 0.1$ (blue), $\bar{R}_f = 0.3$ (cyan), and $\bar{R}_f = 1$ (magenta).

$\langle \Delta T_{\theta_1} \rangle_{(3,4)} = 0$ and, consequently, Eq. (48) requires zero temperature gradient at the SC ends. For moderate and large $\bar{R}_f$, e.g., $\bar{R}_f = 1$, the temperature gradient at the SC ends increases above of the temperature gradient in the sample, ∇T_x, so that the average temperature gradient, ∇T_{fx}, along a SC given by Eq. (54) can also be larger than ∇T_x. In particular, $\nabla T_{fx} \to \nabla T_{fx}^{\infty}$ at $\mathrm{Bi}_c\bar{n}_S \to \infty$, where

$$\nabla T_{fx}^{\infty} = \nabla T_x \frac{K}{1 + (4/\pi + \pi)\bar{R}_f}, \tag{57}$$

(dashed-dotted curve in Fig. 21). On the other hand, the temperature gradient at the center of a SC,

$$\nabla T_{fxC} = \frac{dT_{f,\theta_1}}{dx}\Big|_{x=x_{C_1}} = \nabla T_x(1 - CD), \tag{58}$$

is almost independent of $\bar{R}_f$ and smaller than ∇T_x at any finite $\mathrm{Bi}_c\bar{n}_S$. In addition, $\nabla T_{fxC} \to \nabla T_x$ at $\mathrm{Bi}_c\bar{n}_S \to \infty$ regardless of $\bar{R}_f$.

The average temperature difference at junctions $\langle \Delta\bar{T}_{(+)} \rangle_{\infty}$ can be found based on Eqs. (40) and (47). The approach to evaluation of $\langle \Delta\bar{T}_{(+)} \rangle_{\infty}$ is briefly described in Appendix C. The detailed derivation presented in Sec. SIII in the supplementary material results in Eq. (S56),

$$\langle \Delta\bar{T}_{(+)} \rangle_{\infty} = \frac{\pi}{2} \frac{(1 + 2\pi\bar{R}_f)D_1 + \pi\bar{R}_f K D_2 + 2\bar{R}_f^2(1 + (8\pi/3)\bar{R}_f + \pi^2\bar{R}_f^2)}{(1 + \pi\bar{R}_f)(1 + 4\pi\bar{R}_f + 2\pi^2\bar{R}_f^2)}, \tag{59}$$

where $D_1 = D[C\cosh(C/2) - 2\sinh(C/2)]/C^2$, $D_2 = D\sinh(C/2)$, and the subscript "∞" indicates that this value is obtained for dense networks at $\bar{n}_S \to \infty$. The temperature difference depends only on $\bar{R}_f$ and $\mathrm{Bi}_c\bar{n}_S$. At fixed $\bar{R}_f$, $\mathrm{Bi}_c\bar{n}_S$ is proportional to the Biot number $\mathrm{Bi}_T = \mathrm{Bi}_c\langle N_J \rangle$, which is defined by the average total conductance of all junctions for a single fiber.[59] This observation means that Bi_T serves as a true measure of the effect of the intrinsic conductivity of individual fibers on the effective conductivity of fibrous materials. For dense networks, when $\bar{n}_S$ and $\langle N_J \rangle$ are large, this effect can control the effective conductivity even if the intrinsic fiber conductivity is large and, correspondingly, Bi_c is small.

At $\mathrm{Bi}_c \to 0$, $\langle \Delta\bar{T}_{(+)} \rangle_{\infty}$ approaches $\langle \Delta\bar{T}_{(+)} \rangle_{\infty}^{0}$ given by Eq. (25). At $\mathrm{Bi}_c \to \infty$, $\langle \Delta\bar{T}_{(+)} \rangle_{\infty}$ approaches $\langle \Delta\bar{T}_{(+)} \rangle_{\infty}^{\infty}$ given by the following equation:

$$\langle \Delta\bar{T}_{(+)} \rangle_{\infty}^{\infty} = \frac{\pi}{2}\bar{R}_f^3 \frac{8\pi/3 - 8/\pi + [(8\pi^2 - 32)/3 + 2\pi^2]\bar{R}_f + \pi(2\pi^2 - 56/9)\bar{R}_f^2}{(1 + \pi\bar{R}_f)(1 + 4\pi\bar{R}_f + 2\pi^2\bar{R}_f^2)(1 + (4/\pi + \pi)\bar{R}_f)}, \tag{60}$$

(dashed curve in Fig. 21). At finite Bi_c, $\langle \Delta\bar{T}_{(+)} \rangle_{\infty}$ is in between $\langle \Delta\bar{T}_{(+)} \rangle_{\infty}^{0}$ and $\langle \Delta\bar{T}_{(+)} \rangle_{\infty}^{\infty}$.

Equation (59) predicts a complex dependence of $\langle \Delta\bar{T}_{(+)} \rangle_{\infty}$ on $\mathrm{Bi}_c\bar{n}_S$ at finite $\bar{R}_f$ (Fig. 20). For slender rods, Eq. (59) reduces to

$$\langle \Delta\bar{T}_{(+)} \rangle_{\infty} = \frac{\pi/8}{\mathrm{Bi}_c\bar{n}_S/(2\pi)} \left(1 - \frac{\tanh\left(\sqrt{\mathrm{Bi}_c\bar{n}_S/(2\pi)}\right)}{\sqrt{\mathrm{Bi}_c\bar{n}_S/(2\pi)}} \right). \tag{61}$$

As shown in Sec. SIV in the supplementary material, this equation can be approximated by Eq. (S69) obtained based on a hypothesis of linear temperature distribution along a SC. In the high-density approximation, Eq. (S69) in the supplementary material reduces to

$$\langle \Delta\bar{T}_{(+)} \rangle_{\infty} = \frac{\pi/8}{3 + \mathrm{Bi}_c\bar{n}_S/(2\pi)}. \tag{62}$$

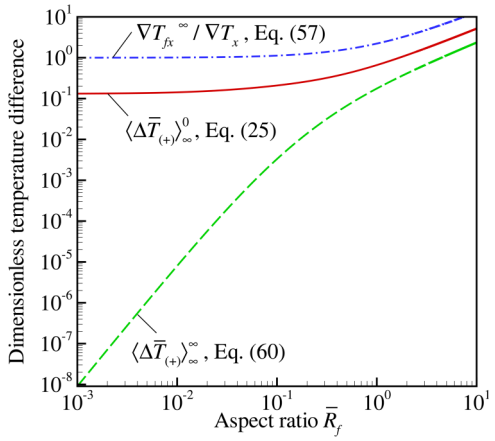

FIG. 21. Average temperature differences $\langle \Delta\bar{T}_{(+)} \rangle_{\infty}^{0}$ [red solid curve, Eq. (25) for $\mathrm{Bi}_c = 0$] and $\langle \Delta\bar{T}_{(+)} \rangle_{\infty}^{\infty}$ [green dashed curve, Eq. (60) for $\mathrm{Bi}_c \to \infty$], as well as average gradient of fiber temperature $\nabla T_{fx}^{\infty}/\nabla T_x$ [blue dashed-dotted curve, Eq. (57) for $\mathrm{Bi}_c \to \infty$] vs aspect ratio $\bar{R}_f$.

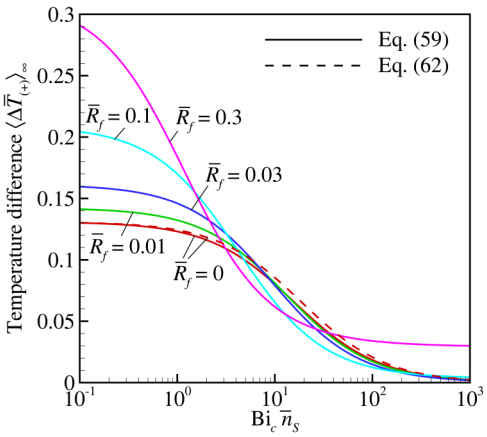

FIG. 22. Average temperature difference $\langle \Delta \bar{T}_{(+)} \rangle_\infty$ vs $\mathrm{Bi}_c \bar{n}_S$. The solid curves are obtained with Eq. (59) for $\bar{R}_f = 0$ (red), $\bar{R}_f = 0.01$ (green), $\bar{R}_f = 0.03$ (blue), $\bar{R}_f = 0.1$ (cyan), and $\bar{R}_f = 0.3$ (magenta). The red dashed curve for $\bar{R}_f = 0$ is obtained based on the approximation given by Eq. (62).

The good match between the predictions of Eqs. (61) and (62), shown by the solid and dashed curves in Fig. 22, proves that Eq. (62) provides good approximation of $\langle \Delta \bar{T}_{(+)} \rangle_\infty$ for slender rods.

The comparison of numerical values of $\langle \Delta \bar{T}_{(+)} \rangle$ with predictions of Eq. (59), plotted in Figs. 23 and 24 as solid and dashed curves, respectively, shows a good agreement between the two at $\bar{n}_S > 50$. At $\bar{R}_f = 0$, the numerically calculated temperature differences approach zero at $\bar{n}_S \to \infty$, while at $\bar{R}_f > 0$ they approach nonzero asymptotic values that are in perfect agreement with predictions of Eq. (60). These asymptotic values, however, are small for high-aspect-ratio SCs.

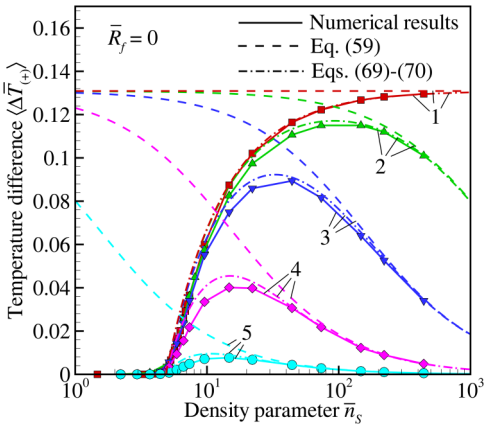

FIG. 23. Average temperature difference $\langle \Delta \bar{T}_{(+)} \rangle$ vs density parameter $\bar{n}_S$ at $\bar{R}_f = 0$ for $\mathrm{Bi}_c = 0$ (red squares and curves 1), $\mathrm{Bi}_c = 0.01$ (green triangles and curves 2), $\mathrm{Bi}_c = 0.1$ (blue gradients and curves 3), $\mathrm{Bi}_c = 1$ (magenta diamonds and curves 4), and $\mathrm{Bi}_c = 10$ (cyan circles and curves 5). The symbols and solid curves represent numerical values. The dashed and dashed-dotted curves are calculated with Eqs. (59), (69), and (70), respectively.

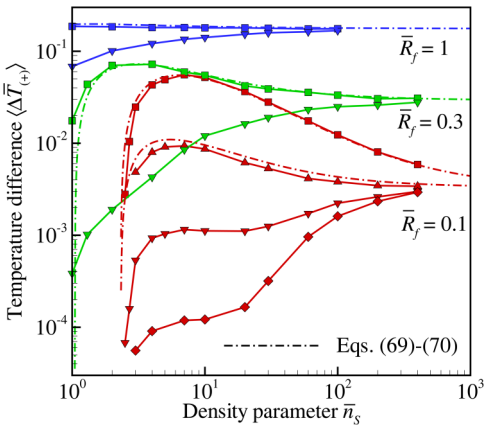

FIG. 24. Average temperature difference $\langle \Delta \bar{T}_{(+)} \rangle$ vs density parameter $\bar{n}_S$ for $\bar{R}_f = 0.1$ (red), $\bar{R}_f = 0.3$ (green), and $\bar{R}_f = 1$ (blue) at $\mathrm{Bi}_c = 1$ (squares), $\mathrm{Bi}_c = 0.10$ (triangles), $\mathrm{Bi}_c = 100$ (gradients), and $\mathrm{Bi}_c = 1000$ (diamonds). The symbols with solid curves represent numerical values. The dashed-dotted curves are calculated with Eqs. (69) and (70).

Depending on Bi_c and $\bar{R}_f$, the numerical profiles of $\langle \Delta \bar{T}_{(+)} \rangle$ as functions of $\bar{n}_S$ can be monotonous or exhibit a maximum. The presence of a maximum is characteristic for high-aspect-ratio fiber networks at an arbitrary Bi_c, as well as for short-aspect-ratio fiber networks at small Bi_c. At small $\bar{R}_f$, $\langle \Delta \bar{T}_{(+)} \rangle$ first rises when $\bar{n}_S$ increases from below the percolation threshold and then achieves its maximum as a result of the reduction in the correlation of SC temperatures. For small $\bar{R}_f$ and large $\mathrm{Bi}_c \bar{n}_S$, Eqs. (54) and (58) predict that both ∇T_{fx} and ∇T_{fxC} are close to ∇T_x and, hence, the temperature distribution in a SC along the coordinate x is close to the distribution of the average temperature $T(x)$ in the sample. With further increase in $\bar{n}_S$, $\langle \Delta \bar{T}_{(+)} \rangle$ starts to drop, because the temperatures of SCs with junctions at points with the same coordinate x almost coincide with each other and with the average temperature $T(x)$ of the sample. For short SCs at large Bi_c, the profiles of $\langle \Delta \bar{T}_{(+)} \rangle$ as functions of $\bar{n}_S$ become monotonous because the asymptotic temperature difference is relatively high.

After inserting Eqs. (59), (19), and (22) into the right-hand side of Eq. (17), one can express the conductivity at finite Bi_c as

$$k = \sigma_c C_0(\bar{R}_f, \mathrm{Bi}_c \bar{n}_S) \bar{n}_S^2, \tag{63}$$

where

$$C_0(\bar{R}_f, \mathrm{Bi}_c \bar{n}_S) = C_0^0(\bar{R}_f) \frac{\langle \Delta \overline{T}_{(+)} \rangle_\infty}{\langle \Delta \overline{T}_{(+)} \rangle_\infty^0}. \tag{64}$$

According to Eqs. (59) and (63), the effect of the intrinsic conductivity of SCs on the average temperature difference $\langle \Delta \bar{T}_{(+)} \rangle$ and bulk conductivity is not defined solely by Bi_c but depends on $\mathrm{Bi}_c \bar{n}_S \sim \mathrm{Bi}_c \langle N_J \rangle = \mathrm{Bi}_T$ and, thus, on the average total conductance at all junctions of a SC.[59] This effect can be significant even at

small Bi_c if the material density and, correspondingly, the density of contacts between fibers are large.

At $\bar{R}_f > 0$, in the limit $\mathrm{Bi}_c \to \infty$, Eq. (63) reduces to

$$k_\infty^\infty = \sigma_c C_0^\infty(\bar{R}_f)\bar{n}_S^2, \tag{65}$$

where

$$C_0^\infty(\bar{R}_f) = C_0^0(\bar{R}_f)\frac{\langle\Delta\overline{T}_{(+)}\rangle_\infty^\infty}{\langle\Delta\overline{T}_{(+)}\rangle_\infty^0}, \tag{66}$$

and $\langle\Delta\overline{T}_{(+)}\rangle_\infty^\infty$ is given by Eq. (60). Thus, in the limit of a large Biot number, the obtained solution predicts quadratic scaling of conductivity with the density parameter for systems composed of SCs of finite radius. This result is in agreement with numerical calculations that also predict a quadratic scaling law $\bar{k} \propto \bar{n}_S^2$ at $\bar{n}_S \gg 1$ and $\bar{R}_f > 0$ (Fig. 17). Equation (65), however, cannot be used at $\bar{R}_f = 0$.

For slender rods, Eq. (63) reduces to

$$k = \frac{\sigma_c \bar{n}_S}{2\mathrm{Bi}_c}\left(1 - \frac{\tanh\left(\sqrt{\mathrm{Bi}_c\bar{n}_S/(2\pi)}\right)}{\sqrt{\mathrm{Bi}_c\bar{n}_S/(2\pi)}}\right). \tag{67}$$

Then, at $\mathrm{Bi}_c \to \infty$,

$$k \to k_\infty^\infty = \frac{1}{2}\sigma_f\bar{n}_S = \frac{k_f A_f}{2}\frac{\rho_S}{\rho_f}, \tag{68a}$$

or

$$\frac{k}{\sigma_f} \to \overline{\overline{k}}_\infty^\infty = \bar{k}_\infty^\infty\mathrm{Bi}_c = \frac{\bar{n}_S}{2}, \tag{68b}$$

where the subscript and superscript "∞" indicate that these equations are valid at $\mathrm{Bi}_c \to \infty$ and $\bar{n}_S \to \infty$. Equation (68) describes the conductivity of an "ordinary" fibrous material, where the contact resistance is negligibly small. The dimensional conductivity k in this case is a linear function of the surface density ρ_S and is independent of the fiber length. This equation is in agreement with the scaling law $\overline{\overline{k}} \propto \bar{n}_S$ at $\bar{n}_S \gg 1$ revealed for slender rods in the numerical calculations of conductivity [Fig. 16(b)].

For disk particles, i.e., at $L_f \to 0$, Eq. (63) reduces to Eq. (30), which was previously obtained for disks at $\mathrm{Bi}_c = 0$, and, thus, the effects of intrinsic thermal conductivity vanish in the limit of disk particles. In our model, it occurs since $\mathrm{Bi}_c\bar{n}_S = \sigma_c n_S L_f^3/(k_f A_f) \to 0$ as $L_f \to 0$ and the redistribution of thermal energy due to heat conduction is considered only along the "cylindrical" parts of SCs.

In spite of similarity between conductivity curves shown in Figs. 16(a) and 18 for $\bar{R}_f = 0$ and $\bar{R}_f = 0.01$, the asymptotic behavior of curves plotted for finite Bi_c in these two cases is different. At $\bar{R}_f = 0$, the curves follow the linear scaling law, $\overline{\overline{k}} \propto \bar{n}_S$, while at $\bar{R}_f = 0.01$, the curves follow the quadratic scaling law, $\bar{k} \propto \bar{n}_S^2$, as $\bar{n}_S \to \infty$. At a large Biot number, the latter is realized at $\bar{n}_S \gg 10^3$ and is not seen in Fig. 18. At the same time, at $\bar{R}_f = 0.01$, the curves corresponding to large Biot numbers can have a "transient" range of $\bar{n}_S$ where $\bar{k}(\bar{n}_S)$ can be fitted by a linear function. The examples of such linear fits are shown by solid lines in Fig. 18. At large $\bar{R}_f$, e.g., $\bar{R}_f \geq 0.1$, the numerically calculated values of conductivity for moderate $\bar{n}_S$ can be substantially smaller than the values predicted by Eq. (65) at $\mathrm{Bi}_c \to \infty$ (Fig. 18). This effect cannot be captured by the developed theoretical conductivity equations.

The derivation of Eq. (59) reveals the reasons for the difference in the asymptotic behavior of conductivity at finite Bi_c between slender rods and SCs with $\bar{R}_f > 0$. For slender rods, where only junctions of type 1 are present, the distribution of average temperature along a SC is close to a linear one, and the temperature difference at the junctions drops to zero at $\mathrm{Bi}_c \to \infty$. At $\bar{R}_f > 0$, the temperature difference at junctions does not drop to zero because, for junctions of types 2, 3, and 4, points J_1 and J_2 on the SC axes have different x coordinates (Fig. 8). This peculiarity is a result of the assumption that semicircular SC caps have infinite conductivity, so that the effect of finite contact conductivity does not vanish at $\mathrm{Bi}_c \to \infty$. Presumably, the finite values of $\langle\Delta\bar{T}_{(+)}\rangle$ at $\mathrm{Bi}_c \to \infty$ could be avoided if the definition of the junction geometry would be changed to ensure that $x_{J_1} = x_{J_2}$ for junctions of any type. The origin of the problem with the conductivity of thick SCs at large Bi_c is the assumption that the temperature distribution within a SC is always one-dimensional, while this is not the case for thick SCs.

B. Conductivity equation in semidilute networks

To obtain a good approximation for $\langle\Delta\bar{T}_{(+)}\rangle$ in semidilute networks, one needs to account for the correlations between SC temperatures at the junctions. The average temperature difference in a semidilute network can be expressed as

$$\langle\Delta\bar{T}_{(+)}\rangle = \langle\Delta\overline{T}_{(+)}\rangle_\infty + \langle\delta\Delta\bar{T}_{(+)}\rangle, \tag{69}$$

where $\langle\delta\Delta\bar{T}_{(+)}\rangle$ is, in general, a function of $\bar{n}_S$, Bi_c, and $\bar{R}_f$. Because the percolation threshold is independent of Bi_c, a simple approximation of $\langle\delta\Delta\bar{T}_{(+)}\rangle$ can be found from the requirement that Eqs. (34) and (69) give zero value at the same value of the density parameter at a fixed $\bar{R}_f$. This condition ensures that the conductivity of networks with arbitrary Bi_c and fixed $\bar{R}_f$ is turned into zero at the same $\bar{n}_S$. Then,

$$\langle\delta\Delta\bar{T}_{(+)}\rangle = \frac{\langle\Delta\overline{T}_{(+)}\rangle_\infty}{\langle\Delta\overline{T}_{(+)}\rangle_\infty^0}\langle\delta\Delta\bar{T}_{(+)}\rangle^0, \tag{70}$$

where $\langle\delta\Delta\bar{T}_{(+)}\rangle^0$ is given by Eq. (33). For slender rods, this correction reduces the maximum discrepancy between numerical values of $\langle\Delta\bar{T}_{(+)}\rangle$ and predictions based on Eq. (69) at $\bar{n}_S \geq 10$ below 25% at $\mathrm{Bi}_c = 1$ and below 6% at $\mathrm{Bi}_c = 0.1$ (Fig. 23). For finite $\bar{R}_f$, Eq. (70) provides good approximation for $\langle\Delta\bar{T}_{(+)}\rangle$ in semidilute networks at $\mathrm{Bi}_c \leq 10$ (Fig. 24). For slender rods, Eq. (S69) derived in the supplementary material enables calculations of $\langle\Delta\bar{T}_{(+)}\rangle$ in semidilute networks with almost the same degree of accuracy as Eq. (70).

After inserting Eqs. (69), (19), and (22) into the right-hand side of Eq. (17), one can find the conductivity at finite Bi_c in the following form:

$$k = \sigma_c C_0(\bar{R}_f, \mathrm{Bi}_c\bar{n}_S)\bar{n}_S^2 - \sigma_c C_1(\bar{R}_f, \mathrm{Bi}_c\bar{n}_S)\bar{n}_S, \tag{71}$$

where

$$C_k(\bar{R}_f, \mathrm{Bi}_c\bar{n}_S) = C_k^0(\bar{R}_f)\frac{\langle\Delta\overline{T}_{(+)}\rangle_\infty}{\langle\Delta\overline{T}_{(+)}\rangle_\infty^0}, \quad k = 0, 1. \tag{72}$$

All conductivity equations derived above can be obtained as asymptotic limits of the most general Eq. (71). The relationship between various equations obtained in the present study is illustrated in Fig. 25. At $\bar{R}_f \ll 0.1$, Eq. (71) provides a good approximation of the numerical results for the conductivity of slender rods at arbitrary $\bar{n}_S$ and Bi_c (dashed curves in Figs. 16 and 18). For $\bar{R}_f \geq 0.1$, Eq. (71) ensures good approximation of the numerical data at large $\bar{n}_S$. At moderate $\bar{n}_S \sim 10 - 100$, Eq. (71) is accurate only when the numerical values of conductivity are close to or larger than k_∞^∞ given by Eq. (65), i.e., when the curves corresponding to different Bi_c in Fig. 19 are close to or above the dashed-double-dotted curves corresponding to the limit of $\mathrm{Bi}_c \to \infty$.

In Sec. SIV in the supplementary material, we derived approximate Eq. (S70) for conductivity of semidilute networks of slender rods:

$$k = \frac{\sigma_c}{12\pi + 2\mathrm{Bi}_c\bar{n}_S}\left(\bar{n}_S^2 - \frac{48}{\pi^2}\bar{n}_S\right). \tag{73}$$

This equation provides almost the same degree of accuracy as Eq. (71) with respect to the results of Monte Carlo calculations.

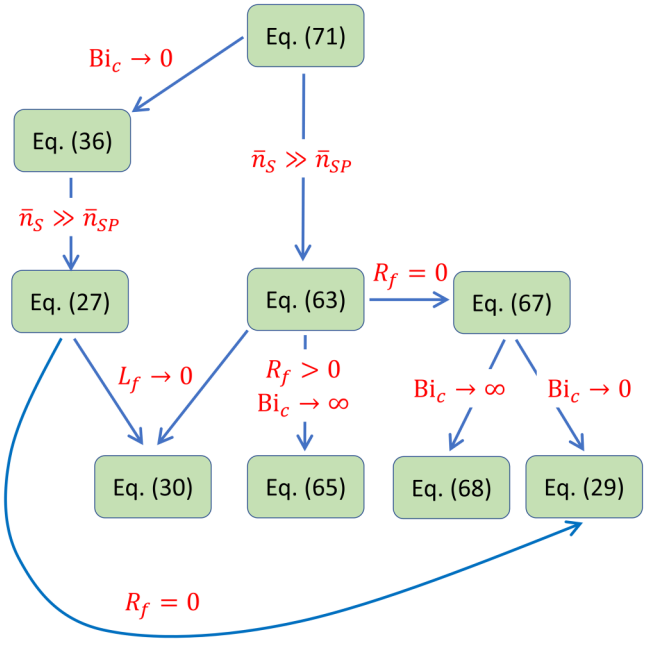

FIG. 25. Sketch illustrating the relationships between various theoretical conductivity equations obtained in this work. Equation (71) is the most general equation. Other equations can be considered as asymptotic limits of Eq. (71) under certain conditions. These conditions are given at arrows depicting directions of transformation of more general equations into less general ones.

The analog of Eq. (73) in the high-density approximation, when the second term in the right-hand part can be omitted, was derived in Ref. 59. Similar equations were proposed on a semiempirical basis in Refs. 55 and 57.

IX. DOMAINS OF APPLICABILITY OF THEORETICAL CONDUCTIVITY EQUATIONS AND REGIMES OF HEAT TRANSFER

The domains of applicability of the theoretical equations and scaling laws derived above are roughly defined by the approximations used in the theoretical analysis. In this section, we report the results of quantitative evaluation of the domains of applicability of major theoretical equations, such as Eqs. (36) and (71), and the two major scaling laws, quadratic $\bar{k} \propto \bar{n}_S^2$ and linear $\bar{k} \propto \bar{n}_S$, in the space of material parameters that fully characterize a 2D system of straight conducting fibers, $\bar{n}_S$, $\bar{R}_f$, and Bi_c. The quantitative evaluation is based on a large number (several hundreds) of Monte Carlo calculations of thermal conductivity performed with a model described in Sec. III. The difference between numerically calculated and theoretically predicted values of thermal conductivity is characterized by the relative error $\varepsilon = 100\% \times |\bar{k}_{th} - \bar{k}|/\bar{k}$, where $\bar{k}$ is the conductivity obtained in Monte Carlo calculations and $\bar{k}_{th}$ is the corresponding value predicted by one of the theoretical equations. For $\mathrm{Bi}_c = 0$, the numerical calculations are performed at $1 \leq \bar{n}_S \leq 10^3$ and $10^{-3} \leq \bar{R}_f \leq 10^{-1}$ (Fig. 26). For $\mathrm{Bi}_c \neq 0$, the calculations are performed at $1 \leq \bar{n}_S \leq 10^3$ and $10^{-2} \leq \mathrm{Bi}_c \leq 10^2$ for $\bar{R}_f = 0$, 0.01, 0.1, and 1 (Fig. 27).

For systems composed of fibers with infinite thermal conductivity ($\mathrm{Bi}_c = 0$), the domain where the relative error of Eq. (36) is smaller than 10% corresponds to the patterned area

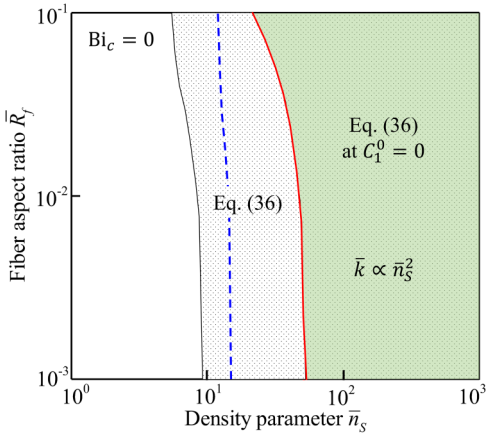

FIG. 26. Domains of applicability of Eq. (36) for thermal conductivity of fibrous materials in the parameter space $(\bar{n}_S, \bar{R}_f)$ at $\mathrm{Bi}_c = 0$. The error of Eq. (36) with respect to the direct numerical calculations of $\bar{k}$ is less than 10% in the domain shaded by the gray pattern. The error of Eq. (36) with respect to the direct numerical calculations of $\bar{k}$ is less than 1% to the right of the blue dashed curve. The error of Eq. (36) with $C_1^0 = 0$, when the predicted value of conductivity follows the quadratic scaling law $\bar{k} \propto n_S^2$, is less than 10% in the domain filled with green color to the right of the red curve.

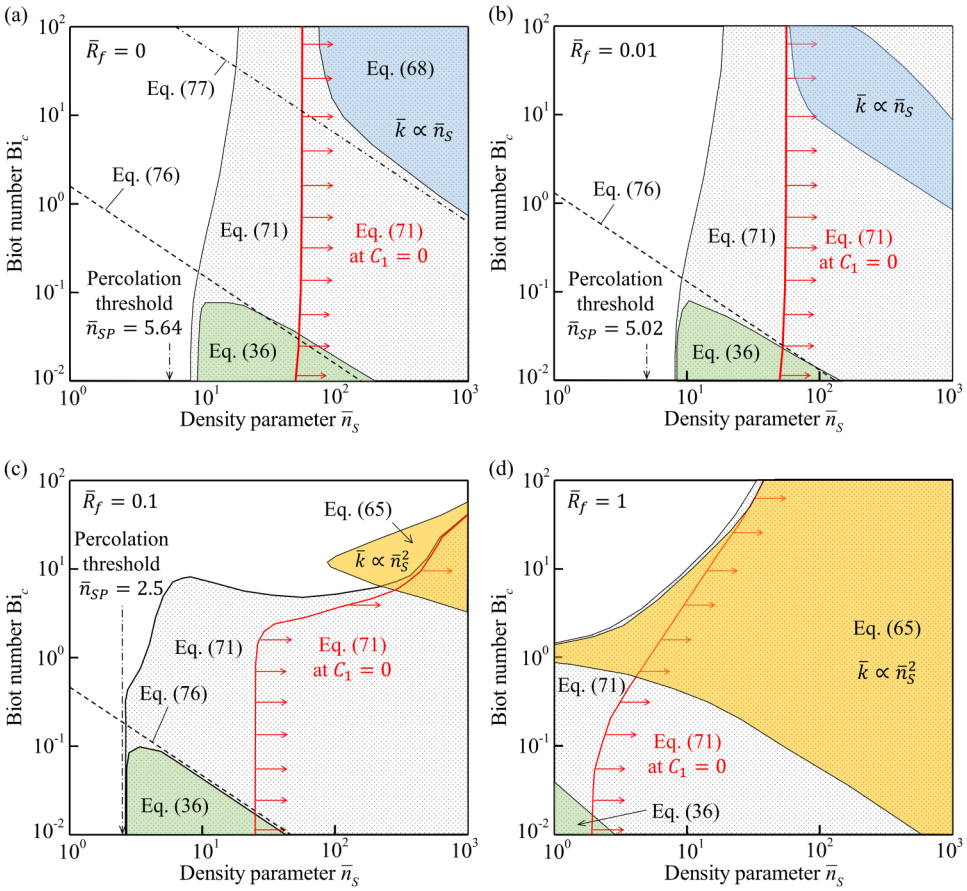

FIG. 27. Domains of applicability of Eqs. (36) and (71) for thermal conductivity in the parameter space ($\bar{n}_S$, Bi_c) at $\bar{R}_f = 0$ (a), $\bar{R}_f = 0.01$ (b), $\bar{R}_f = 0.1$ (c), and $\bar{R}_f = 1$ (d). The error of Eq. (71) with respect to the direct numerical calculations of $\bar{k}$ is less than 10% in the domains shaded by the gray pattern. The error of Eq. (71) with $C_1 = 0$, when the correction for finite density parameter is not accounted for, is less than 10% to the right of thick red curves with arrows. The error of Eq. (36), which is obtained for the case of $\mathrm{Bi}_c = 0$, is less than 10% in the domains filled by green. The dashed lines illustrate the analytical approximation of the upper boundary of these domains provided by Eq. (76) at $\delta = 0.1$. In panel (a), in the domain colored blue, the error of Eq. (68) is less than 10% and the conductivity follows the linear scaling law, $\bar{k} \propto \bar{n}_S$. The dashed-dotted line shows the analytical approximation of the lower boundary of this domain provided by Eq. (77) at $\delta = 0.1$. In the blue domain shown in panel (b), the numerically calculated values of conductivity can be reasonably well fitted, at a fixed Bi_c, by a linear function of the density parameter and $\bar{k} \propto \bar{n}_S$. In panels (c) and (d), in the domains colored yellow, the error of Eq. (65) is less than 10% and the conductivity follows to the quadratic scaling law, $\bar{k} \propto \bar{n}_S^2$.

in Fig. 26. The boundary of this domain shifts toward smaller $\bar{n}_S$ with increasing $\bar{R}_f$ due to the reduction of the percolation threshold $\bar{n}_{SP}$ with increasing $\bar{R}_f$. In the part of the patterned area to the right of the blue dashed curve, the error of the theoretically predicted values is smaller than 1%. The area colored by green corresponds to the domain where the error of Eq. (36) with $C_1^0 = 0$, i.e., without the correction for finite values of $\bar{n}_S$, is less than 10%. In this domain, both numerically calculated and theoretically predicted values of thermal conductivity follow the quadratic scaling law, $\bar{k} \propto \bar{n}_S^2$. To the left of the green-colored domain, the system is gradually approaching the percolation threshold and, as a result, the thermal conductivity exhibits a superquadratic scaling with surface density.

The domain in the parameter space where Eq. (36) obtained for $\mathrm{Bi}_c = 0$ can be used is also identified in the simulations performed with finite values of the Biot number. Four cross sections of this domain, where the error of Eq. (36) is less than 10%, are colored green in Fig. 27. For the range of Bi_c considered in the calculations, these green regions correspond to relatively small $\bar{n}_S <\sim 10^2$, when a deviation from the high-density limit starts to be important. As a result, the parts of the domain where thermal conductivity follows Eq. (36) with $C_1^0 = 0$ are outside the range of parameters used in the calculations and shown in Fig. 27. With Bi_c decreasing below 10^{-2}, the green regions would expand to larger $\bar{n}_S$, and the parts of the domain where Eq. (36) is valid with $C_1^0 = 0$ would appear.

The range of Bi_c, where Eq. (36) is valid for a given $\bar{n}_S$ and, thus, the effects of finite Bi_c are negligible, can be theoretically estimated based on the comparison of conductivity values given by Eqs. (27) and (71) or, alternatively, by comparing the values of temperature difference given by Eqs. (25) and (59). In the Taylor series of the right-hand side of Eq. (59) with respect to Bi_c $\bar{n}_S$,

$$\langle \Delta\overline{T}_{(+)} \rangle_\infty = \langle \Delta\overline{T}_{(+)} \rangle_\infty^0 + \Lambda\ \mathrm{Bi}_c\ \bar{n}_S + \cdots, \tag{74}$$

where

$$\Lambda = \left. \frac{d\langle \Delta\overline{T}_{(+)} \rangle_\infty}{d(\mathrm{Bi}_c\ \bar{n}_S)} \right|_{\mathrm{Bi}_c\ \ \bar{n}_S = 0}, \tag{75}$$

the first term $\langle \Delta\overline{T}_{(+)} \rangle_\infty^0$ is given by Eq. (25). By neglecting higher-order terms in the right-hand side of Eq. (74), a curve that corresponds to the relative error $|\langle \Delta\overline{T}_{(+)} \rangle_\infty - \langle \Delta\overline{T}_{(+)} \rangle_\infty^0| / \langle \Delta\overline{T}_{(+)} \rangle_\infty$ equal

to δ can be obtained from the following equation:

$$\frac{|\Lambda|}{\langle \Delta \overline{T}_{(+)} \rangle_{\infty}^{0}} \mathrm{Bi}_c \bar{n}_S = \delta. \tag{76}$$

For slender rods, $\Lambda = -1/120$, as can be established through differentiation of Eq. (61). For an arbitrary $\bar{R}_f$, the differentiation of Eq. (59) results in a complex equation for Λ, which is not provided here. We obtained this equation using symbolic computations in MATLAB®, with the MATLAB code provided in Sec. SV in the supplementary material. The relationship between Bi_c and $\bar{n}_S$ corresponding to Eq. (76) for $\delta = 0.1$ is shown by the dashed line in Fig. 27. As one can see, at $\bar{R}_f \leq 0.1$, Eq. (76) provides a reliable estimate for the boundary of a domain, where the effects of finite Biot number are negligible and Eq. (36) can be used for calculation of conductivity.

The domains where the relative error of Eq. (71) at $\mathrm{Bi}_c \neq 0$ is smaller than 10% correspond to the patterned areas in Fig. 27. At $\bar{R}_f \leq 0.01$, this equation can be used at $\bar{n}_S > 10$ for any Bi_c. If Eq. (71) is used with $C_1 = 0$, i.e., without corrections for finite $\bar{n}_S$, then its error is less than 10% in the domains to the right of thick red curves with arrows.

For slender rods, the blue area in Fig. 27(a) marks the domain where the error of Eq. (68) is less than 10% and the conductivity closely follows the linear scaling law $\bar{k} \propto \bar{n}_S$. The boundary of this domain that corresponds to a given relative error δ can be found theoretically from the equation $|k - k_{\infty}^{\infty}|/k_{\infty}^{\infty} = \delta$, where k and k_{∞}^{∞} are given by Eqs. (67) and (68a), respectively. This equation reduces to

$$\mathrm{Bi}_c \bar{n}_S = 2\pi X^2(\delta), \tag{77}$$

where $X(\delta)$ is the positive root of the equation $\tanh X = \delta X$. For $\delta = 0.1$, $X \approx 10$. Equation (77) is shown by the dashed-dotted curve in Fig. 27(a).

At finite but small $\bar{R}_f$, e.g., $\bar{R}_f = 0.01$ [Fig. 27(b)], the pattern of domains in the parameter space is close to the pattern for slender rods. The asymptotic scaling law at $\bar{n}_S \to \infty$, however, changes from linear for $\bar{R}_f = 0$ to quadratic for $\bar{R}_f > 0$. Correspondingly, the blue region, where the conductivity is described by Eq. (68), does not exist in the parameter space shown in Fig. 27(b). At the same time, the results shown in Fig. 18 suggest that, at a sufficiently large Bi_c, the conductivity can follow a close-to-linear dependence on $\bar{n}_S$ in some limited range of $\bar{n}_S$. The domain corresponding to such a "transient" linear scaling regime is colored blue in Fig. 27(b). The domain where $\bar{k} \propto \bar{n}_S^2$ is out of range of parameters depicted in Fig. 27(b).

At larger $\bar{R}_f$, e.g., $\bar{R}_f = 0.1$ and $\bar{R}_f = 1$ [Figs. 27(c) and 27(d)], the domain where the conductivity can be fitted by a linear function disappears. At the same time, regions where the conductivity follows the asymptotic scaling law $\bar{k} \propto \bar{n}_S^2$ given by Eq. (65) expand toward smaller $\bar{n}_S$. These domains are colored yellow in Figs. 27(c) and 27(d). The distinct feature of systems with relatively large $\bar{R}_f$ is that the numerically calculated values of conductivity at large Bi_c can be smaller than those predicted by theoretical Eq. (65) in the limit $\mathrm{Bi}_c \to \infty$ (Fig. 19). This fact explains, in particular, why the shaded area in Fig. 27(c) does not extend to Bi_c larger than ~100 in the considered range of $\bar{n}_S$ and why the results of numerical calculations can be better described by the approximate Eq. (65) than the formally more accurate Eq. (71) within certain ranges of $\bar{n}_S$ and Bi_c.

X. MAPPING THEORETICAL EQUATIONS TO A REAL MATERIAL SYSTEM

The application of the theoretical results obtained in this paper to a particular material system requires mapping of the properties and structural characteristics of the material of interest to the parameters used in the theoretical analysis of thermal conductivity, i.e., $\bar{n}_S$, $\bar{R}_f$, and Bi_c. To provide an example of such mapping and to illustrate the relevance of the general analysis of thermal conductivity established in Fig. 27 for a particular material system, we consider the regimes of conductivity in thin CNT films. We limit our consideration by films composed of (10,10) single-walled CNTs with the radius $R_f = 6.785$ Å,[84] which are abundant in samples produced by laser ablation of carbon targets.[8,9,85,86] We assume that the CNTs are sufficiently long, so that the effects caused by finite $\bar{R}_f$ are negligible. The cross-sectional area of a single-walled CNT is often defined as an area of a ring with an internal radius of R_f and a thickness of $\delta_f = 3.4$ Å,[39] which gives $A_f = 2\pi R_f \delta_f = 145$ Å^2 for (10,10) single-walled CNTs [note that the definition of A_f adopted for CNTs is slightly different from the one discussed for tubes in Sec. II]. The linear density of the CNT is equal to $\rho_f = 2\pi m R_f n_\sigma = 0.324 \times 10^{-15}$ mg μm^{-1}, where $n_\sigma = 4/\left(3\sqrt{3}l_c^2\right) = 0.381$ Å^2 is the surface density of atoms in a single-walled CNT, $m = 12$ Da is the mass of a carbon atom, and $l_c = 1.421$ Å is the graphene lattice constant.[84,87] The intrinsic conductivity of (10,10) CNTs, k_f, is within the range of 1000−3000 W m^{-1} K^{-1} and the intertube thermal contact conductance, σ_c, is within the range of 10^{-11}−10^{-10} W K^{-1}.[29,35,39,40,42,72] For our calculations, we choose the conservative estimate of k_f equal to 1000 W m^{-1} K^{-1} and $\sigma_c = 5 \times 10^{-11}$ W K^{-1} obtained in Ref. 35.

We characterize the surface density of a CNT film with the surface coverage $\varphi_S = 2R_f L_f n_S$, which can also be expressed through the surface density of the film material ρ_S as $\varphi_S = 2R_f(\rho_S/\rho_f)$. The contours of constant $\bar{n}_S$ and Bi_c in the parameter space (L_f, φ_S) are shown in Fig. 28(a). As one can see, typical nanotube materials are characterized by small Biot numbers for a single contact and relatively large density parameters. The Biot number for the whole nanotube, $\mathrm{Bi}_T = \mathrm{Bi}_c \langle N_J \rangle \sim \mathrm{Bi}_c \bar{n}_S$, however, is not small, and, in a broad range of material parameters, the effect of the intrinsic conductivity cannot be neglected. To make this conclusion apparent, we divided the parameter space in Fig. 28(a), into three domains separated by solid curves that correspond to solutions of Eqs. (76) and (77) at $\delta = 0.1$. In the green domain, the effects of finite Bi_c are negligible and Eq. (36) is valid with the exception of conditions close to the percolation threshold (the isoline $\bar{n}_S = 5.64$ corresponding to percolation threshold for slender rods reduces to equation $\varphi_S L_f = 7.66$ nm and is closer to the axes $\varphi_S = 0$ and $L_f = 0$ than the isoline $\bar{n}_S = 10$ shown in Fig. 28(a)). In the blue domain, the conductivity follows linear scaling with the material density and can be determined with Eq. (68). In the red transitional domain, the effects of finite intrinsic conductivity are strong, but the material conductivity does not approach yet the asymptotic behavior predicted by Eq. (68). In the red domain, which covers most of the practically relevant material

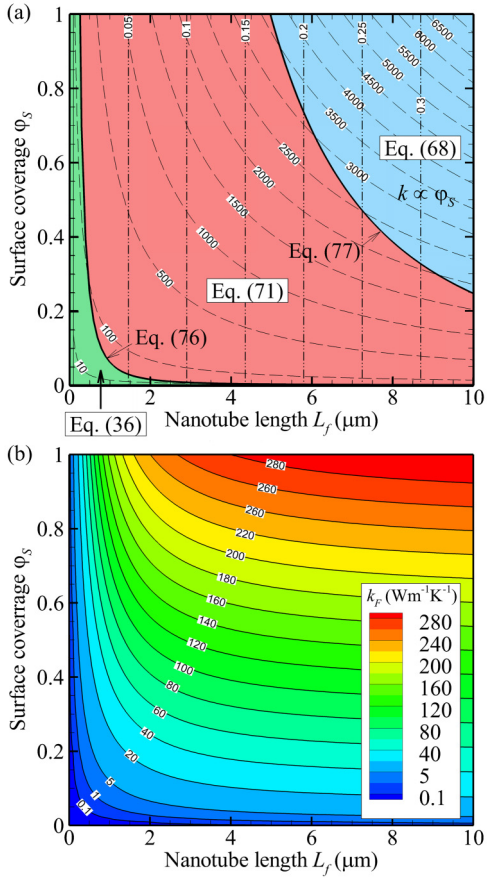

FIG. 28. (a) Chart that defines the density parameter $\bar{n}_S$ (dashed curves) and Biot number for a single contact Bi_c (dashed-double-dotted vertical lines) as functions of the nanotube length L_f and surface coverage φ_S obtained for high-aspect-ratio (10,10) CNTs. The values of $\bar{n}_S$ and Bi_c for every isoline are given in the figure panel. The thick solid curves are obtained with Eqs. (76) and (77). These lines divide the parameter space (L_f, φ_S) into three characteristic domains. In the green domain, the effects of finite Bi_c are negligible and Eq. (36) is valid except for the conditions close to the percolation threshold. In the blue domain, the conductivity follows linear scaling with the material density and can be determined with Eq. (68). In the red transitional domain, the effects of finite intrinsic conductivity are strong, but the conductivity does not yet follow the asymptotic behavior predicted by Eq. (68). In the red domain, the conductivity can be calculated with Eq. (71). (b) Thermal conductivity $k_F = k/\Delta z$ of (10,10) CNT films in units of W m^{-1} K^{-1} as a function of L_f and φ_S. Here, k is calculated based on Eq. (71) at $\bar{R}_f = 0$ and $\Delta z = 2R_f + 3.114$ Å.[56]

parameters, the conductivity can be calculated with Eq. (71). The conclusion about the strong effect of the intrinsic thermal conductivity of CNTs on thermal transport in CNT materials is consistent with results of large-scale mesoscopic simulations of CNT films reported in Ref. 59. The conductivity k defined by Eq. (3) can be transformed into the thermal conductivity k_F of (10,10) CNT films in units of W m^{-1} K^{-1} as $k_F = k/\Delta z$ using the approach suggested in Ref. 56. Here Δz is the film thickness associated with one 2D monolayer of CNTs assumed to be equal to a CNT diameter plus the equilibrium distance between surfaces of parallel CNTs, $\Delta z = 2R_f + 3.114$ Å. The values of k_F calculated based on Eq. (71) for various L_f and φ_S are shown in Fig. 28(b).

The model developed in this paper can be directly applied for calculation of the conductivity of quasi-2D layered CNT systems,[65] where the chemical cross-links or electrical charges counterbalance the intertube van der Waals attraction and prevent rearrangement of nearly straight individual CNTs into bundles. In most CNT films, however, the structure of contacts between individual CNTs and the corresponding intertube conductance[72] is strongly affected by the self-assembly of CNTs into networks of interconnected bundles.[5,7,85,88] The presence of nanotubes that serve as interconnects between the bundles is necessary for the stability of CNT films composed of CNTs in the absence of chemical cross-links.[88] As suggested by mesoscopic simulations,[56] the nanotubes that serve as interconnects between the bundles provide more efficient pathways for the heat propagation than junctions between pairs of crossing CNTs. As a result, the in-plane thermal conductivity of thin films composed of CNTs with infinitely large intrinsic conductivity tends to follow the scaling law obtained and analyzed in the present paper, but with a larger prefactor than predicted, e.g., by Eq. (28).

XI. CONCLUSIONS AND OUTLOOK

The thermal conductivity of 2D homogeneous and isotropic fibrous materials composed of straight soft-core spherocylinders is studied both numerically and theoretically for the arbitrary density parameter, aspect ratio of fibers, and Biot number defined for a single thermal contact. In all regimes of thermal transport considered in this work, the key factor that defines the material conductivity is the average temperature difference at the thermal contacts between individual fibers. At large density parameter, this temperature difference can be described by exact theoretical equations valid for any Biot number and aspect ratio of the fibers.

For dense materials, the theoretical approach developed in the present work produces, for the first time, the solution of the thermal transport problem and corresponding equations for the effective thermal conductivity valid for an arbitrary Biot number. In this solution, which becomes increasingly accurate with increasing material density, the effect of the intrinsic conductivity of fibers is found to be a function of the product of the density parameter and the Biot number for a single contact. Thus, this effect can be strong for a sufficiently dense material even at a small Biot number for a single contact. Such conditions are characteristic of various nanofiber materials with high intrinsic conductivity of individual nanofibers and low interfiber contact conductance, e.g., carbon nanotube network materials.

For the intermediate range of material density, semiempirical corrections to the theoretical equations are obtained based on the analysis of results of numerical simulations. These corrections account for growing correlations in fiber temperatures with decreasing density parameter and extend the range of applicability of the theoretically obtained equations down to the conditions close to the percolation threshold. In the vicinity of the percolation threshold, our numerical results confirm the hypothesis of existence of the universal conductivity exponent, which depends only on the spatial dimension of the considered system and is equal to 1.33 for 2D systems independently of the fiber aspect ratio.

The obtained equations, in agreement with the results of direct numerical simulations, predict a complex dependence of the effective thermal conductivity of fibrous materials on the density parameter, aspect ratio of fibers, and Biot number for a single contact. For materials composed of high-aspect-ratio fibers with a small Biot number for a single contact, the increase of the density parameter from the percolation threshold leads to a steep superquadratic initial rise of the conductivity. The superquadratic scaling turns into approximately linear scaling upon further increase of the density parameter. This linear scaling law is terminal for dense systems composed of slender rods. For fibers with a finite aspect ratio, both numerical simulations and theoretical equations predict a transition into quadratic terminal scaling due to the effect of thermal contacts involving semicircular caps of spherocylinders.

The complex dependence of the conductivity on the material parameters, revealed in this work, provides an explanation of a variety of scaling laws for thermal conductivity of fibrous materials reported in the literature based on numerical simulations performed in different regions of the parameter space. Moreover, the strong dependence of conductivity of fibrous materials on the length of fibers suggest that a fibrous material can be turned to function as either a thermal conductor or a thermal insulator by an appropriate adjustment of material structural characteristics, e.g., fiber length. This observation can also explain the large scattering in experimental data on the conductivity of CNT films and "buckypaper" and suggests that the measurements of the thermal conductivity of such materials should be accompanied by thorough characterization of the CNT length distribution.

The general theoretical and computational framework developed in this paper is not limited to 2D fibrous samples and can be reformulated for nonisotropic and three-dimensional (3D) fibrous materials. In particular, the mathematical approach for calculation of the individual contributions of various types of thermal junctions to the effective conductivity of the material briefly presented in Appendixes A–C and further detailed in the supplementary material enables a straightforward generalization to account for additional stochastic factors, such as preferential orientations of fibers and material anisotropy, distribution of fiber length, etc. The approach developed in the present paper can also be extended to account for additional features of thermal transport in fibrous materials, such as the length-, temperature-, and pressure-dependent thermal properties of individual fibers and their thermal contacts, as well as the presence of defects serving as additional thermal resistors that impede the propagation of heat along individual fibers.[89,90] The developed theory can also be adopted for non-thermal transport processes in fibrous material, which can be described by physical laws similar to the Fourier law for intrinsic conductivity of individual fibers and contact conductance law for interfiber heat exchange. In particular, the same theory can be applied to predict the effective electrical conductivity of fibrous materials,[50,51,67,91] when the electrical conductance along the fibers is described in the diffusive approximation based on the one-dimensional Ohm's law.

SUPPLEMENTARY MATERIAL

The supplementary material includes details of derivations of various equations used in the present work. Sections SI–SIII provide details of derivations briefly described in Appendixes A–C. In Sec. SIV, an approximate equation for the thermal conductivity of slender rods at a finite Biot number is obtained following the approach suggested in Ref. 59. Section SV contains the MATLAB® code for calculation of the coefficient $|\Lambda|$ in Eq. (76).

ACKNOWLEDGMENTS

Financial support for this work was provided by the National Aeronautics and Space Administration (NASA) through an Early Stage Innovations grant from NASA's Space Technology Research Grants Program (No. NNX16AD99G). A.N.V. also acknowledges support from the National Science Foundation (NSF) through the CAREER Award No. CMMI-1554589, and L.V.Z. acknowledges support from the U.S. Department of Energy (DOE) through the Vehicle Technologies Office Award No DE-EE0008195. Computational support was provided by the Alabama Supercomputer Center and by NASA's Advanced Supercomputing (NAS) Division. The authors thank Arun B. Thapa for his help in the preparation of the manuscript.

APPENDIX A: AVERAGE INTER-CENTER DISTANCES AT JUNCTIONS BETWEEN SCs

The average inter-center distance, $\langle \Delta\bar{x}_{(+)} \rangle$, introduced in Eq. (24) is a statistical mean of the random inter-center coordinate distance in a junction between a pair of SCs, $\Delta x_{(+)} = (x_{C_j} - x_{C_i})/L_f$, where $\chi_i(x) = 1$ and $\delta_{ij(+)}(x) = 1$ at given x. The value of $\langle \Delta\bar{x}_{(+)} \rangle$ can be found as a sum of contributions from junctions of different types shown in Fig. 8,

$$\langle \Delta\bar{x}_{(+)} \rangle = \int_0^{2\pi} \langle \Delta\bar{x}_{(+)} \rangle_{(1)}(\vartheta) \frac{A_{\mathrm{ex}(1)}(\vartheta)}{A_{\mathrm{ex}}} \frac{d\vartheta}{2\pi} + \sum_{k=2}^{4} \langle \Delta\bar{x}_{(+)} \rangle_{(k)} \frac{A_{\mathrm{ex}(k)}}{A_{\mathrm{ex}}}, \tag{A1}$$

where $\langle \Delta\bar{x}_{(+)} \rangle_{(k)}$ $(k = 1, .., 4)$ are the average dimensionless inter-center distances along the axis Ox for junctions of type k, and areas $A_{\mathrm{ex}(k)}$ are introduced in the text above Eq. (21). Although the first term in the right-hand side of Eq. (A1) implies a possible dependence of $\langle \Delta\bar{x}_{(+)} \rangle_{(1)}$ on the angle ϑ between SCs, the actual derivations presented in Sec. SI in the supplementary material show that $\langle \Delta\bar{x}_{(+)} \rangle_{(1)}$ is independent on ϑ and, therefore, the first term in Eq. (A1) reduces to $\langle \Delta\bar{x}_{(+)} \rangle_{(1)} A_{\mathrm{ex}(1)}/A_{\mathrm{ex}}$.

The values of $\langle \Delta\bar{x}_{(+)} \rangle_{(k)}$ can be found as conditional expectations of the random distance $\Delta x_C = x_{C_2} - x_{C_1}$ between centers of SCs along the axis Ox. The expectations are obtained under conditions that (i) SC 1 intersects the line $x = 0$ and (ii) the junction point J with coordinate x_J lies to the right of this line, i.e., at $x_J \geq 0$. The generic representations of x_J and Δx_C can be introduced using vector $\mathbf{r}_J = -\xi\mathbf{e}_1 + (r/2)\mathbf{e}$ connecting points I and J shown in Fig. 29 and vector $\Delta\mathbf{r}_C = \xi_1\mathbf{e}_1 + r\mathbf{e} - \xi_2\mathbf{e}_2$ connecting the centers of SCs C_1 and C_2, where the unit vectors $\mathbf{e}_1$, $\mathbf{e}$, and $\mathbf{e}_2$ are directed along the axis a_1 of SC 1, along the axis a (J_1J_2) that corresponds to the closest distance between SCs, and along the axis a_2 of SC 2, respectively (Fig. 29). The directions of vectors $\mathbf{e}_1$, $\mathbf{e}$,

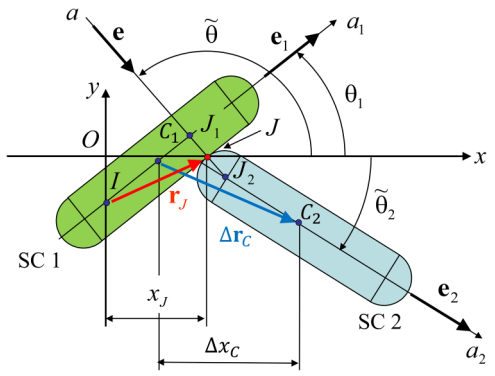

FIG. 29. Schematic representation of two interacting SCs, which illustrates definitions of vectors $\mathbf{r}_J$, $\Delta\mathbf{r}_C$, $\mathbf{e}$, $\mathbf{e}_1$, and $\mathbf{e}_2$ that are introduced to determine the junction coordinate x_J and inter-center distance Δx_C.

and $\mathbf{e}_2$ can be defined by corresponding angles θ_1, $\tilde{\theta}$, and $\tilde{\theta}_2$ between these vectors and the axis Ox. Then, $x_J = -\xi\cos\theta_1 + (r/2)\cos\tilde{\theta}$ and $\Delta x_C = \xi_1\cos\theta_1 + r\cos\tilde{\theta} - \xi_2\cos\tilde{\theta}_2$ can be found as projections of vectors $\mathbf{r}_J$ and $\Delta\mathbf{r}_C$ onto the axis Ox.

For junctions of type 1 shown in Fig. 8(a), $r = 0$, $\tilde{\theta}_2 = \theta_1 + \vartheta$, and the positions of SC 1 with respect to the axis $x = 0$ and SC 2 with respect to SC 1 are defined by distances ξ, ξ_1, ξ_2, and angle θ_1 at a given ϑ. For junctions of type 2 shown in Fig. 8(b), $\tilde{\theta} = \theta_1 - \pi/2$, $\tilde{\theta}_2 = \theta_1 - \pi/2 + \theta_2$, $\xi_2 = -L_f/2$, and the positions of SC 1 with respect to the line $x = 0$ and SC 2 with respect to SC 1 are defined by distances ξ, ξ_1, r, and angles θ_1 and θ_2. For junctions of type 3 shown in Fig. 8(c), $\tilde{\theta} = \theta_1 - \theta$, $\tilde{\theta}_2 = \theta_1 - \theta + \theta_2$, $\xi_1 = L_f/2$, and the positions of SC 1 with respect to the line $x = 0$ and SC 2 with respect to SC 1 are defined by distances ξ, ξ_2, r, and angles θ_1 and θ. For junctions of type 4 shown in Fig. 8(d), $\tilde{\theta} = \theta_1 - \theta$, $\tilde{\theta}_2 = \theta_1 - \theta + \theta_2$, $\xi_1 = L_f/2$, $\xi_2 = -L_f/2$, and the positions of SC 1 with respect to the line $x = 0$ and SC 2 with respect to SC 1 are defined by distances ξ, r, and angles θ_1, θ_2, and θ, where the variable r plays a role of a radius variable in polar coordinates.

To find an equation for $\langle\Delta\bar{x}_{(+)}\rangle_{(k)}$, we introduce a set of geometrical parameters $\zeta_{(k)} = (\zeta, \zeta_1, \ldots)$ that identify the position of SC 1 with respect to the line $x = 0$, as well as the position of SC 2 with respect to SC 1. The subscript "(k)" is hereinafter used to denote parameters specific for junctions of type k. The junctions of different types are characterized by different sets $\zeta_{(k)}$ as described above. We then define the conditional PDF $f_{(k)}(\zeta_{(k)})$ of parameters $\zeta_{(k)}$ and find $\langle\Delta\bar{x}_{(+)}\rangle_{(k)}$ as a conditional expectation,

$$\langle\Delta\bar{x}_{(+)}\rangle_{(k)} = \int\Delta\bar{x}_{C(k)}f_{(k)}(\zeta_{(k)})d\zeta_{(k)}, \tag{A2}$$

where $\Delta\bar{x}_{C(k)} = \Delta x_{C(k)}/L_f$. The details of derivation of $\langle\Delta\bar{x}_{(+)}\rangle_{(k)}$ for junctions of different types are given in Sec. SI in the supplementary material.

APPENDIX B: DISTRIBUTION OF AVERAGE TEMPERATURE DIFFERENCES AT JUNCTIONS ALONG AN ARBITRARILY INCLINED SC AT A FINITE Bi_c

The average temperature differences $\langle\Delta T_{\theta_1}\rangle_{(1,2)}$ and $\langle\Delta T_{\theta_1}\rangle_{(3,4)}$ introduced in Eqs. (41) and (48) can be represented in the following form:

$$\langle\Delta T_{\theta_1}\rangle_{(1,2)} = \int_0^{2\pi}\langle\Delta T_{\theta_1}\rangle_{(1)}(\vartheta)\frac{A_{\mathrm{ex}(1)}(\vartheta)}{A_{\mathrm{ex}(1)}+A_{\mathrm{ex}(2)}}\frac{d\vartheta}{2\pi} + \langle\Delta T_{\theta_1}\rangle_{(2)}\frac{A_{\mathrm{ex}(2)}}{A_{\mathrm{ex}(1)}+A_{\mathrm{ex}(2)}}, \tag{B1}$$

$$\langle\Delta T_{\theta_1}\rangle_{(3,4)} = \frac{A_{\mathrm{ex}(3)}\langle\Delta T_{\theta_1}\rangle_{(3)} + A_{\mathrm{ex}(4)}\langle\Delta T_{\theta_1}\rangle_{(4)}}{A_{\mathrm{ex}(1)}+A_{\mathrm{ex}(2)}}, \tag{B2}$$

where $\langle\Delta T_{\theta_1}\rangle_{(k)}$ is the contribution of junctions of type k. To find $\langle\Delta T_{\theta_1}\rangle_{(k)}$, we assume that the distribution of temperature along a SC satisfies Eq. (37). The coordinate of the center of SC 1, x_{C_1}, angle between the axis of SC 1 and axis Ox, θ_1, and coordinate of the junction on the axis of SC 1, x_1, are assumed to be fixed, while the position and orientation of SC 2 are random. Then, $\langle\Delta T_{\theta_1}\rangle_{(1,2)}$ and $\langle\Delta T_{\theta_1}\rangle_{(3,4)}$ can be found as conditional expectation values of the average temperature difference between two SCs, which depends on the average temperature distribution along a SC given by the function $\tau_{\theta_1}(x)$ in Eq. (39). The derivations described in Sec. SII in the supplementary material result in

$$\langle\Delta T_{\theta_1}\rangle_{(1,2)} = \nabla T_x(x_1 - x_{C_1}) - \tau_{\theta_1}(x_1 - x_{C_1}), \tag{B3}$$

$$\langle\Delta T_{\theta_1}\rangle_{(3,4)} = \nabla T_x L_f\frac{\cos\theta_1}{2}\frac{K + \pi\bar{R}_f F_{\theta_1}(D)}{1+\pi\bar{R}_f} - \tau_{\theta_1}\left(\frac{L_f\cos\theta_1}{2}\right), \tag{B4}$$

where $K = 1 + (8/\pi + \pi)\bar{R}_f + (16/3)\bar{R}_f^2$ and

$$F_{\theta_1}(D) = -\frac{2}{\cos\theta_1}\int_{-\pi/2}^{\pi/2}\frac{d\theta}{\pi}\int_{-\pi/2}^{\pi/2}\frac{d\theta_2}{\pi}\bar{\tau}_{\theta_1-\theta-\theta_2}\left(\frac{\cos(\theta_1-\theta-\theta_2)}{2}\right). \tag{B5}$$

By inserting Eq. (47) under the integral in the right-hand side of Eq. (B5), the functional $F_{\theta_1}(D)$ can be written as follows:

$$F_{\theta_1}(D) = -\frac{4}{\pi^2} + \frac{2}{\cos\theta_1}\int_{-\pi/2}^{\pi/2}\frac{d\theta}{\pi}\int_{-\pi/2}^{\pi/2}\frac{d\theta_2}{\pi}D(\theta_1-\theta-\theta_2)\cos(\theta_1-\theta-\theta_2). \tag{B6}$$

Here, $D(\theta_1)$ is an unknown function that must be determined using Eq. (52). It is worth noting that the subscript "θ_1" of functions $\tau_{\theta_1}(x)$ and $\bar{\tau}_{\theta_1}(\bar{\eta})$ in Eqs. (39) and (40) defines the value of an additional argument of these functions, which is equal to the angle

between the SC axis and axis Ox. Taking this convention into account, the function $\bar{\tau}_{\theta_1-\theta-\theta_2}(\bar{\eta})$ in Eq. (B5) must be considered as a function of two arguments, $\theta_1-\theta-\theta_2$ and $\bar{\eta}$.

APPENDIX C: AVERAGE TEMPERATURE DIFFERENCE AT JUNCTIONS BETWEEN SCs AT A FINITE Bi_c

The average temperature difference at the junctions at finite Bi_c, $\langle\Delta\bar{T}_{(+)}\rangle_\infty$, introduced in Sec. VIII, can be found based on its representation in a form similar to that of Eq. (A1),

$$\langle\Delta\bar{T}_{(+)}\rangle_\infty = \int_0^{2\pi}\langle\Delta\bar{T}_{(+)}\rangle_{(1)}(\vartheta)\frac{A_{\mathrm{ex}(1)}(\vartheta)}{A_{\mathrm{ex}}}\frac{d\vartheta}{2\pi} + \sum_{k=2}^{4}\langle\Delta\bar{T}_{(+)}\rangle_{(k)}\frac{A_{\mathrm{ex}(k)}}{A_{\mathrm{ex}}}, \tag{C1}$$

where $\langle\Delta\bar{T}_{(+)}\rangle_{(k)}$ is the average temperature difference at junctions of type k. The temperature differences can be found as conditional expectations of the random difference $\Delta T_J = T_2(x_{J_2}) - T_1(x_{J_1})$ between the average temperatures of SCs 1 and 2 at points J_1 and J_2, respectively, found under conditions that (i) SC 1 intersects the line $x = 0$ and (ii) the junction point J with coordinate x_J lies to the right of this line, i.e., $x_J \geq 0$.

The distribution of temperature along a SC is assumed to be described by Eq. (39). The temperature of SC i ($i = 1,2$) in a junction where the point J_i has coordinate x_{J_i} is then equal to $T_i(x_{J_i}) = T_0 + \nabla T_x L_f[x_{C_i} + \bar{\tau}_{\tilde{\theta}_i}(\bar{x}_{J_i} - \bar{x}_{C_i})]$, where $\tilde{\theta}_i$ is the angle between the axis of SC i and axis Ox ($\tilde{\theta}_1 = \theta_1$ for all junction types, but $\tilde{\theta}_2$ is defined differently for different junction types, see Appendix A), $\bar{x}_{J_i} - \bar{x}_{C_i} = \bar{\xi}_i\cos\tilde{\theta}_i$, and $\bar{\xi}_i = \xi_i/L_f$ is the reduced coordinate that specifies the position of the point J_i with respect to the point C_i (Fig. 29), so that

$$\Delta\bar{T}_{J(k)} = \Delta\bar{x}_{C(k)} + \bar{\tau}_{\theta_2}(\bar{\xi}_2\cos\tilde{\theta}_2) - \bar{\tau}_{\theta_1}(\bar{\xi}_1\cos\theta_1). \tag{C2}$$

Then, $\langle\Delta\bar{T}_{(+)}\rangle_{(k)}$ can be expressed in a form similar to that of Eq. (A2), where $\Delta\bar{x}_{C(k)}$ must be replaced with $\Delta\bar{T}_{J(k)}$. The derivation of expressions for $\langle\Delta\bar{T}_{(+)}\rangle_{(k)}$ for junctions of different types is provided in Sec. SIII in the supplementary material.

REFERENCES

[1]S. Kirkpatrick, "Percolation and conduction," Rev. Mod. Phys. **45**, 574–588 (1973).
[2]D. Stauffer and A. Aharony, *Introduction to Percolation Theory*, 2nd ed. (Taylor & Francis, London, 1992).
[3]P. Keblinski and F. Cleri, "Contact resistance in percolating networks," Phys. Rev. B **69**, 184201 (2004).
[4]P. Poulin, B. Vigolo, and P. Launois, "Films and fibers of oriented single wall nanotubes," Carbon **40**, 1741–1749 (2002).
[5]F. Hennrich, S. Lebedkin, S. Malik, J. Tracy, M. Barczewski, H. Rösner, and M. Kappes, "Preparation, characterization and applications of free-standing single walled carbon nanotube thin films," Phys. Chem. Chem. Phys. **4**, 2273–2277 (2002).
[6]T. V. Sreekumar, T. Liu, S. Kumar, L. M. Ericson, R. H. Hauge, and R. E. Smalley, "Single-wall carbon nanotube films," Chem. Mater. **15**, 175–178 (2003).
[7]W. Ma, L. Song, R. Yang, T. Zhang, Y. Zhao, L. Sun, Y. Ren, D. Liu, L. Liu, J. Shen, Z. Zhang, Y. Xiang, W. Zhou, and S. Xie, "Directly synthesized strong, highly conducting, transparent single-walled carbon nanotube films," Nano Lett. **7**, 2307–2311 (2007).
[8]A. G. Rinzler, J. Liu, H. Dai, P. Nikolaev, C. B. Huffman, F. J. Rodríguez-Macías, P. J. Boul, A. H. Lu, D. Heymann, D. T. Colbert, R. S. Lee, J. E. Fischer, A. M. Rao, P. C. Eklund, and R. E. Smalley, "Large-scale purification of single-wall carbon nanotubes: Process, product, and characterization," Appl. Phys. A Mater. Sci. Process. **67**, 29–37 (1998).
[9]L. Berhan, Y. B. Yi, A. M. Sastry, E. Munoz, M. Selvidge, and R. Baughman, "Mechanical properties of nanotube sheets: Alterations in joint morphology and achievable moduli in manufacturable materials," J. Appl. Phys. **95**, 4335–4345 (2004).
[10]S. Wang, Z. Liang, G. Pham, Y.-B. Park, B. Wang, C. Zhang, L. Kramer, and P. Funchess, "Controlled nanostructure and high loading of single-walled carbon nanotubes reinforced polycarbonate composite," Nanotechnology **18**, 095708 (2007).
[11]J. Zou, J. Liu, A. S. Karakoti, A. Kumar, D. Joung, Q. Li, S. I. Khondaker, S. Seal, and L. Zhai, "Ultralight multiwalled carbon nanotube aerogel," ACS Nano **4**, 7293–7302 (2010).
[12]K. J. Zhang, A. Yadav, K. H. Kim, Y. Oh, M. F. Islam, C. Uher, and K. P. Pipe, "Thermal and electrical transport in ultralow density single-walled carbon nanotube networks," Adv. Mater. **25**, 2926–2931 (2013).
[13]M. Xu, D. N. Futaba, M. Yumura, and K. Hata, "Alignment control of carbon nanotube forest from random to nearly perfectly aligned by utilizing the crowding effect," ASC Nano **6**, 5837–5844 (2012).
[14]S. Wang, Z. Liang, B. Wang, and C. Zhang, "High-strength and multifunctional macroscopic fabric of single-walled carbon nanotubes," Adv. Mater. **19**, 1257–1261 (2007).
[15]Z. Wang, Z. Liang, B. Wang, C. Zhang, and L. Kramer, "Processing and property investigation of single-walled carbon nanotube (SWNT) buckypaper/epoxy resin matrix nanocomposites," Compos. Part A **35**, 1225–1232 (2004).
[16]P. Kim, L. Shi, A. Majumdar, and P. L. McEuen, "Thermal transport measurements of individual multiwalled nanotubes," Phys. Rev. Lett. **87**, 215502 (2001).
[17]M. Fujii, X. Zhang, H. Xie, H. Ago, K. Takahashi, T. Ikuta, H. Abe, and T. Shimizu, "Measuring the thermal conductivity of a single carbon nanotube," Phys. Rev. Lett. **95**, 065502 (2005).
[18]Q. Li, C. Liu, X. Wang, and S. Fan, "Measuring the thermal conductivity of individual carbon nanotubes by the Raman shift method," Nanotechnology **20**, 145702 (2009).
[19]E. Pop, D. Mann, Q. Wang, K. Goodson, and H. Dai, "Thermal conductance of an individual single-wall carbon nanotubes above room temperature," Nano Lett. **6**, 96–100 (2006).
[20]J. Wang and J.-S. Wang, "Carbon nanotube thermal transport: Ballistic to diffusive," Appl. Phys. Lett. **88**, 111909 (2006).
[21]Y. Gu and Y. Chen, "Thermal conductivities of single-walled carbon nanotubes calculated from the complete phonon dispersion relations," Phys. Rev. B **76**, 134110 (2007).
[22]S. Berber, Y.-K. Kwon, and D. Tománek, "Unusually high thermal conductivity of carbon nanotubes," Phys. Rev. Lett. **84**, 4613–4616 (2000).
[23]J. Che, T. Çagın, and W. A. Goddard III, "Thermal conductivity of carbon nanotubes," Nanotechnology **11**, 65–69 (2000).
[24]M. A. Osman and D. Srivastava, "Temperature dependence of the thermal conductivity of single-wall carbon nanotubes," Nanotechnology **12**, 21–24 (2001).
[25]G. Zhang and B. Li, "Thermal conductivity of nanotubes revisited: Effects of chirality, isotope impurity, tube length, and temperature," J. Chem. Phys. **123**, 114714 (2005).
[26]R.-Q. Pan, Z.-J. Xu, and Z.-Y. Zhu, "Length dependence of thermal conductivity of single-walled carbon nanotubes," Chin. Phys. Lett. **24**, 1321–1323 (2007).
[27]J. Shiomi and S. Maruyama, "Molecular dynamics of diffusive-ballistic heat conduction in single-walled carbon nanotubes," Jpn. J. Appl. Phys. **47**, 2005–2009 (2008).

[28]R. N. Salaway and L. V. Zhigilei, "Molecular dynamics simulations of thermal conductivity of carbon nanotubes: Resolving the effects of computational parameters," Int. J. Heat Mass Transfer **70**, 954–964 (2014).
[29]L. V. Zhigilei, R. N. Salaway, B. K. Wittmaack, and A. N. Volkov, "Computational studies of thermal transport properties of carbon nanotube materials," in *Carbon Nanotubes for Interconnects: Process, Design and Applications*, edited by A. Todri-Sanial, J. Dijon, and A. Maffucci (Springer, 2017), pp. 129–161.
[30]J. Hone, M. Whitney, and A. Zettl, "Thermal conductivity of single-walled carbon nanotubes," Synth. Met. **103**, 2498–2499 (1999).
[31]J. Hone, M. Whitney, C. Piskoti, and A. Zettl, "Thermal conductivity of single-walled carbon nanotubes," Phys. Rev. B **59**, R2514–R2516 (1999).
[32]J. Hone, M. C. Llaguno, N. M. Nemes, A. T. Johnson, J. E. Fischer, D. A. Walters, M. J. Casavant, J. Schmidt, and R. E. Smalley, "Electrical and thermal transport properties of magnetically aligned single wall carbon nanotube films," Appl. Phys. Lett. **77**, 666–668 (2000).
[33]D. J. Yang, Q. Zhang, G. Chen, S. F. Yoon, J. Ahn, S. G. Wang, Q. Zhou, Q. Wang, and J. Q. Li, "Thermal conductivity of multiwalled carbon nanotubes," Phys. Rev. B **66**, 165440 (2002).
[34]P. Gonnet, Z. Liang, E. S. Choi, R. S. Kadambala, C. Zhang, J. S. Brooks, B. Wang, and L. Kramer, "Thermal conductivity of magnetically aligned carbon nanotube buckypapers and nanocomposites," Curr. Appl. Phys. **6**, 119–122 (2006).
[35]R. S. Prasher, X. J. Hu, Y. Chalopin, N. Mingo, K. Lofgreen, S. Volz, F. Cleri, and P. Keblinski, "Turning carbon nanotubes from exceptional heat conductors into insulators," Phys. Rev. Lett. **102**, 105901 (2009).
[36]D. J. Yang, S. G. Wang, Q. Zhang, P. J. Sellin, and G. Chen, "Thermal and electrical transport in multi-walled carbon nanotubes," Phys. Lett. A **329**, 207–213 (2004).
[37]I. Ivanov, A. Puretzky, G. Eres, H. Wang, Z. Pan, H. Cui, R. Jin, J. Howe, and D. B. Geohegan, "Fast and highly anistropic thermal transport through vertically aligned carbon nanotube arrays," Appl. Phys. Lett. **89**, 223110 (2006).
[38]D. Donadio and G. Galli, "Thermal conductivity of isolated and interacting carbon nanotubes: Comparing results from molecular dynamics and the Boltzmann transport equation," Phys. Rev. Lett. **99**, 255502 (2007).
[39]H. Zhong and J. R. Lukes, "Interfacial thermal resistance between carbon nanotubes: Molecular dynamics simulations and analytical thermal modeling," Phys. Rev. B **74**, 125403 (2006).
[40]S. Maruyama, Y. Igarashi, Y. Taniguchi, and J. Shiomi, "Anistropic heat transfer of single-walled carbon nanotubes," J. Therm. Sci. Technol. **1**, 138–148 (2006).
[41]E. Pop, D. A. Mann, K. E. Goodson, and H. Dai, "Electrical and thermal transport in metallic single-wall carbon nanotubes on insulating substrates," J. Appl. Phys. **101**, 093710 (2007).
[42]Y. Chalopin, S. Volz, and N. Mingo, "Upper bound to the thermal conductivity of carbon nanotube pellets," J. Appl. Phys. **105**, 084301 (2009).
[43]Z. Xu and M. J. Buehler, "Nanoengineering heat transfer performance at carbon nanotube interfaces," ACS Nano **3**, 2767–2775 (2009).
[44]S. Shenogin, L. Xue, R. Ozisik, P. Keblinski, and D. G. Cahill, "Role of thermal boundary resistance on the heat flow in carbon-nanotube composites," J. Appl. Phys. **95**, 8136–8144 (2004).
[45]L. Hu, D. S. Hecht, and G. Grüner, "Percolation in transparent and conducting carbon nanotube networks," Nano Lett. **4**, 2513–2517 (2004).
[46]M. Grujicic, G. Cao, and W. N. Roy, "A computational analysis of the percolation threshold and the electrical conductivity of carbon nanotubes filled polymer materials," J. Mater. Sci. **39**, 4441–4449 (2004).
[47]M. Foygel, R. D. Morris, D. Anez, S. French, and V. L. Sobolev, "Theoretical and computational studies of carbon nanotube composites and suspensions: Electrical and thermal conductivity," Phys. Rev. B **71**, 104201 (2005).
[48]T. Hu, A. Yu. Grosberg, and B. I. Shklovskii, "Conductivity of a suspension of nanowires in a weakly conducting medium," Phys. Rev. B **73**, 155434 (2006).
[49]J. Li, P. C. Ma, W. S. Chow, C. K. To, B. Z. Tang, and J.-K. Kim, "Correlations between percolation threshold, dispersion state, and aspect ratio of carbon nanotubes," Adv. Funct. Mater. **17**, 3207–3215 (2007).
[50]S. Kumar, M. A. Alam, and J. Y. Murthy, "Effect of percolation on thermal transport in nanotube composites," Appl. Phys. Lett. **90**, 104105 (2007).
[51]D. Hecht, L. Hu, and G. Grüner, "Conductivity scaling with bundle length and diameter in single walled carbon nanotube networks," Appl. Phys. Lett. **89**, 133112 (2006).
[52]N. A. Ashtekar and D. A. Jack "Stochastic modeling of the bulk thermal conductivity for dense carbon nanotube networks," in *ASME 2009 International Mechanical Engineering Congress and Exposition* (ASME, 2009), Paper IMECE2009-11282, pp. 157–163.
[53]J.-P. Vassal, L. Orgéas, D. Favier, J.-L. Auriault, and S. Le Corre, "Upscaling the diffusion equations in particulate media made of highly conductive particles. I. Theoretical aspects," Phys. Rev. E **77**, 011302 (2008).
[54]J.-P. Vassal, L. Orgéas, D. Favier, J.-L. Auriault, and S. Le Corre, "Upscaling the diffusion equations in particulate media made of highly conductive particles. II. Application to fibrous materials," Phys. Rev. E **77**, 011303 (2008).
[55]J.-P. Vassal, L. Orgéas, and D. Favier, "Modelling microstructure effects on the conduction in fibrous materials with fibre-fibre interface barriers," Model. Simul. Mater. Sci. Eng. **16**, 035007 (2008).
[56]A. N. Volkov and L. V. Zhigilei, "Scaling laws and mesoscopic modeling of thermal conductivity in carbon nanotube materials," Phys. Rev. Lett. **104**, 215902 (2010).
[57]M. Žeželj and I. Stanković, "From percolating to dense random stick networks: Conductivity model investigation," Phys. Rev. B **86**, 134202 (2012).
[58]Y. Yamada, T. Nishiyama, T. Yasuhara, and K. Takahashi, "Thermal boundary conductance between multi-walled carbon nanotubes," J. Therm. Sci. Technol. **7**, 190–198 (2012).
[59]A. N. Volkov and L. V. Zhigilei, "Heat conduction in carbon nanotube materials: Strong effect of intrinsic thermal conductivity of carbon nanotubes," Appl. Phys. Lett. **101**, 043113 (2012).
[60]X. Zhao, C. Huang, Q. Liu, I. I. Smalyukh, and R. Yang, "Thermal conductivity model of nanofiber networks," J. Appl. Phys. **123**, 085103 (2018).
[61]G. E. Pike and C. H. Seager, "Percolation and conductivity: A computer study. I," Phys. Rev. B **10**, 1421–1434 (1974).
[62]I. Balberg and N. Binenbaum, "Computer study of the percolation threshold in a two-dimensional anisotropic system of conducting sticks," Phys. Rev. B **28**, 3799–3812 (1983).
[63]I. Balberg, C. H. Anderson, S. Alexander, and N. Wagner, "Excluded volume and its relation to the onset of percolation," Phys. Rev. B **30**, 3933–3943 (1984).
[64]L. Berhan and A. M. Sastry, "Modeling percolation in high-aspect-ratio fiber systems. I. Soft-core versus hard-code models," Phys. Rev. E **75**, 041120 (2007).
[65]S. W. Lee, B.-S. Kim, S. Chen, Y. Shao-Horn, and P. T. Hammond, "Layer-by-layer assembly of all carbon nanotube ultrathin films for electrochemical applications," J. Am. Chem. Soc. **131**, 671–679 (2009).
[66]E. S. Snow, J. P. Novak, P. M. Campbell, and D. Park, "Random networks of carbon nanotubes as an electronic material," Appl. Phys. Lett. **82**, 2145–2147 (2003).
[67]S. Kumar, G. B. Blanchet, M. S. Hybertsen, J. Y. Murthy, and M. A. Alam, "Performance of carbon nanotube-dispersed thin-film transistors," Appl. Phys. Lett. **89**, 143501 (2006).
[68]Q. Cao and J. A. Rogers, "Ultrathin films of single-walled carbon nanotubes for electronics and sensors: A review of fundamental and applied aspects," Adv. Mater. **21**, 29–53 (2009).
[69]A. N. Volkov and L. V. Zhigilei, "Thermal conductivity of three-dimensional disordered fibrous materials governed by inter-fiber thermal contact conductance and intrinsic conductivity of fibers," (unpublished).
[70]The term "junction" adopted in the present paper can be used interchangeably with the term "thermal contact."
[71]W. J. Evans, M. Shen, and P. Keblinski, "Inter-tube thermal conductance in carbon nanotubes arrays and bundles: Effects of contact area and pressure," Appl. Phys. Lett. **100**, 261908 (2012).

[72]R. N. Salaway and L. V. Zhigilei, "Thermal conductance of carbon nanotube contacts: Molecular dynamics simulations and general description of the contact conductance," Phys. Rev. B **94**, 014308 (2016).
[73]L. I. Sedov, *Similarity and Dimensional Methods in Mechanics* (CRC Press, Boca Raton, FL, 1993).
[74]M. P. Allen and D. J. Tildesley, *Computer Simulation of Liquids* (Clarendon Press, Oxford, 1987).
[75]S. V. Patankar, *Numerical Heat Transfer and Fluid Flow* (Hemisphere, New York, 1980).
[76]It is worth noting that the heat flux given by Eqs. (6) or (7) can also be calculated as a sum of corresponding Fourier fluxes through SCs crossing the plane $x = const$ only in the case of slender rods with $R_f = 0$. At $R_f > 0$, one needs to account for the contribution of junctions where points J_{ij} and J_{ji} in Fig. 2 are on different sides of the plane $x = const$.
[77]A. L. R. Bug, S. A. Safran, and I. Webman, "Continuum percolation of rods," Phys. Rev. Lett. **54**, 1412–1415 (1985).
[78]S. Kirkpatrick, "Course 5. Models of disordered materials," in *Ill-Condensed Matter, Les Houches Session XXXI*, edited by R. Balian, R. Maynard, and G. Toulouse (North-Holland, Amsterdam, 1979), pp. 321–404.
[79]K. Binder and D. W. Heermann, *Monte Carlo Simulation in Statistical Physics*, 2nd ed. (Springer-Verlag, Berlin, 1992), pp. 40–41.
[80]J. Asikainen and T. Ala-Nissila, "Percolation and spatial correlations in a two-dimensional continuum deposition model," Phys. Rev. E **61**, 5002–5008 (2000).
[81]N. Provatas, M. Haataja, E. Seppälä, S. Majaniemi, J. Åström, M. Alava, and T. Ala-Nissila, "Growth, percolation, and correlations in disordered fiber networks," J. Stat. Phys. **87**, 385–413 (1997).
[82]L. Onsager, "The effects of shape on the interaction of colloidal particles," Ann. N. Y. Acad. Sci. **51**, 627–659 (1949).
[83]Although the temperature difference $\langle \Delta \bar{T}_{(+)} \rangle$ can be both positive and negative, in figures, we always plot the positive values of $\langle \Delta \bar{T}_{(+)} \rangle$ that correspond to the case of $\nabla T_x > 0$.
[84]A. N. Volkov and L. V. Zhigilei, "Mesoscopic interaction potential for carbon nanotubes of arbitrary length and orientation," J. Phys. Chem. C **114**, 5513–5531 (2010).
[85]A. Thess, R. Lee, P. Nikolaev, H. Dai, P. Petit, J. Robert, C. Xu, Y. H. Lee, S. G. Kim, A. G. Rinzler, D. T. Colbert, G. E. Scuseria, D. Tomanek, J. E. Fischer, and R. E. Smalley, "Crystalline ropes of metallic carbon nanotubes," Science **273**, 483–487 (1996).
[86]M. F. Islam, E. Rojas, D. M. Bergey, A. T. Johnson, and A. G. Yodh, "High weight fraction surfactant solubilization of single-wall carbon nanotubes in water," Nano Lett. **3**, 269–273 (2003).
[87]M. S. Dresselhaus, G. Dresselhaus, and R. Saito, "Physics of carbon nanotubes," Carbon **33**, 883–891 (1995).
[88]A. N. Volkov and L. V. Zhigilei, "Structural stability of carbon nanotube films: The role of bending buckling," ACS Nano **4**, 6187–6195 (2010).
[89]Z. Xu and M. J. Buehler, "Strain controlled thermomutability of single-walled carbon nanotubes," Nanotechnology **20**, 185701 (2009).
[90]A. N. Volkov, T. Shiga, D. Nicholson, J. Shiomi, and L. V. Zhigilei, "Effect of bending buckling of carbon nanotubes on thermal conductivity of carbon nanotube materials," J. Appl. Phys. **111**, 053501 (2012).
[91]S. P. Schießl, X. de Vries, M. Rother, A. Massé, M. Brohmann, P. A. Bobbert, and J. Zaumseil, "Modeling carrier density dependent charge transport in semiconducting carbon nanotube networks," Phys. Rev. Mater. **1**, 046003 (2017).